MEASUREMENT OF NEUTRON ENERGY ON D-T FUSION PLASMA EXPERIMENTS

Masaki Osakabe

Doctor of Philosophy

Department of Fusion Science

School of Mathematical and Physical Science

The Graduate University for Advanced Studies

1994

MEASUREMENT OF NEUTRON ENERGY ON D-T FUSION PLASMA EXPERIMENTS

Masaki Osakabe

Department of Fusion Science
The Graduate University for Advanced Studies

Dedicated
to my wife, Kazue Osakabe

Abstracts

Recently, D-T burning plasma experiments have been performed on the Joint European Torus (JET) and the Tokamak Fusion Test Reactor (TFTR). These experiments are expected to bring valuable information for reactor relevant plasmas. In these experiments, the role of fusion products diagnostics, such as neutron diagnostics, becomes more important than ever before. The measurements of neutron flux as well as neutron energy will provide us the information on 1) fusion output, 2) high energy ions produced by the auxiliary heatings and 3) α-heating. These are the major issues not only on those experiments but also on the experiments of the next large tokamak facility such as International Thermonuclear Experimental Reactor (ITER).

During past years, I have developed a new type of neutron spectrometer, named COTETRA (counter telescope with thick radiator), to measure the neutron energy spectra around 14MeV. The COTETRA has a merit of compactness with good energy resolution and high detection efficiency, hence it is suitable for space resolved neutron energy spectrum measurement. It is based on the concept of a proton recoil telescope. In a conventional proton recoil telescope, protons are recoiled by incident neutrons in a thin polyethylene film (radiator). Some of protons enter into a detector (E-detector) placed in a certain geometry, e.g. behind the radiator. The energy of the neutron is evaluated from the recoil proton energy being measured with E-detector, when the energy loss of the proton in the radiator is negligibly small to the proton energy. Therefore, the radiator is preferred to be as thin as possible to measure the neutron energy with good accuracy, although the usage of a thin radiator reduces the detection efficiency of the telescope. In COTETRA, a plastic scintillator (ΔE-detector) is used as a radiator. The energy of

neutron is evaluated by the sum of the energy deposit of recoil proton in ΔE- and that in E-detector. A thicker radiator can be used in COTETRA than a conventional telescope, since the energy deposit of proton in the radiator can be obtained in COTETRA. Therefore, COTETRA has better detection efficiency.

A prototype of COTETRA was constructed to verify its operation principle. The calibration experiments were performed using a D-T neutron generator. The energy resolution of $5.3\pm0.9\%$ and the detection efficiency of 1.3×10^{-4} counts/(n/cm^2) were achieved.

A Monte Carlo code that simulates its detection process has been developed to evaluate the performance of COTETRA. The calculation agrees with the results of the calibration experiments within its margin of error. The calculation also suggests that the energy resolution up to 3% is achievable with the detection efficiency of $\sim10^{-5}$ counts/(n/cm^2).

In 1992, two types of COTETRA were developed for the application to TFTR D-T experiments. One uses a Si-diode (set-A) as an E-detector and the other uses NE102A plastic scintillator, instead (set-B). Both of them use NE102A as a ΔE-detector. Set-A was characterized by higher energy resolution, while set-B was by higher counting rate capability and detection efficiency. For the use under high neutron flux rate condition, both sets have smaller detection area and use faster electronics than the prototype. Calibration experiments for these sets were also performed. An energy resolution of 4.0% was obtained for set-A. Set-B is expected to work at a count rate of up to 10^4cps, which corresponds to a neutron flux rate of $\sim10^9$ (n/cm^2)/s. The detection efficiency of set-B was $\sim6\times10^{-5}$ counts/(n/cm^2).

Both of them were installed at the multichannel neutron collimator of TFTR in 1993. At this location, COTETRA's are viewing plasmas perpendicularly to the magnetic field. A data acquisition system was

newly developed for each set. Two functions are newly applied to the system. One function provides the timing information of neutron events during shots. Another function provides the information of accidental coincidence between ΔE- and E-detector. The accidental coincidence causes serious problem when the neutron flux is extremely high. On the calibration experiment, the effect of accidental coincidence was evaluated by placing a tantalum plate between ΔE- and E-detector. It was not possible to apply this method on TFTR. Therefore, the evaluation was made by the timing-shift technique. Using this technique along with normal coincidence technique, two types of coincidence spectra, called foreground and background spectra, were obtained. The foreground spectrum was obtained by accumulating the coincidence events of the three PMT's (two attached to ΔE-detector and one to E-detector). This spectrum contains events due to accidental coincidences between ΔE- and E-detector as well as those due to true coincidences, in which protons recoiled at ΔE-detector is detected by E-detector. The background spectrum was obtained by coincidence events between the timing signal of ΔE-detector and the 10-nsec shifted timing signal of E-detector. Then, it contains only events due to accidental coincidence. It was verified that these two new functions were working successfully on TFTR.

The Monte Carlo code NESFP was developed to calculate the energy spectra of neutrons emerged from D-T fusion plasmas. With this code, the neutron energy spectrum and the fusion reactivity of a plasma for any velocity distributions of deuterium and tritium ion species can be calculated. The validity of the code was checked by comparing its results with those in other publications in the case where deuterium and tritium ions have Maxwellian velocity distribution.

The D-T fusion plasma experiments have been performed since November 1993 on TFTR. Tritium was introduced to the torus by gas

puffing and/or by neutral beam injection (NBI). As auxiliary heatings, the NBI heating and ion cyclotron range of frequency (ICRF) heating were provided.

The D-T neutron energy spectra were obtained for 'NBI and ICRF' heated plasmas and for NBI heated plasmas. These were the first D-T neutron spectra obtained from D-T plasmas in the world. The full width at half maximum (FWHM) of the peak for the ICRF heated plasma is wider than that for NBI heated plasma. The calculated energy spectra suggested this broadening was due to the existence of the high energy tritium ion tail of 100~400keV. The calculation also suggested that, for D-T plasmas, it is necessary to measure the energy spectrum in evaluating the existence of high energy ions besides the total neutron yield, which might decrease at higher ion temperature.

Space resolved measurements of D-T neutron energy spectra will be necessary for ICRF heated D-T plasma experiments on the next large tokamak, such as ITER, to evaluate the mechanism of ICRF heating in the plasma. The COTETRA will be a suitable diagnostic for this purpose because of its good energy resolution and compactness.

Acknowledgments

Table of CONTENTS

Chapter 1

Introduction

1.1 Fusion Products Measurements

A number of nuclear fusion experiments have been performed and undertaken in the world. The practical goal of the research is to develop a controlled fusion reactor, which is expected to be an ultimate solution for energy problems. Followings are likely to be chosen as nuclear fusion reactions in the fusion reactor:

i)   D + D => p (3.02MeV) + T (1.01MeV) ; 50%

 => n (2.45MeV) + ^{3}He (0.82MeV); 50%

ii) D + T => n (14.03MeV) + ^{4}He (3.56MeV);100%

iii) D + ^{3}He => p (14.64MeV) + ^{4}He (3.71MeV);100%
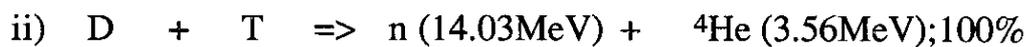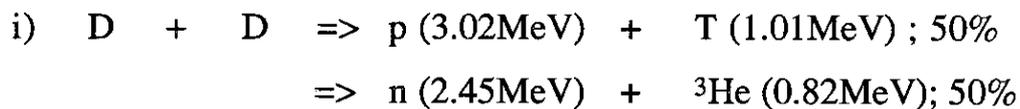
For each reaction, there exists a branch where γ-ray is emitted. The fraction in which such branch likely occurs is much smaller than that of the branch shown above.

Fusion products measurement is one of fusion plasma diagnostics, which utilizes particles produced in these reactions. By this measurement, fusion reactivities of plasmas, confinement and loss of fast ions and slowing-down process of fast ions can be obtained, which are central issues of the nuclear fusion research. An advantage of fusion products measurement is that they are naturally generated in plasmas, and the measurement is non-perturbative to plasmas, i.e., it will not change properties of interested plasmas.

On magnetically confined plasma facilities, various fusion products measurements have been performed or planned [1-17]. The measurement

1

can be categorized to two classes. One is the unconfined charged particle measurement, where proton and helium are the interested particles[3,5,11,12]. The other is non-charged particle measurement, where neutron and γ-ray are of our interests[1,2,4,6-10,13-17]. Since they are essentially neutral, they will not be perturbed by the magnetic field and can penetrate vacuum vessels. Therefore, the measurement can be done by detectors installed at a distant place from a plasma and can bring global information of the plasma. This is an advantage of the measurement. As the amount of γ-ray emitted is very small and that of neutron is large, neutron measurements are widely applied as a non-charged fusion particle measurement. (Even if a D-^{3}He plasma is of our interest, neutrons can be produced by the reaction between deuterium ions in the plasma.)

1.2 Neutron Measurements

In measuring neutron, neutron is often converted to some charged particles using certain nuclear reactions, such as, proton recoil, n-p and n-α reaction, and nuclear fission reaction[18,19]. The reaction often used are ^{10}B(n,α), ^{6}Li(n,α), ^{3}He(n,p), and H(n,p). The type of the reaction must be chosen according to the purpose and the environment of the measurement.

To measure the energy of non-thermal neutron, H(n,p) reaction is widely used because the cross section of hydrogen for the reaction is relatively large and well evaluated, and has a simple energy structure. What is more, a neutron could deposit its all of energy by a single scattering with hydrogen. One of the great difficulties in measuring the energy of neutron using H(n,p) reaction is that the proton is isotropically recoiled in the center-of-mass system and the amount of deposited energy on the proton depends on the recoil angle. In Fig.1-1, the expected proton energy distribution is shown for the case when it is recoiled by
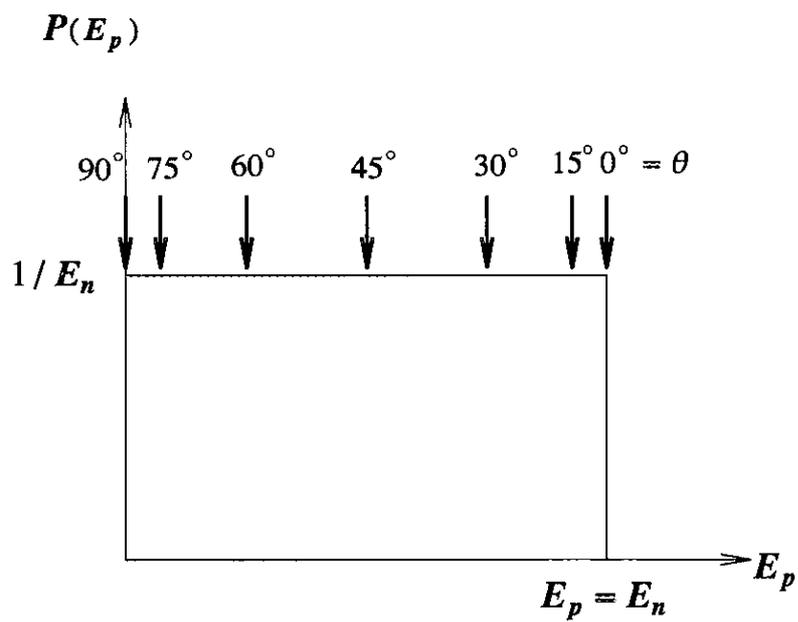
Fig.1-1 The energy distribution of proton being recoiled by mono-energetic neutron. The θ denotes the proton recoil angle.

mono-energetic neutrons. Therefore, the evaluation of neutron energy is not simple in this method.

There are three major methods of neutron measurement that uses $H(n,p)$ reaction (Fig.1-2). The first method (Fig.1-2(a)) has a simple experimental configuration, but requires complicated data analysis, called *unfolding*, in obtaining neutron spectra because the proton recoil angle is not limited. In obtaining neutron spectra by *unfolding*, a lot of statistics are necessary for the proton spectra, otherwise the obtained spectra will have non-physical peaks in the low energy region of it. The second method (Fig.1-2(b)) is called 'proton recoil counter telescope method.' In this method a thin polyethylene film, in which proton is recoiled, is placed in front of the proton detector so that the recoil angle of proton is restricted by the geometrical configuration of the film and the detector. Therefore, the neutron energy can be directly obtained by the proton energy. With this method, we can achieve fairly high energy resolution, but the detection efficiency is limited by the restriction of angle and the thickness of a thin film. In the third method (Fig.1-2(c)), the incident neutron energy was evaluated from the time-of-flight(TOF) of the scattered neutron. This method uses at least two detectors where protons are recoiled, and the scattering angle of the neutron is limited by the configuration of these two detectors. The energy resolution of this method is very high. On the other hand, the detection efficiency is low, because the neutron must undergo the n-p scattering twice and the scattering angle is limited.

1.3 D-T Neutron Energy Spectroscopy for Fusion Diagnostic

The D-T fusion plasma experiment has been undertaken only at the Joint European Torus (JET) and Tokamak Test Fusion Reactor (TFTR) [20-23].
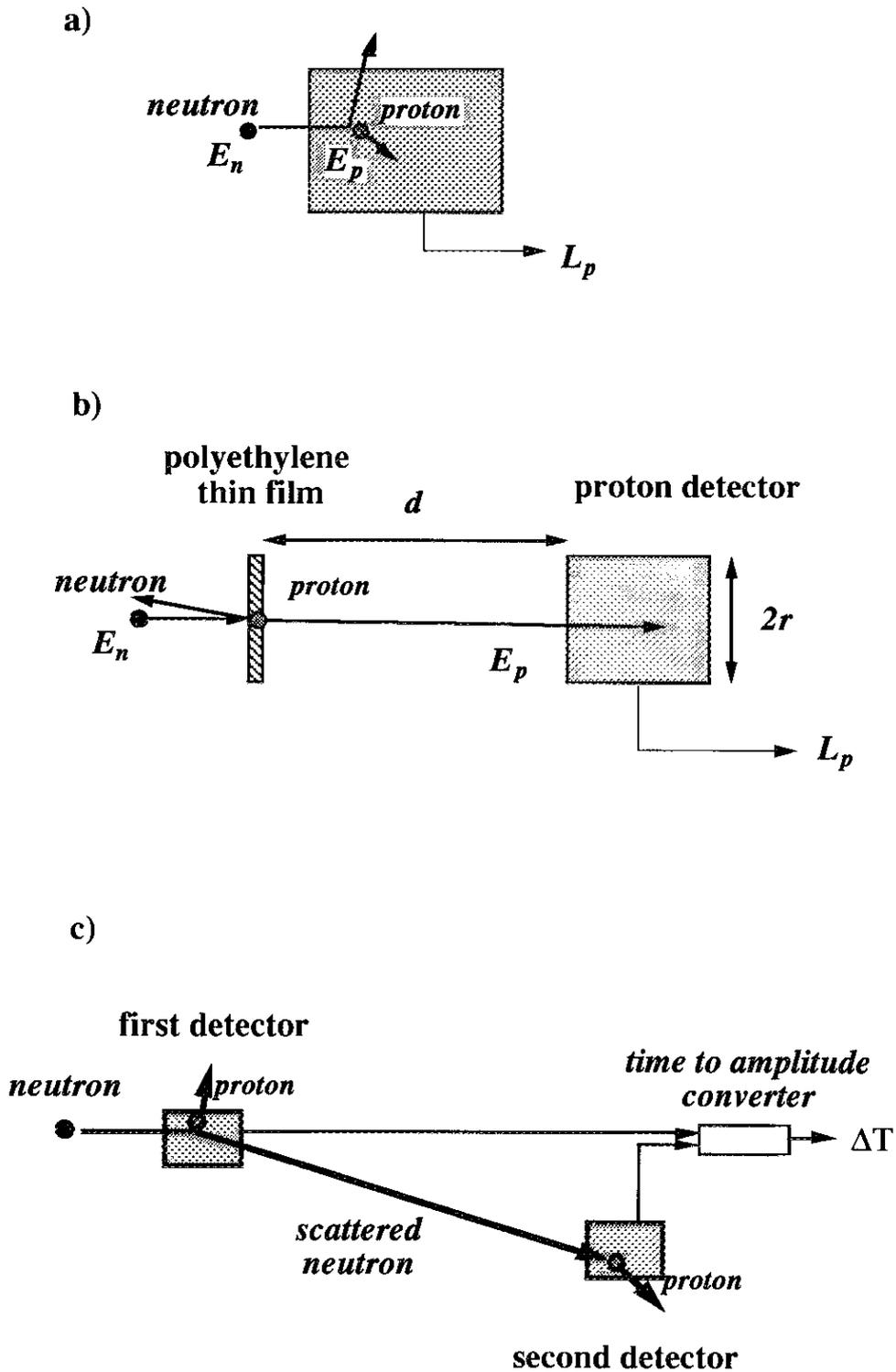
Fig.1-2 Conceptual drawing of neutron energy measurement using H(*n,p*) reaction. (a) proton recoil with unfolding method, (b) proton recoil counter telescope method, and (c) double scintillator time-of-flight method.

Plasma parameters obtainable from neutron spectrum measurement depend on its energy resolution (ΔR). When it is measured with high resolution, we can determine the plasma ion temperature (T_i) from the Doppler width (ΔE_D) of the D-T neutron peak by using the relation of $T_i \simeq (\Delta E_D/177)^2$, where T_i and ΔE_D are in [keV]. Generally in JET and TFTR, the ion temperature of the plasma is about 5 to 30keV. In these situations, the required ΔR of a spectrometer is about 3% at the D-T neutron energy. Even if the energy resolution of the spectrum is not fine enough to determine T_i, the total neutron yield and the neutron emission profile are obtainable, which are also of our great interests. In this case, the energy of the neutron is measured to identify its origin of the reaction, e.g., D-T reaction, D-D reaction, or (γ, n) reaction, and so on.

The time resolution is another important parameter of the measurement since the plasma parameters are changing with time. Because the slowing-down time of 3.5-MeV α-particle (τ_α) is one of the most important time scales in the fusion experiment (typically, $\tau_\alpha \geq 0.1$ sec for the electron density less than 3×10^{20} [electrons/m^3] at $T_e = 10$keV), it is preferable to set the time resolution less than 0.1 sec. In order to get enough count ($\geq 10^2$ counts) during this period, the count rate capability (CR^{cap}) of the spectrometer should be greater than 10^3 cps. In the D-T experiment at TFTR and JET, the D-T neutron flux of $10^8 \sim 10^{10}$ [n/cm^2/sec] is expected at the place where the neutron spectrometer is located. To obtain the count rate over 10^3 cps, the detection efficiency (η) of the spectrometer must be greater than 10^{-5} [counts/(n/cm^2)].

The required performances of the neutron spectrometer for D-T plasma diagnostics are $\Delta R < 3\%$, $\eta > 10^{-5}$ [counts/(n/cm^2)], and $CR^{cap} > 10^3$ cps.

To satisfy these requirements, a modified recoil counter telescope (COTETRA) has been developed and applied to the TFTR D-T

6

experiments. In a conventional recoil counter telescope, a thin polyethylene film (~10μm) is used as a radiator. In COTETRA, this thin film was replaced with relatively thick scintillator (2mm) and the energy deposit of a recoil proton in the radiator was measured. With this modification, the detection efficiency was increased without deteriorating the energy resolution of the spectrometer. The idea is similar to that of the spectrometers being suggested by Mozley et.al.[24] and constructed by Calvert et al.[25] and Gellar et.al.[26] in the field of nuclear physics. Gellar used stilbene scintillator as a radiator and coupled it with single photo multiplier tube (PMT). In COTETRA, the NE102A plastic scintillator was used, because it has the merits of fast signal, easy handling, uniform optical quality and mechanical strength. Two PMT's were attached to the scintillator so as to increase the signal to noise ratio by employing coincidence technique. Moreover, COTETRA itself and its detection system were optimized for measuring D-T neutron on magnetically confined fusion devices.

Several types of neutron spectrometers are prepared for the D-T experiments on JET, such as TANSY, MPR, and etc.[27,28]. TANSY is an improved TOF spectrometer. It was reported that TANSY achieved the energy resolution of ~1% and detection efficiency of $1.4 \times 10^{-5} cm^2$[27].

1.4 Outline of Thesis

This thesis is composed of six chapters. Chapter 1 is for an introduction. In chapter 2, the development of COTETRA neutron spectrometer is described, including the development of the simulation code of the detection process in COTETRA, and its installation on TFTR is described in chapter 3. Monte Carlo calculation of neutron spectra that are expected to be obtained at D-T fusion plasma experiments is presented in chapter 4. In chapter 5, neutron energy spectra obtained at TFTR D-T

experiments and the analysis on the spectra are shown. Finally, it is concluded in chapter 6.

References

[1] C.L.Fiore, *et.al.*, Rev. Sci. Instrum. **63**, 4530 (1992)

[2] S.Rollet, *et.al.*, Rev. Sci. Instrum. **63**, 4551 (1992)

[3] R.L.Boivin, *et.al.*, Rev. Sci. Instrum. **63**, 4533 (1992)

[4] N.P.Hawkes, *et.al.*, Nucl. Instrum. and Meth. **A335**, 533 (1993)

[5] T.J.Murphy, *et.al.*, Nucl. Instrum. and Meth. **A267**, 520 (1988)

[6] O.N.Jarvis, Plasma Phys. Control. Fusion **36**, 209 (1994)

[7] S. Conroy, *et.al.*, Nucl. Fusion **28**, 2127 (1988)

[8] O.N.Jarvis, *et.al.*, Fusion Technology **20**, 265 (1991)

[9] J.D.Strachan, *et al.*, Rev. Sci. Instrum. **59**, 1732 (1988)

[10] A.L.Roquemore, *et al.*, Rev. Sci. Instrum. **61**, 3163 (1990)

[11] W.W.Heidbrink, *et al.*, Rev. Sci. Instrum. **56**, 501 (1985)

[12] W.W.Heidbrink, *et al.*, Nucl. Fusion **27**,129 (1987)

[13] M.Pillon, *et.al.*, Fusion Technology **15**, 1420 (1989)

[14] H.W.Hendel, *et al.*, Rev. Sci. Instrum. **61**, 1900 (1990)

[15] M.Angelone, *et al.*, Rev. Sci. Instrum. **61**, 3157 (1990)

[16] C.W.Barnes, *et al.*, Rev. Sci. Instrum. **61**, 3151 (1990)

[17] J.D.Strachan, *et al.*, Nucl. Fusion **33**, 991 (1993)

[18] G.F.Knoll, *Radiation Detection and Measurement, Second Edition* (John Wiley and Sons, 1989) .

[19] N.Tsoulfanidis, *Measurement and Detection of Radiation* (McGraw-Hill,1983)

[20] JET Team, Nucl. Fusion **32**, 187 (1992)

[21] J.D.Strachan, *et al.*, Physical Review Letters **72**, 3526 (1994)

[22] R.J.Hawryluk, *et al.*, Physical Review Letters **72**, 3530 (1994).

[23] R.J.Hawryluk, *et al.*, Physics of Plasmas **1**, 1560 (1994)

[24] R.F.Mozley, *et.al.*, Rev. Sci. Instr. **23**, 569 (1952)

[25] J.M.Calvert, *et.al.*, Proc. Phys. Soc. **A68**, 1017 (1955)

[26] K.N.Gellar, *et.al.*, Nucl. Instr. Meth. **69**, 141 (1969)

[27] M.Hoek, *et.al.*, Nucl. Instr. Meth. **A322**, 248 (1992)

[28] Jan Källne, *et.al.*, Nucl. Instr. Meth. **A311**, 595 (1992)

[29] D.L.Jassby, *et.al.*, Phys. Fluids **B3**, 2308 (1991)

[30] T.Nishitani, The Journal of the Japan Society of Plasma Science and Nuclear Fusion Research **68**, 6 (1992)

Chapter 2

Development of a New Neutron Spectrometer for D-T Experiments

2.1 Principle of Neutron Energy Spectrometer "COTETRA"

a) Detection Principle

Based on the proton recoil counter telescope method, we have developed a new type of neutron energy spectrometer, named COTETRA (Counter Telescope with Thick Radiator) [1]. In conventional proton recoil telescope, a polyethylene film was used as a radiator (Fig.1-2(b)). The film must be as thin as possible to achieve good energy resolution, since the proton energy loss can not be obtained in the polyethylene film. Consequently, its detection efficiency was small. As shown in Fig.2-1, COTETRA uses a plastic scintillator (ΔE-detector) as a radiator instead of a polyethylene film to overcome the defect.

When a neutron entering ΔE-detector recoils a proton, the proton will fly to E-detector with a certain probability. The energy of the incident neutron (E_n) can be expressed using that of recoil proton (E_p) and its recoil angle (θ) with respect to the neutron direction:

$$E_n = E_p \sec^2\theta. \tag{2-1}$$

The recoil angle of a proton that enters into E-detector is limited by the sizes of ΔE- and E-detector (r_1, and r_2) and by the distance (d) between them. This limitation is expressed as

$$0 \leq \theta \leq \arctan\{(r_1+r_2)/d\} \tag{2-2}$$

where r_1 is the radius of ΔE-detector, and r_2 is that of E-detector. In case $r_1+r_2 \ll d$, we have $\sec^2\theta \simeq 1$. Then, the energy of the neutron can be obtained directly by measuring that of the recoil proton. When the
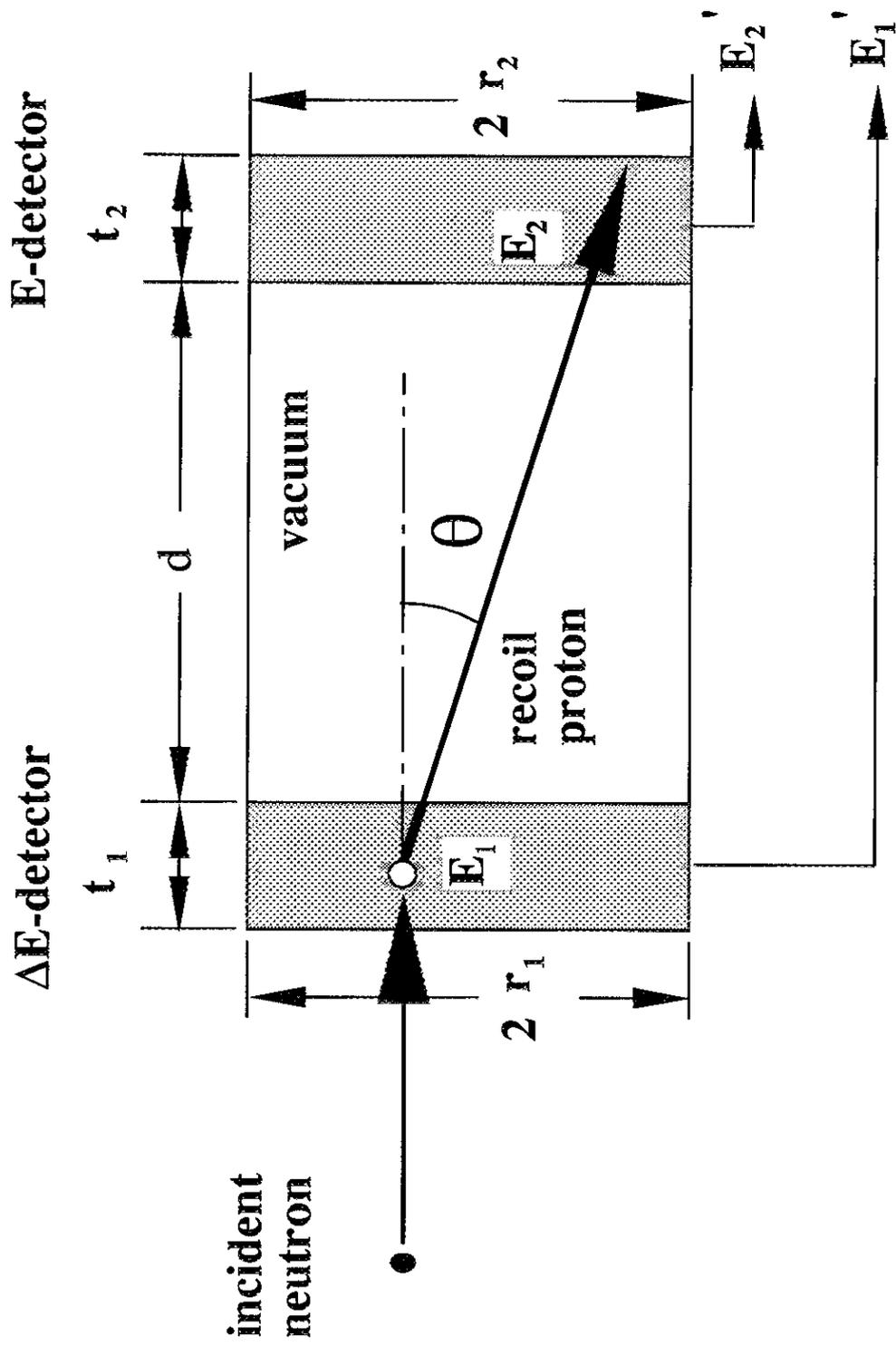
Fig.2-1 A conceptual figure of COTETRA neutron spectrometer

thickness of E-detector is sufficient to stop the recoil proton, its energy can be expressed with the sum of its energy loss in ΔE-detector (E_1) and that in E-detector (E_2). Therefore, the energy of an incident neutron can be obtained from E_1 and E_2, i.e.,

$$E_n \simeq E_1 + E_2. \qquad (2\text{-}3)$$

The higher signal-to-noise ratio is one of the other advantages of COTETRA in comparison with the conventional telescope. As shown in eq.(2-3), COTETRA only detects the coincidence events between ΔE- and E-detector, which are due to the recoil proton crossing through these two detectors, in principle. On the other hand, the conventional telescope can not distinguish the events due to the proton recoiled in the radiator from those due to the particle induced by the neutron in an E-detector. The later events are considered as noise signals since we can not apply the restriction of eq.(2-2).

b) Energy Resolution

Energy resolution of COTETRA can be expressed as follows

$$\Delta E_{tot}^2 = \Delta E_{det}^2 + \Delta E_{geo}^2, \text{ and} \qquad (2\text{-}4)$$
$$\Delta E_{det}^2 = <\Delta E_1^2>_{12} + <\Delta E_2^2>_{12}, \qquad (2\text{-}5)$$

where ΔE_{tot} is total energy resolution of COTETRA. The ΔE_{det} is energy broadening due to the intrinsic energy resolution of ΔE- and E-detector, which are ΔE_1 and ΔE_2, respectively. The ΔE_{geo} is that due to the recoil angle spread, which strongly depends on the geometrical configuration of COTETRA. The symbol $<>_{12}$ denotes an average over the distribution of (E_1, E_2).

There are two types of geometrical effects that appear in the energy resolution. One depends mainly on the ratio $(r_1+r_2)/d$ and appears in the second term of the eq. (2-4). This effect strongly relates to the

restriction on the recoil angle. To minimize the energy resolution, the ratio is preferred to be as small as possible. Another effect depends on the thickness of ΔE-detector (t_1). In general, ΔE-detector has worse energy resolution than E-detector because of the complicated configuration of ΔE-detector and the use of plastic scintillator in it. Therefore, the total energy resolution of COTETRA increases with an increase in the ratio of the proton energy deposit in ΔE-detector to that both in ΔE- and E-detector, which strongly depends on the thickness of ΔE-detector. This effect appears both in the first and second terms of eq. (2-5) through the distribution of (E_1, E_2).

c) Detection Efficiency

Total detection efficiency of the spectrometer, η_{tot} [counts/(neutron/cm^2)], is the product of the single counting efficiency of ΔE-detector, η_1 [counts/(n/cm^2)], and the probability of a proton recoiled at ΔE-detector entering E-detector., $\overline{\varepsilon_{geo}}$, i.e.,

$$\eta_{tot} = \eta_1 \overline{\varepsilon_{geo}} . \qquad (2\text{-}6)$$

The single counting efficiency η_1 is roughly determined by the products of the cross section of n-p scattering for hydrogen atom, the density of hydrogen, and the volume of ΔE-detector ($\pi r_1^2 t_1$). The probability $\overline{\varepsilon_{geo}}$ is proportional to the solid angle of E-detector being seen from ΔE-detector, which strongly relates to the ratio $(r_1+r_2)/d$. To achieve high efficiency detection system, the thickness t_1 and the ratio $(r_1+r_2)/d$ are preferred to be as large as possible. This contradicts to the requirement of the energy resolution.

In designing COTETRA, we need to estimate the effect of these parameters, i.e., t_1 and $(r_1+r_2)/d$, on the detection efficiency and the energy resolution, and also need to choose the appropriate values of them for our purpose.

13

2.2 Prototype of COTETRA and the Calibration Experiment

a) Prototype Spectrometer

Figure 2-2 shows a schematic drawing of the prototype spectrometer assembly. A plastic scintillator (NE102A) and a Si(Li) semiconductor detector were used as ΔE- and E-detector, respectively. The sizes of these detectors are shown in Table 2-1.

Table 2-1 Physical Dimensions of the Prototype, Set-A, and Set-B of COTETRA. The distance (d) denotes that between ΔE- and E-detector

Type of Sets	ΔE-detector			E-detector			distance d
	material	diameter	thickness	material	diameter	thickness	
Prototype	NE102A	21 mm	2 mm	Si(Li)	12.6mm[*1]	5 mm	250 mm
Set-A	NE102A	12 mm	0.5 mm	SSBD	11.3mm[*2]	2 mm	80 mm
Set-B	NE102A	12 mm	2 mm	NE102A	12 mm	2 mm	70 mm

*1 and 2: Equivalent diameter for the effective area of 500 and 100 mm^2, respectively.

The plastic scintillator was installed in an aluminum cylinder (hollow light guide) with inner polished surface and was optically connected to two PMT's through it. These two PMT's were placed to face the cylindrical side surface of the scintillator so that they would not disturb the incident neutrons and the recoil protons. The right hand side flat surface of the scintillator in Fig.2-2 was coated with evaporated aluminum in order not to lose the right going scintillation light and to optically shield the E-detector. On the left hand side flat surface of the scintillator, a Lucite lens was attached to extract the scintillation light effectively to outside from the scintillator. The effect of the Lucite lens on the light collection efficiency are shown in Appendix A.

b) Arrangements of Calibration Experiment

The prototype spectrometer had been tested using an intense D-T neutron source at Osaka University (OKTAVIAN). Mono-energetic
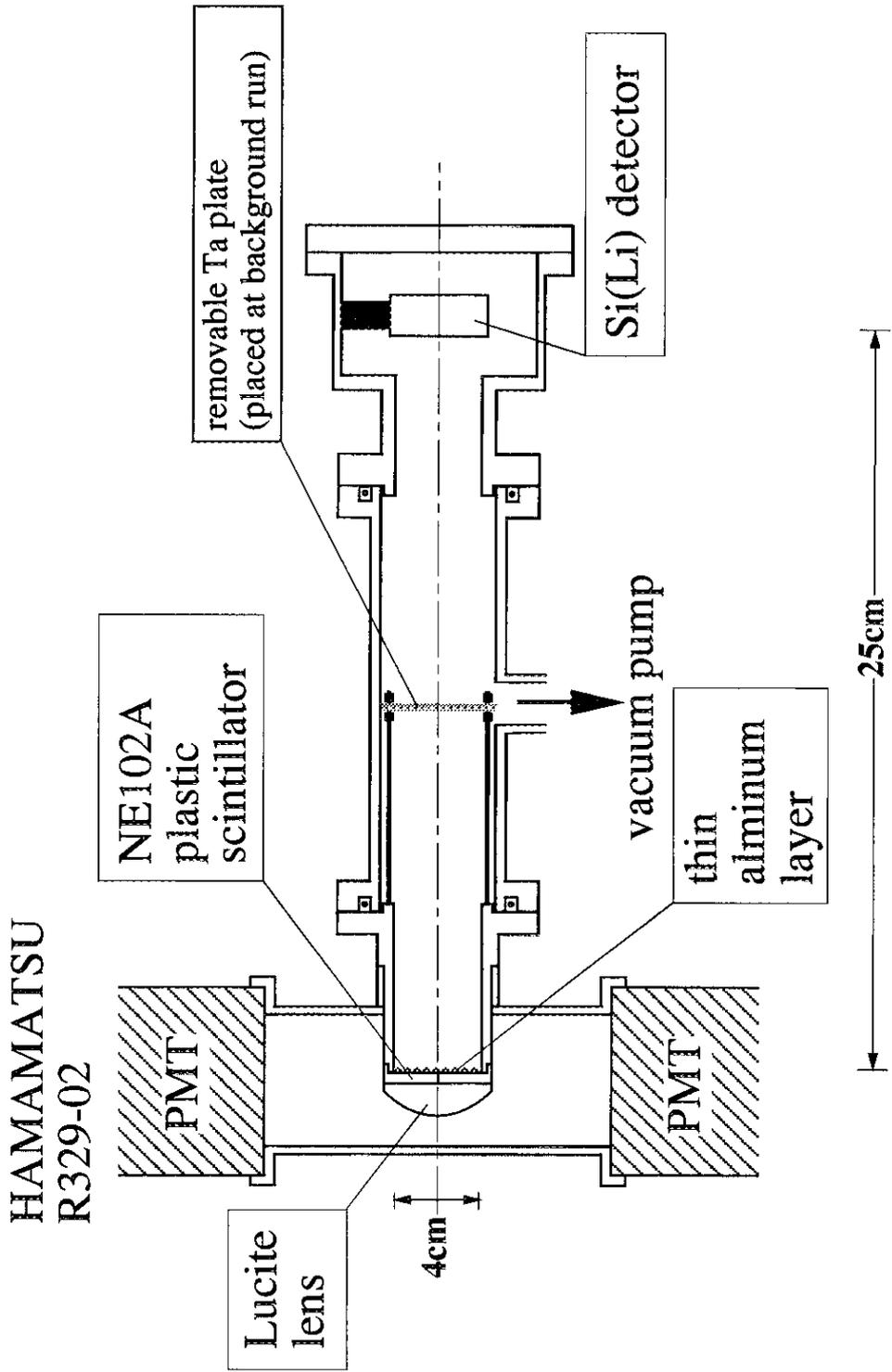
Fig. 2-2 Schematic drawing of prototype spectrometer assembly.

HAMAMATSU
R329-02

PMT

PMT

Lucite
lens

NE102A
plastic
scintillator

removable Ta plate
(placed at background run)

thin
aluminum
layer

vacuum pump

Si(Li) detector

4cm

25cm

neutrons (FWHM~3%, [2]) of an average energy of 14.8MeV were generated with the pulsed mode on the zero degree line. The prototype was placed on the line at a distance of 141 cm from the target (see Fig. 2-3). To monitor the flux and energy spectrum of the neutrons at this angle, several kinds of activation foils (Al, Ni and Nb) and 'time-of-flight' (TOF) neutron monitor (NE213) were placed at a distance of 21cm and 646cm from the target, respectively.

Figure 2-4 shows the block diagram of the electronics system at the calibration experiment for the prototype. Three signals, (ΔT, L_1 and L_2), are measured in the system. The ΔT-signal corresponds to the TOF of the particle between the ΔE-detector and the tritium target. The signal is obtained by measuring the time difference between the signal from ΔE-detector signal and that from the accelerator's pick-up-ring (target signal). The target signal was delayed by GDG (gate and delay generator) modules. Therefore, the events due to faster particles appear right hand side of ΔT spectra (Fig.2-6). The L_1- and L_2-signal are linear signals of the ΔE- and E-detector, respectively. Here, a linear signal is a detector output signal whose pulse height relates to the energy deposit of a charged particle in the detector. Those three signals are digitized by three CAMAC 'analog to digital converters (ADC)' using 'event-by-event' mode with a common gate signal, which is generated with the coincidence event between ΔE- and E-detector, and stored in a personal computer in the vector form of (L_1, L_2, ΔT).

The signal of ΔE-detector was obtained through two PMT's, where the fast coincidence technique was applied to eliminate PMT noises. The bias voltages of PMT's were adjusted so that the linear signals from them would have the same pulse height for the Compton edge of [137]Cs γ-ray. The zero offsets of the electronic system in the L_1 and L_2 signals were determined by using mercury pulsar.

16
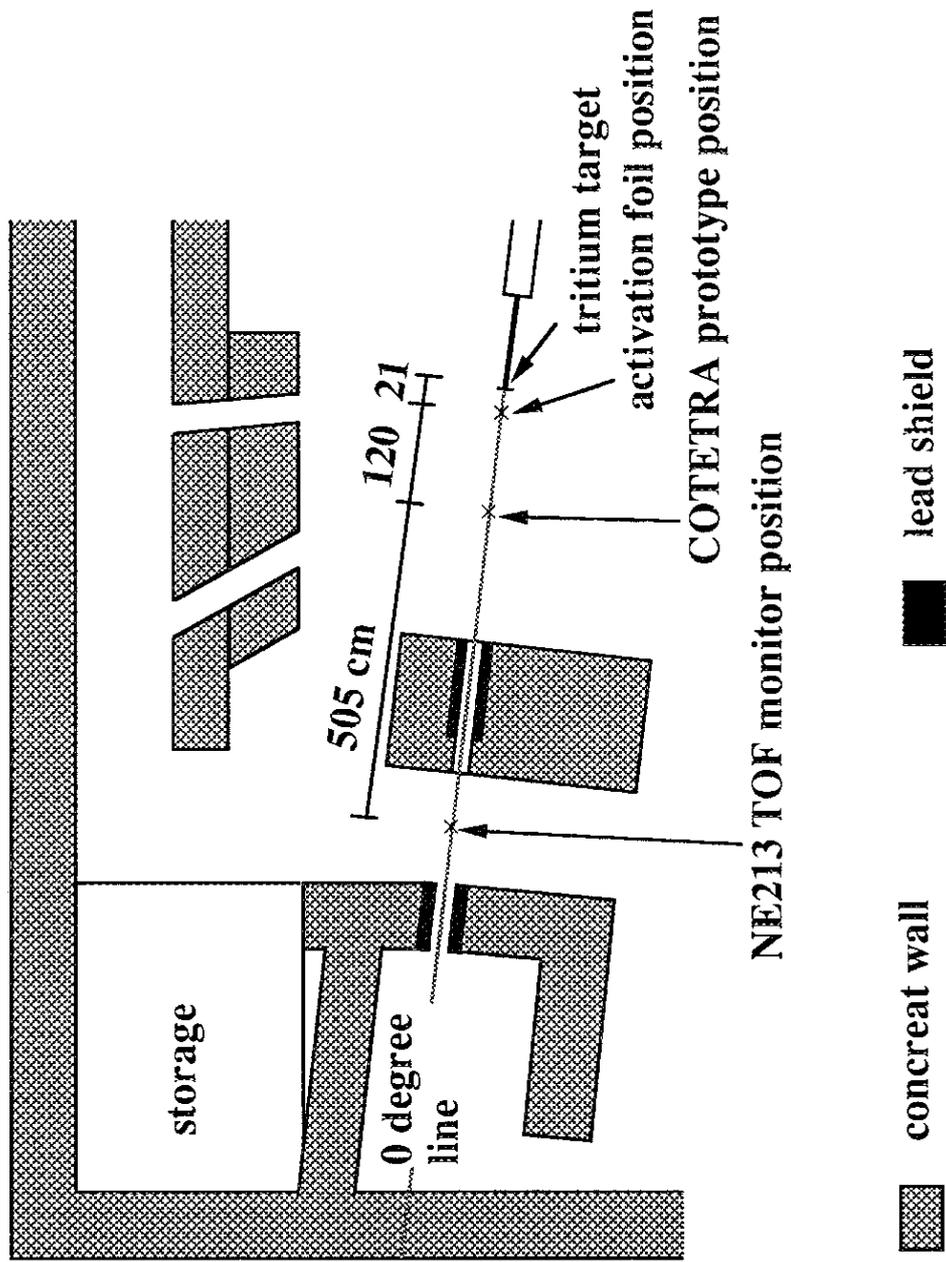
Fig. 2-3 Schematic layout of the experimental set up for the prototype calibration. The distances from the prototype, activation foil and TOF monitor to the tritium target are 141cm, 21cm and 646 cm, respectively.

17
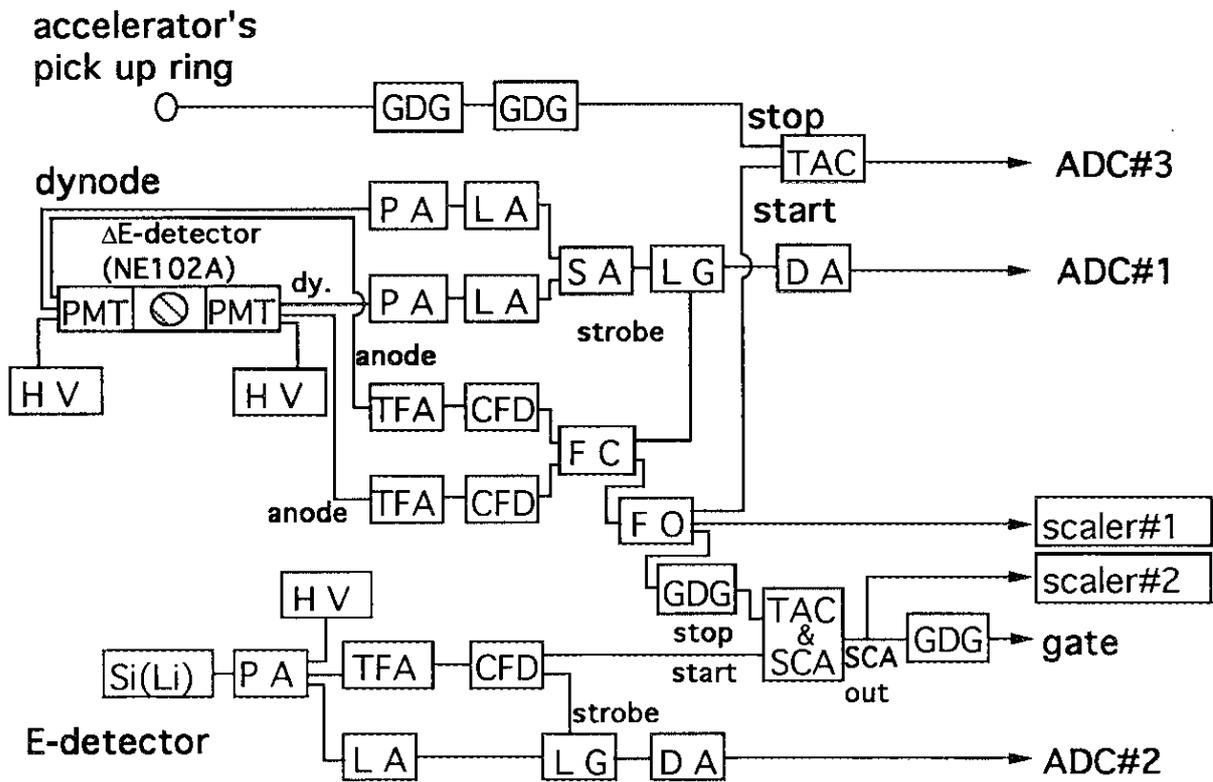
Fig. 2-4 A block diagram of the spectrometer electronic system. The labels shown in this figure are; **GDG**: gate and delay generator, **TAC**: time to amplitude converter, **PMT**: photo multiplier tube, **HV**: high voltage power supply, **PA**: pre-amplifier, **LA**: linear amplifier, **SA**: sum amplifier, **LG**: linear gate, **DA**: delay amplifier, **TFA**: timing filter amplifier, **CFD**: constant fraction discriminator, **FC**: fast coincidence, **FO**: fan out, **TAC&SCA**: TAC and single channel analyzer, **Si(Li)**: lithium drifted silicon semiconductor detector, and **ADC**: analog to digital converter.

The counting rate of ΔE-detector (CR_1) and the coincidence rate of ΔE- and E-detector (CR_{co}) were recorded by scalar #1 and #2, respectively. They are used to estimate the detection efficiency and accidental coincidence rate of the prototype system.

c) Result of Calibration Experiment

Figure 2-5 shows an example of (L_1, L_2) distribution obtained in the experiment. As is expected from eq.(2-2), events due to D-T neutrons appear around the line indicated by ℓ with a certain broadening of $\Delta L_{(L_1,L_2)}$ in Fig.2-5(a). This broadening was mainly caused by the energy resolutions of ΔE-detector.

The data shown in Fig.2-5(a) includes all events, i.e., the events due to the target γ-rays, the accidental coincidences and the true coincidences. Here, the *accidental coincidence* means the coincidence between a ΔE-detector signal being generated by a charged particle and an E-detector signal by another charged particle, while the *true coincidence* means the coincidence between ΔE- and E-detector signals due to one charged particle which crosses through both detectors. The events due to the neutrons can be distinguished from those due to the target γ-rays using associated ΔT-signals because the velocities of γ-rays and D-T neutrons are different (Fig. 2-6). Fig.2-5(b) shows the (L_1, L_2) distribution of γ-ray events that are identified by ΔT-signals and Fig.2-5(c) shows that of neutron events. The γ-ray events concentrate around the lower left side corner of the distribution because ΔE- and E-detector do not have enough thickness for their Compton electrons to lose large amount of their energy. Using this feature, we can easily discriminate γ-ray events from D-T neutron events without using the ΔT signal. This is a big advantage of COTETRA.

To determine the effect of accidental coincidence, the background run was also performed, where a tantalum plate of 0.5mm thickness was

19
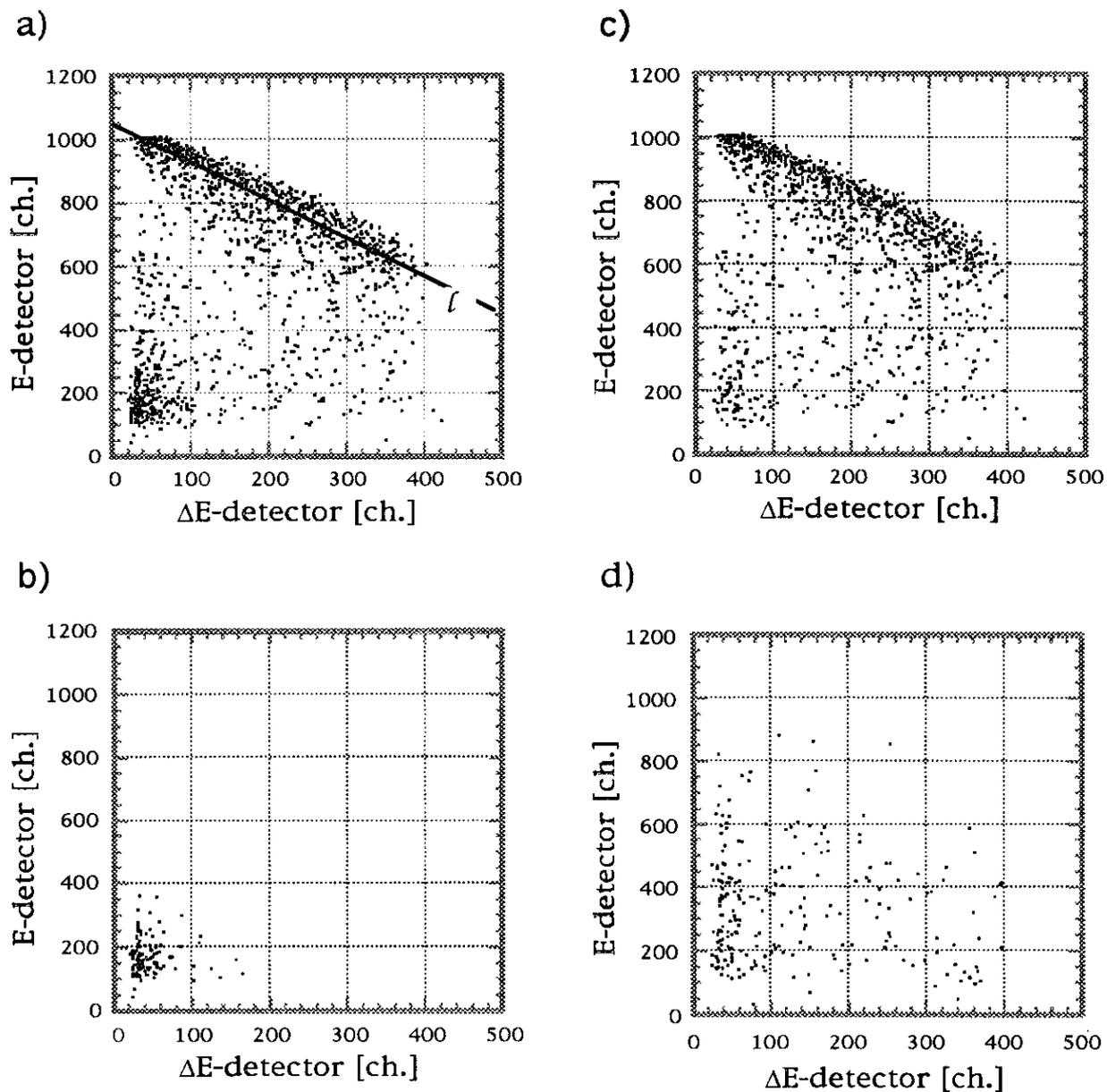
Fig. 2-5 Obtained (L_1, L_2) distribution. Because of the walk of the timing signals from the PMT's in ΔE-detector, the higher portion of the L_1 signal were lost. The distributions (a), (b) and (c) were obtained through the foreground run. The distribution (a) is due to whole events, (b) to γ-ray events, and (c) to neutron events. The distribution (d) was obtained through background run which express the (L_1, L_2) distribution due to the accidental coincidence events. The γ-ray events are eliminated in the distribution (d).

a)

b)
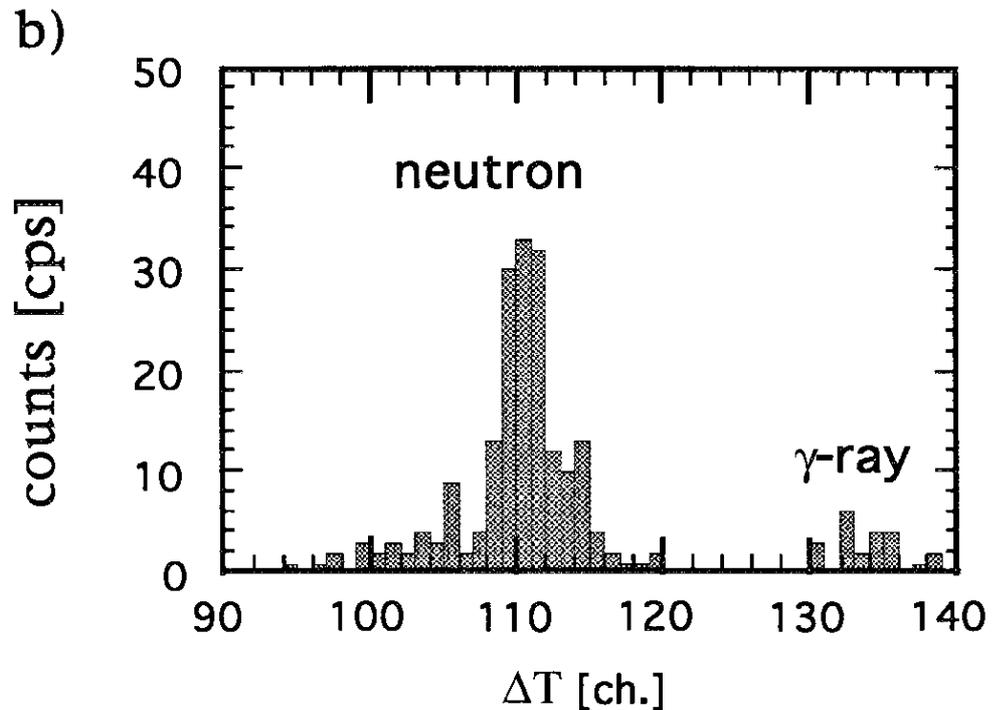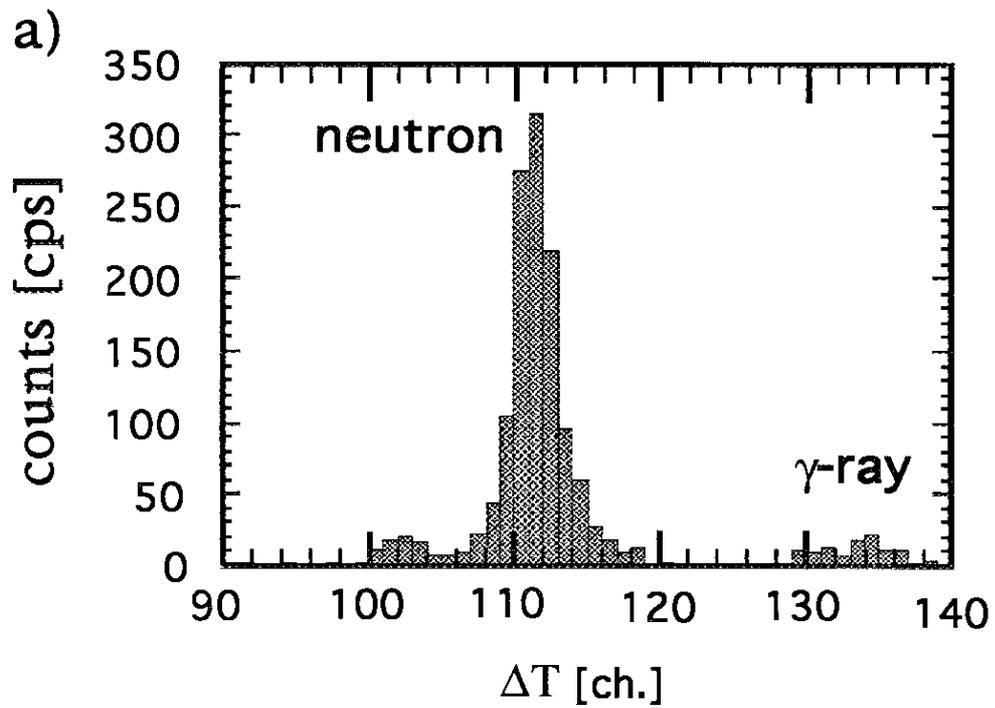
Fig. 2-6 TOF spectra of neutrons and γ-rays which flew to ΔE-detector from tritium target at the calibration experiment of the prototype. The ΔT is the time difference between the ΔE-detector signal and the delayed accelerator's pick-up ring. Events due to fast particles appear right hand side of the figures.
(a) spectrum obtained for foreground run. (b) that obtained for background run.

placed between ΔE- and E-detector. For the sake of convenience, we will call the experiment being performed without placing the tantalum plate as the foreground run. Figure 2-5(d) shows the result of background run, where γ-ray events being identified by ΔT signals are already removed.

Figure 2-7(a) and (b) show the one-dimensional pulse height spectra (PHS) which are obtained by projecting the points in Fig.2-5 (c) and (d) onto the vertical axis (L_2-axis) along the line l, where line l is determined so that it gives the minimum FWHM of the peak in the one dimensional PHS of foreground run. The pulse height spectrum of foreground run is normalized with the measurement time, on the other hand that of the background run is normalized by the measurement time and the count rate of ΔE-detector so that it has the same source intensity as the foreground run does. The zero points of the electronic system are also projected onto L_2-axis and they locate at -2.78 ± 0.04 [ch.] in these figures. Fig.2-7 (c) shows the PHS due to the true events, which is obtained after the subtraction of the background PHS from the foreground PHS.

2.3 Monte Carlo Simulation of Neutron Detection Process for COTETRA

a) Calculation Model

A Monte Carlo calculation code, which simulates the detection process of COTETRA, was developed to estimate the energy resolution and the detection efficiency. In the calculation, ΔE- and E-detector are modeled by two disks of thickness t_1 and t_2, and of radii r_1 and r_2, respectively. The angular distribution of proton recoiled by the neutron in ΔE-detector is treated as isotropic in the center-of-mass system. Multiple scattering of the neutron in ΔE-detector is not considered since its probability is very small compared to single scattering.
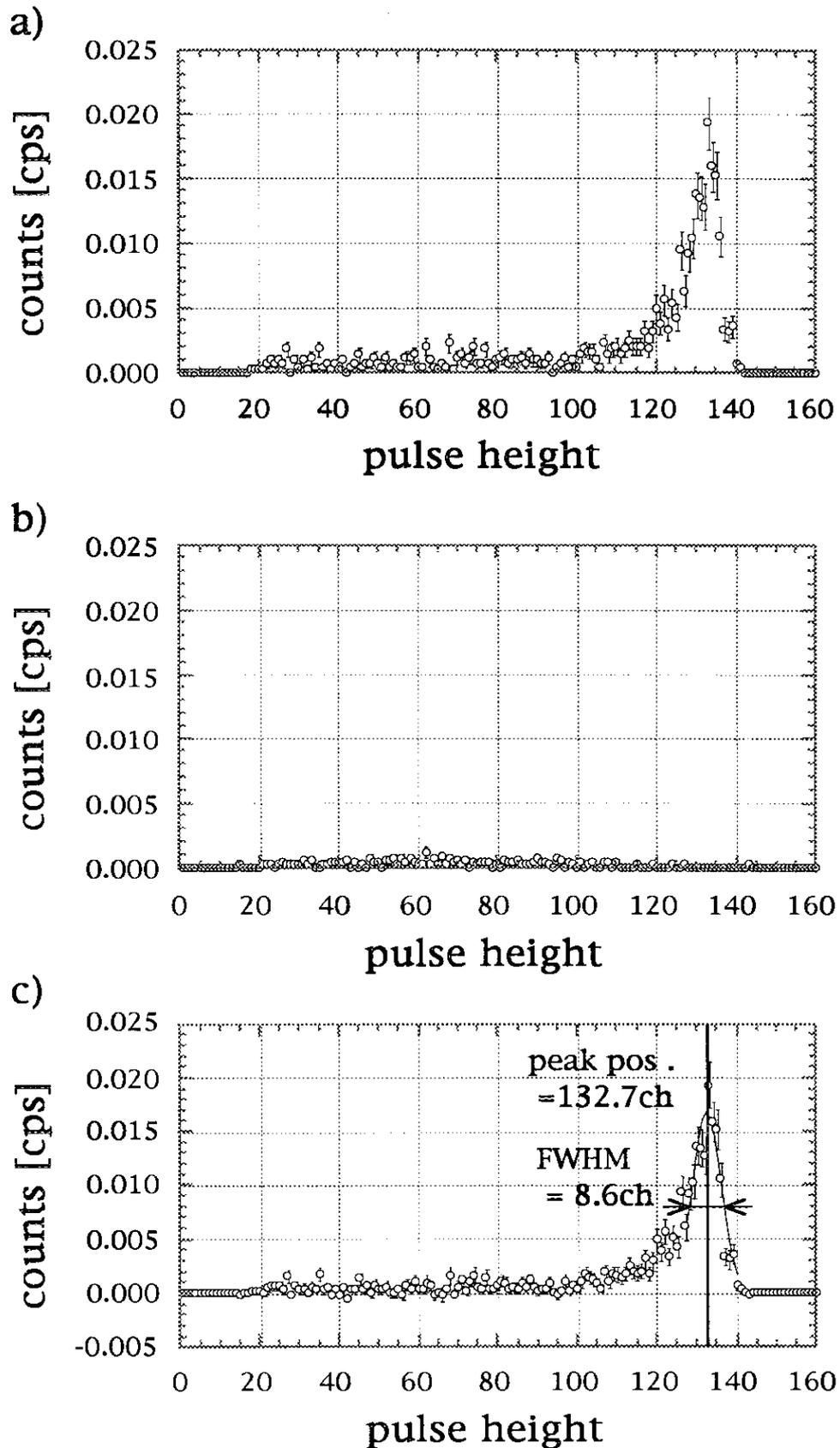
a)

b)

c)

Fig. 2-7 One dimensional pulse height spectra of neutrons for (a) foreground run, (b) background run and (c) true events. Both in (a) and (b), the γ-ray events are already removed. The PHS (c) is obtained by subtracting the PHS (b) from (a).

The energy distribution of (E_1, E_2) is calculated by the Monte Carlo code for a certain incident neutron energy (E_n), where E_1 and E_2 are energy deposits of a recoil proton in ΔE- and E- detector, respectively. Using this distribution in eq.(2-4) and (2-5), the energy resolution of COTETRA can be calculated for a given neutron energy, where the energy resolution of each ΔE- and E-detector (ΔE_i: i=1 for ΔE- detector, and i=2 for E-detector) is assumed to be proportional to the square root of the energy deposit in each detector (Appendix B), i.e.,

$$\Delta E_i = \alpha_i \, (E_i)^{1/2}. \qquad (2\text{-}7)$$

The α_i is a proportional constant, and is intrinsic to each detector. It should be determined experimentally.

The detection efficiency of COTETRA is obtained from eq.(2-6). In the Monte Carlo code, the η_1 is calculated using following formula

$$\eta_1 = S_1 \Sigma_p \{1\text{-}\exp(-\Sigma_t t_1)\}/\Sigma_t, \qquad (2\text{-}8)$$

where S_1 : the area of ΔE-detector,

t_1 :thickness of ΔE-detector,

Σ_p :macroscopic n-p scattering cross section of ΔE-detector, and

Σ_t :macroscopic total cross section of ΔE-detector.

'Japanese Evaluated Nuclear Data Library version 3', JENDL-3 [3], was adopted as a neutron cross section data set in the calculation. The probability $\overline{\varepsilon_{geo}}$ was averaged over the whole volume of ΔE-detector,

$$\overline{\varepsilon_{geo}} = \int_{V_1} \varepsilon_{geo(r,\vartheta,z)} r\, dr\, d\vartheta\, dz \Big/ V_1, \qquad (2\text{-}9)$$

where V_1 : the volume of ΔE-detector, and

$\varepsilon_{geo(r,\vartheta,z)}$: the probability of a proton recoiled at (r, θ, z) in ΔE-detector enters into E-detector.

Here, the small correction due to the attenuation of incoming neutron flux at z was made. This integration was carried out using the Monte Carlo method.

b) Calculation for COTETRA

Using the Monte Carlo code, the energy resolution and the detection efficiency for 14.1-MeV neutron were surveyed by changing the thickness of ΔE-detector (t_1) and the distance between detectors (d). Here, the α of NE102A which is directly connected to a PMT is used as α_1. The catalog value of the energy resolution of SSBD is used to estimate α_2. They are shown in Table 2-2 as ideal values of α's. These α's give better performances than those of the prototype and suggest the achievable limit of energy resolution and detection efficiency with the improvements of detectors used in the prototype.

Table 2-2 Resolution parameter, α, as defined by Eq. (7). In an ideal model, the measured FWHM of NE102A that is directly connected to the PMT is used to estimate the α_1 and a FWHM of SSBD obtained from a catalog was used for α_2. The α_1 of the prototype is estimated by measuring the FWHM of ΔE-detector using internal conversion electrons from ^{137}Cs and [207]Bi, and the α_2 is estimated from the FWHM of E-detector for α-particles of [241]Am. For set-A and -B, α_1 is considered to be equal to the α_1 of the prototype. The α_2 of set-A is estimated from the FWHM shown on the catalog of the SSBD used, and that of set-B is considered to be equal to the α_1 of the ideal model.

	α_1 (ΔE-detector) [MeV$^{1/2}$]	α_2 (E-detector) [MeV$^{1/2}$]
Ideal	2.76×10^{-1}	6.84×10^{-3}
Prototype	3.98×10^{-1}	2.34×10^{-2}
Set-A	3.98×10^{-1}	7.71×10^{-3}
Set-B	3.98×10^{-1}	2.76×10^{-1}

The Table 2-3 shows sizes of detectors in the calculation. Figure 2-8 shows the result of the calculation. The total energy resolution and detection efficiency are expressed with contours. In general, the total

25

a)

Distance between ΔE- and E-detectors: d [mm]

300

250

200

150

100

0.2

0.4

0.6

0.8

1.0

2.0

0.5 1.0 1.5 2.0 2.5 3.0

Thickness of ΔE-detector: t_1 [mm]

b)

Distance between ΔE- and E-detectors: d [mm]

300

250

200

150

100

2%

3%

4%

5%

6%

0.5 1.0 1.5 2.0 2.5 3.0

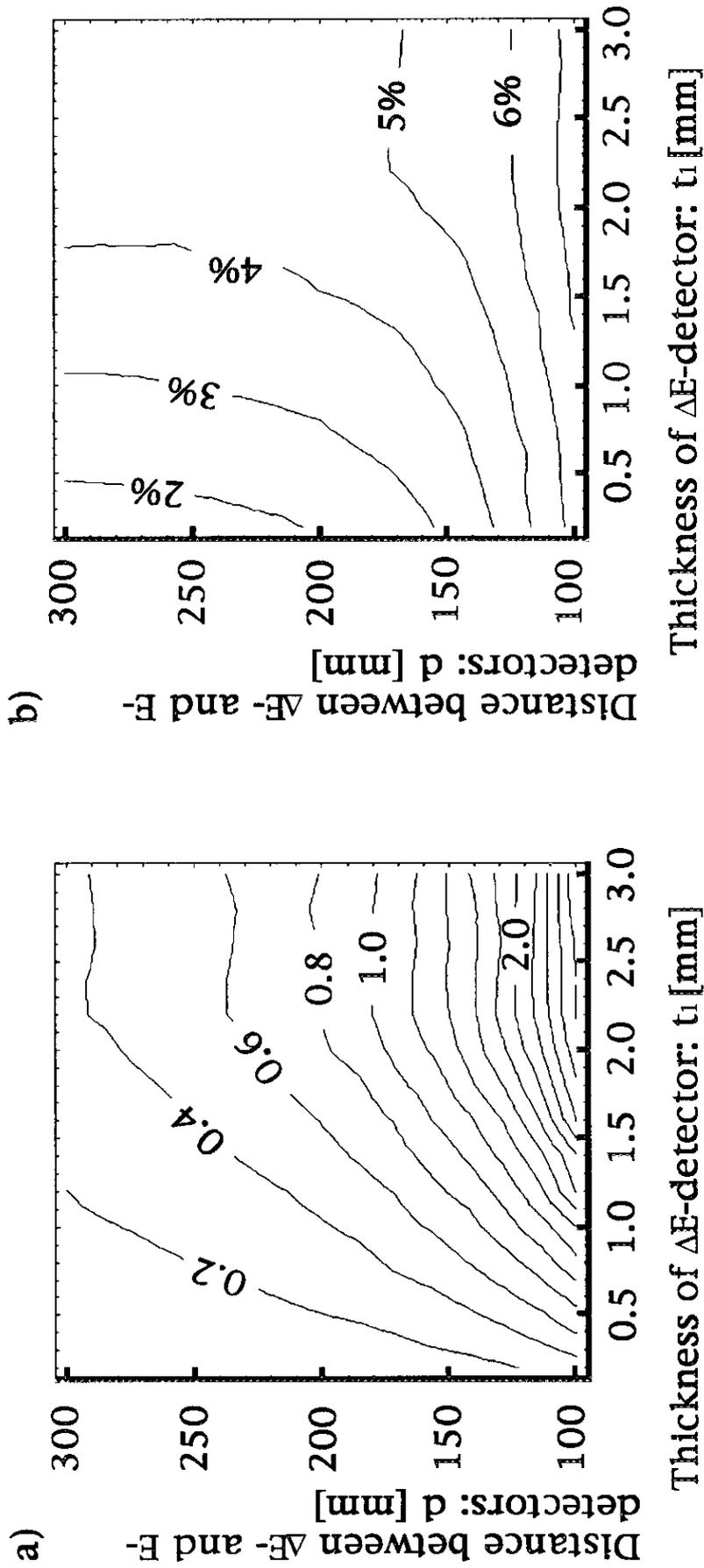Thickness of ΔE-detector: t_1 [mm]

Fig.2-8 (a) Change of calculated detection efficiency η_{tot} [$\times 10^{-4}$ counts/(n/cm^2)] vs. the thickness t_1 of ΔE-detector and the distance d between ΔE- and E-detector. (b) Change of calculated energy resolution $\Delta E_{tot}/E$ [%] vs. t_1 and d. In both cases, α's of Ideal Model were used and the energy of the neutron is 14.1 MeV.

26

resolution and the detection efficiency increase as t_1 increases and as d decreases. Both $\Delta E_{tot}/E$ and η_{tot} do not change with t_1 when t_1 is larger than ~2mm. This length is equivalent to the range of 14.1-MeV proton in NE102A. When t_1 is larger than the range of the recoil proton, there exists a 'Dead Region'. Protons produced here cannot reach E-detector. As these protons only generate accidental coincidence signals, the thickness of ΔE-detector should be chosen carefully in accordance with the energy range of the neutron that we are interested in.

Table 2-3 Sizes of the ΔE- and E-detector used in the calculation. The thickness (t_1) and the distance (d) were varied from 0.2mm to 3mm and from 100mm to 300mm, respectively.

	ΔE-detector	E-detector
Radius (r) [mm]	20	20
Thickness (t) [mm]	0.2 - 3 (varied)	3

The increase of ΔE_{tot} with t_1 is due to the increase of the average ratio of E_1 to E_p, $<E_1/E_p>_{12}$, because the energy resolution of E-detector was better than that of ΔE-detector in the calculation. This average ratio expresses the amount of the contribution of ΔE-detector to the total energy resolution of the spectrometer.

It can be seen in Fig.2-8(a) that COTETRA may fulfill the requirement of the total detection efficiency, i.e., $\eta_{tot} > 10^{-5}$ [counts/(n/cm^2)], at any point of the calculated region and that it may also satisfy the requirement of the energy resolution, i.e., $\Delta E_{tot}/E \leq 3\%$, in a sub region of Fig.2-8(b).

c) Comparison of Calculation with the Experimental Results for the Prototype

The energy resolution of the prototype is estimated to be 4.8% by the calculation, where α_1 is determined for ΔE-detector of prototype by

calibration experiments using internal conversion electrons (ICE) from ^{137}Cs and α_2 is for E-detector by using α-particles from ^{241}Am. These α's are shown in Table 2-2. The detection efficiencies are also calculated for the prototype. The calculated values of η_{tot}, η_1 and $\overline{\varepsilon_{geo}}$ are 1.2×10^{-4} [counts/(n/cm^2)], 8.9×10^{-2} [counts/(n/cm^2)] and 1.3×10^{-3}, respectively.

The peak position of the PHS in Fig. 2-7(c) is set to be 14.8MeV, since it is observed that the energy of the neutrons is about 14.8MeV by the NE213 TOF measurement on the same neutron flight path and this agrees with the theoretical prediction. By using this result, this PHS is transformed to the neutron energy spectrum as shown in Fig.2-9, where the energy dependence of efficiency is taken into account. The latter was calculated by the Monte Carlo Code and is shown in Fig.2-10.

The FWHM of the DT peak in Fig.2-9 is 0.91 ± 0.10MeV, i.e., $6.1\pm0.7\%$. Considering that the energy broadening of the source neutron was about $3.0\pm0.4\%$ [2] in this kind of experiment at OKTAVIAN, the total energy resolution of the prototype spectrometer is estimated to $5.3\pm0.9\%$. This agrees with the Monte Carlo prediction (4.8%) within its margin of error.

The experimental detection efficiencies of COTETRA were determined from the count rates (CR's) and the neutron flux (ϕ) using the following equations:

$$\eta_{tot} = CR_{co}^{true} / \phi, \tag{2-10}$$

$$\eta_1 = CR_1^{true} / \phi, \text{ and} \tag{2-11}$$

$$\overline{\varepsilon_{geo}} = CR_{co}^{true} / CR_1^{true}, \tag{2-12}$$

where the neutron flux (ϕ) was measured using activation foils and was $(2.6\pm0.2) \times 10^3$ [n/cm^2/sec] at the place where the prototype was placed. Using the count rate of Detector #1 (CR$_1$) and the coincidence rate (CR$_{co}$)
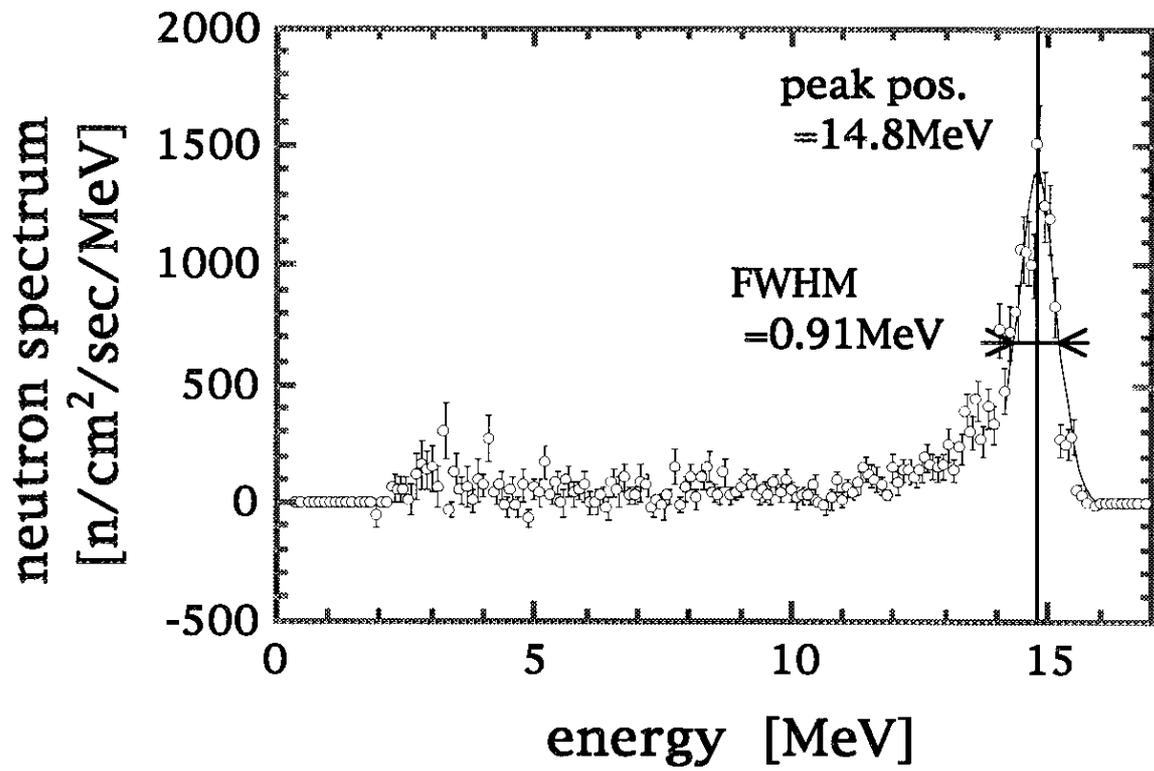
28

Fig. 2-9 Obtained neutron spectrum for D-T neutron at the calibration experiment of the prototype
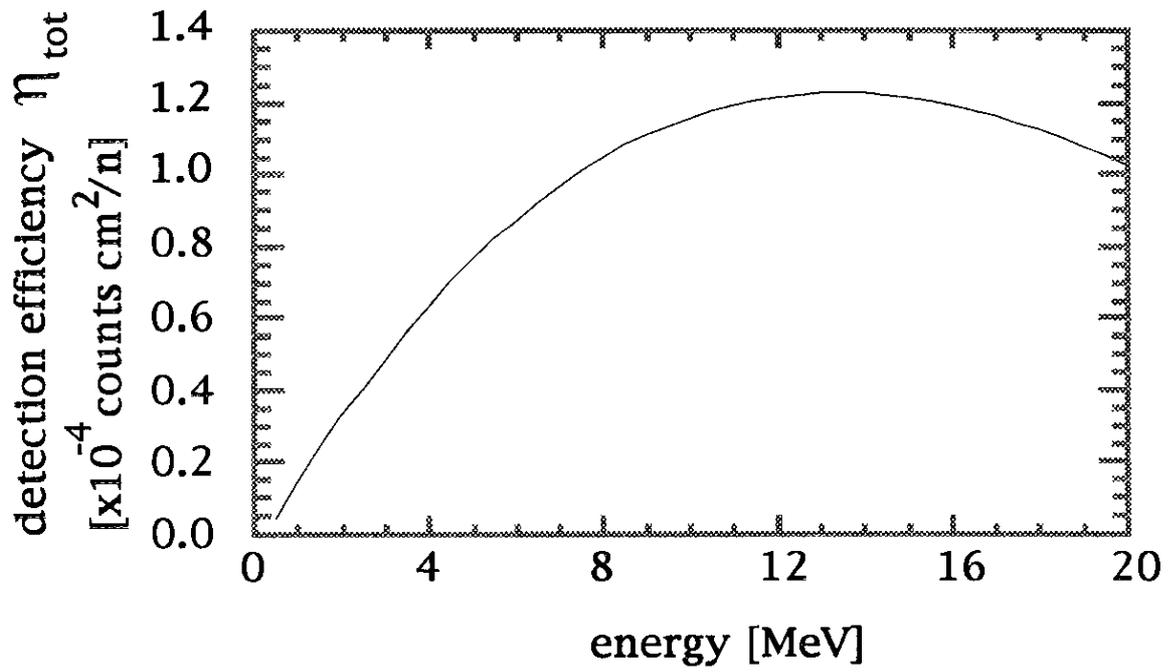
Fig. 2-10 Calculated detection efficiency : η_{tot} [counts/(n/cm ^{2})] of the prototype spectrometer. The loss of events due to the walk of signals from ΔE-detector is considered in the calculation.

of the foreground and background run, the count rate due to the true events (CR_1^{true}, CR_{co}^{true}) can be expressed as follows:

$$CR_1^{true} = r_n^{fore} CR_1^{fore}, \text{ and} \qquad (2\text{-}13)$$

$$CR_{co}^{true} = r_n^{fore} CR_{co}^{fore} - f r_n^{back} CR_{co}^{back}. \qquad (2\text{-}14)$$

Here, the neutron ratio, r_n, is the ratio of the neutron events to total events and is obtained from the data shown in Fig. 2-6. The CR_1 and CR_{co} are shown in Table 2-4, together with r_n. The correction factor (f), which eliminates the effect of the source intensity difference between foreground and background runs, can be expressed:

$$f = (CR_1^{fore} / CR_1^{back})^2. \qquad (2\text{-}15)$$

The experimental detection efficiencies, i.e., η_{tot}, η_1 and $\overline{\varepsilon_{geo}}$, are $(1.3\pm0.2)\times10^{-4}$ [counts/(n/cm^2)], $(1.0\pm0.1)\times10^{-1}$ [counts/(n/cm^2)] and $(1.3\pm0.1)\times10^{-3}$, respectively. They agree with the Monte Carlo prediction within their margin of error. These results in the detection efficiency and the energy resolution are summarized in Table 2-5.

Table 2-4   List of CR and r_n. Ratios of neutron events to total events (r_n) are obtained from the data shown in Fig. 2-6.

	Count Rate of #1 CR_1 [cps]	Coincidence Rate CR_{co} [cps]	neutron ratio: r_n
Foreground run	320.2±0.3	0.46±0.02	0.83±0.03
Background run	330.2±0.3	0.057±0.004	0.78±0.08
True events	265±11	0.34±0.04	-

Table 2-5   The performances of the prototype spectrometer for 14.8-MeV neutron.

	$\Delta E_{tot}/E$ [%]	η_{tot} [counts/(n/cm^2)]	η_1 [counts/(n/cm^2)]	ε_{geo}
Experiment	5.3±0.9	$(1.3\pm0.2)\times10^{-4}$	$(1.0\pm0.1)\times10^{-1}$	$(1.3\pm0.1)\times10^{-3}$
Calculation	4.8	1.2×10^{-4}	8.9×10^{-2}	1.3×10^{-3}

The count rate capability of the whole spectrometer system (CR_{tot}^{cap}) is determined by the product of the count rate capability of ΔE-detector (CR_1^{cap}) and the geometrical detection efficiency ($\overline{\varepsilon_{geo}}$):

$$CR_{tot}^{cap} = CR_1^{cap}\,\overline{\varepsilon_{geo}}. \qquad (2\text{-}16)$$

The CR_1^{cap} depends on the count rate capability of the NIM modules used, and was about 10^5 cps. Since $\overline{\varepsilon_{geo}}$ of the prototype was about 10^{-3}, the CR_{tot}^{cap} of the present system was about 10^2 cps. This capability was not enough for fusion plasma diagnostics. Further improvements on the count rate capability of the prototype system, especially of NIM modules, are necessary.

2.4 Development of COTETRA for TFTR D-T Experiments

a) COTETRA for TFTR D-T experiments

For TFTR D-T experiments, two sets of detectors, set-A and set-B were prepared as shown in Fig.2-11[4]. Set-A utilizes a NE102A plastic scintillator with thickness of 0.5mm and diameter of 13mm as a ΔE-detector and a Silicon Surface Barrier Detector (SSBD: effective area of 100mm² and thickness of 2mm) as an E-detector. Set-B also uses a NE102A plastic scintillator for a ΔE-detector but with thickness of 2mm and diameter of 13mm. For set-B, the E-detector is also a NE102A plastic scintillator. Since the SSBD has better energy resolution than NE102A, set-A will provide better neutron energy resolution. Set-A has a thinner ΔE-detector than set-B in order to increase the ratio of the energy that is deposited by a recoil proton in the E-detector to the total incident energy, which is the sum of the energy deposits in both the ΔE- and E-detector.

Schematic block diagrams of the NIM modules for both sets were shown in Fig.2-12, where we have applied fast electronic techniques.
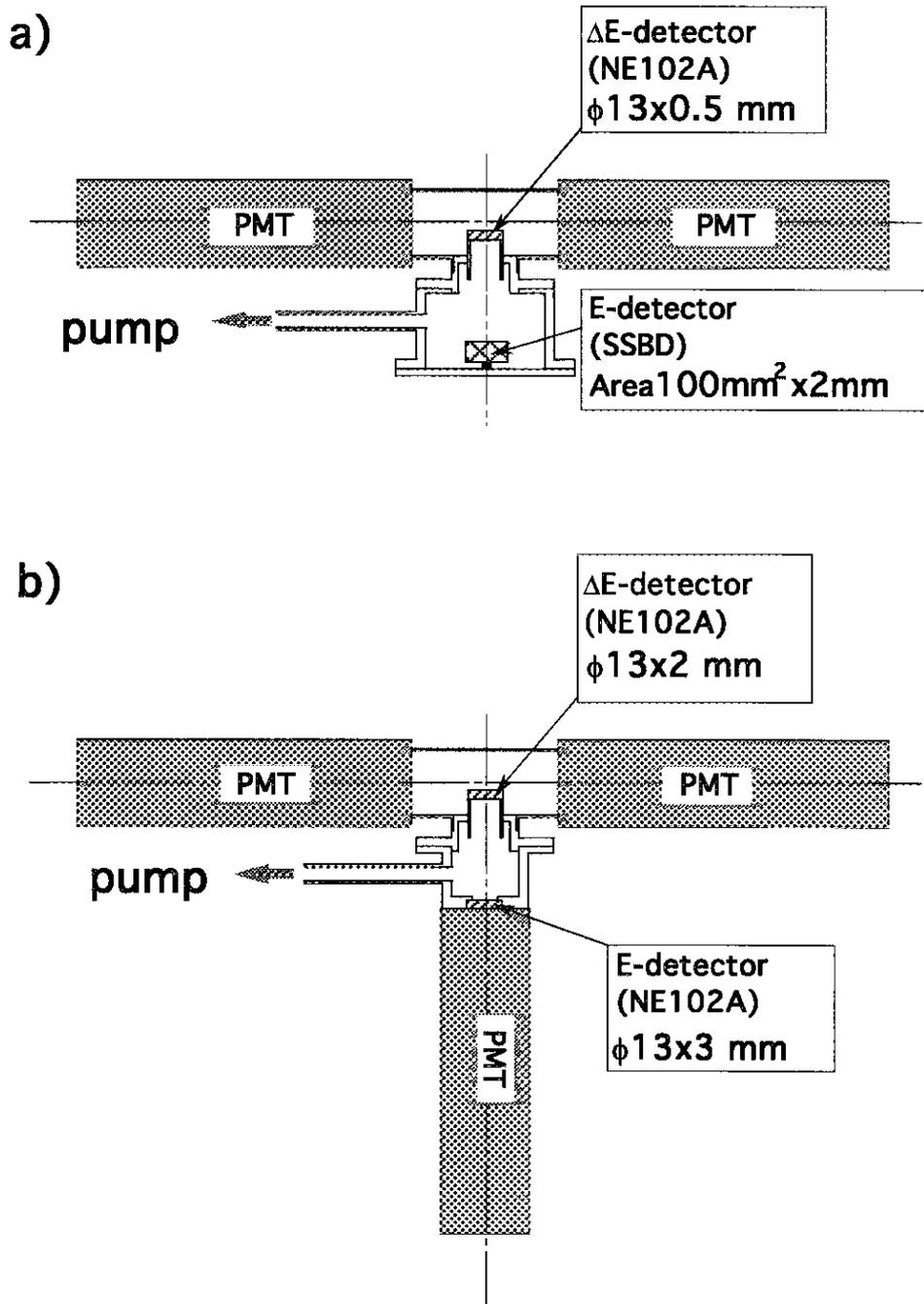
32

Fig.2-11 Schematic drawings of COTETRA for TFTR D-T experiments. (a) Set-A has better energy resolution, and (b) set-B has better counting rate capability and detection efficiency.
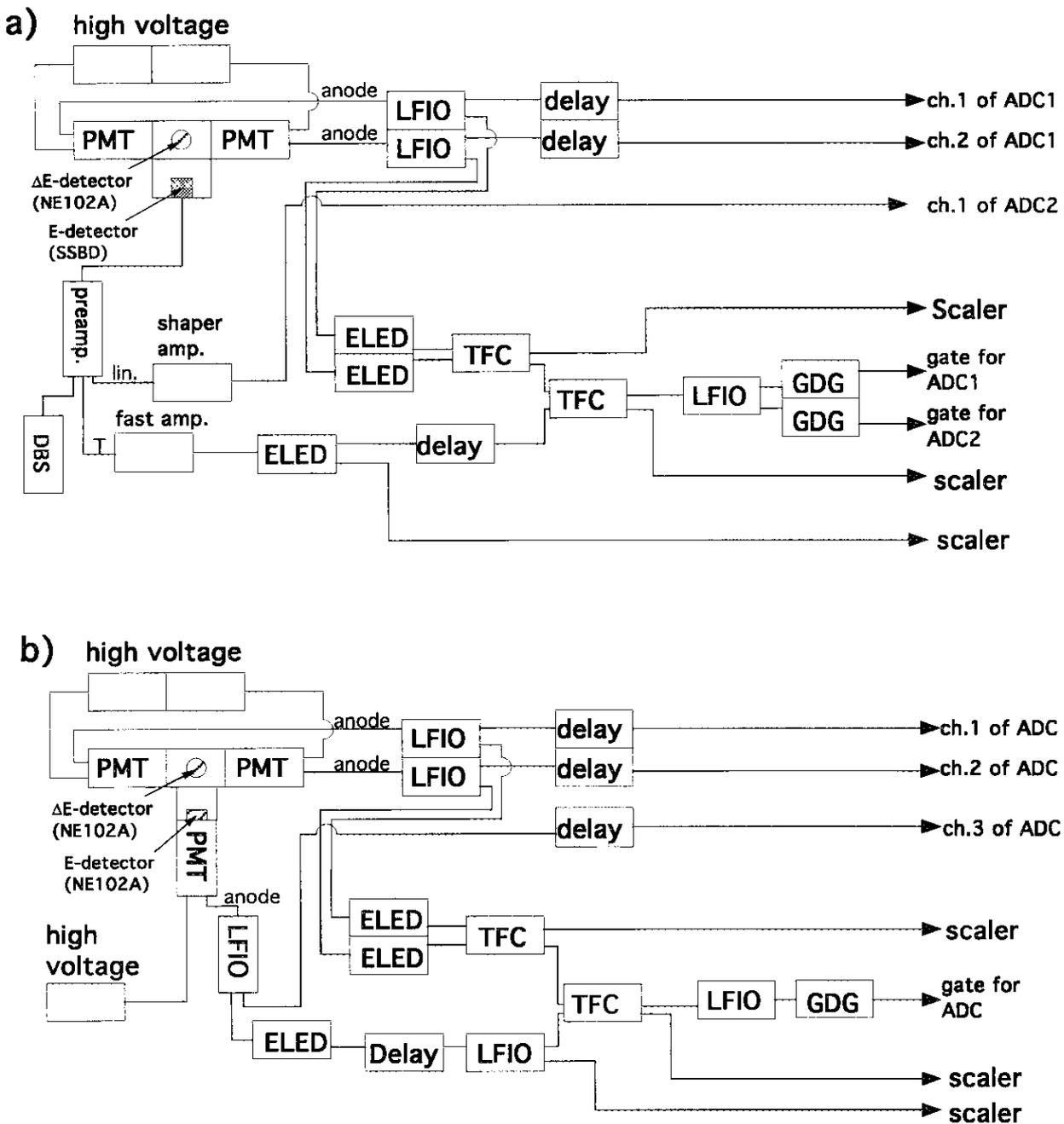
a) high voltage

b) high voltage

Fig. 2-12 Block diagrams for COTETRA (a) set-A and (b)set-B on the calibration experiment at OKTAVIAN. The labels shown in these figures are; **PMT**: photo multiplier tube, **SSBD**: silicon surface barrier detector, **DBS**: detector bias supply, **CG**: clock generator, **ELED**: extrapolated leading edge discriminator, **LFIO**: linear fan in and out, **TFC**: two fold coincidence, and **GDG**: gate and delay generator.

34

Anode signals of photo multiplier tubes (~10nsec in full width) are directly supplied to a Charge Sensitive Analog to Digital Converter (ADC) with internal memories. This method will enhance the count rate capabilities from the 10^5cps up to 10^7cps. The ADC's are triggered by coincidence signals between the ΔE- and E-detector. The timing signals for the ΔE-detector are produced by the coincidence of the two photo tubes. This triple coincidence among two ΔE-detectors and one E-detector insures that the signal is produced by a real event and not by spurious noise, i.e., thermal electron PMT noise and/or neutron induced PMT noise. The gate width of the ADC is set at 50ns for set-B, which is the minimum requirement for the ADC. A different approach is used for set-A where two ADC's with different gate widths are utilized because of the different rise and fall times of the ΔE- and E-detector. Signals from the ΔE-detector are collected in the first ADC having a gate width of 50ns, while a signal from the E-detector and its associated marker are collected in another ADC with a gate width of 2.5μs. The longer gate width of the E-detector is due to the slow signal from the SSBD. Set-B has greater count rate capability than set-A and is expected to work at up to 10^4cps, as the count rate capability of the scintillator is expected to be around 10MHz and the ratio of the coincidence to the single count of a ΔE-detector is order of 10^{-3}. Set-A is not expected to function at 10^4cps, because of the slow signal from the SSBD.

In addition to the higher count rate capability, set-B has the advantage of easy adjustments of timing signals, since it uses the same type of detectors in both the ΔE- and E-detector.

b) Result of Calibration Experiments for Set-A and -B

A calibration experiment for both detector sets was performed using OKTAVIAN. Each set was placed on the zero degree line with respect to the incident deuterium beam direction, where the energy of the

neutron is around 14.8MeV. A Ni activation foil was placed adjacent to the ΔE-detector, to provide a measurement of the intensity of the neutron flux at the spectrometer position.

Energy spectra obtained are shown in Fig.2-13(a) and (b). The full widths at half maximum (FWHM) of the peaks are 5.5% for set-A and 11% for set-B. In order to determine the source of low energy signal that shows up on the pulse height distribution, a set of data was taken with a 5cm thick polyethylene block placed in front of the detector. Some of the virgin neutrons from the accelerator should be scattered by the block reducing the 14-MeV peak, while neutrons scattered from supporting materials should not be affected by the block. Fig.2-13(c) demonstrates it. The block effectively reduces the 14.8-MeV neutron flux by about a half, while the shape of the 14-MeV peak remains the same. However, the lower energy component between 10 and 14MeV does not change appreciably. Therefore, the lower side tail components below the peaks in Fig.2-13(a) and (b) are considered to be due mainly to the scattering of neutrons at the spectrometer support materials.

Applying a Gaussian fit to the spectra from set-A above 14.3MeV, the FWHM is determined to be ~5.0%. For set-B, using a fitting region above 13.9MeV, the FWHM is seen to be ~10%. Considering the energy spread of the neutron source, which was previously determined to be ~3%, the energy resolution of set-A becomes 4%, and that of set-B is 9.5%. These are consistent with the results of the Monte Carlo calculation[1], which are shown in Table 2-6.
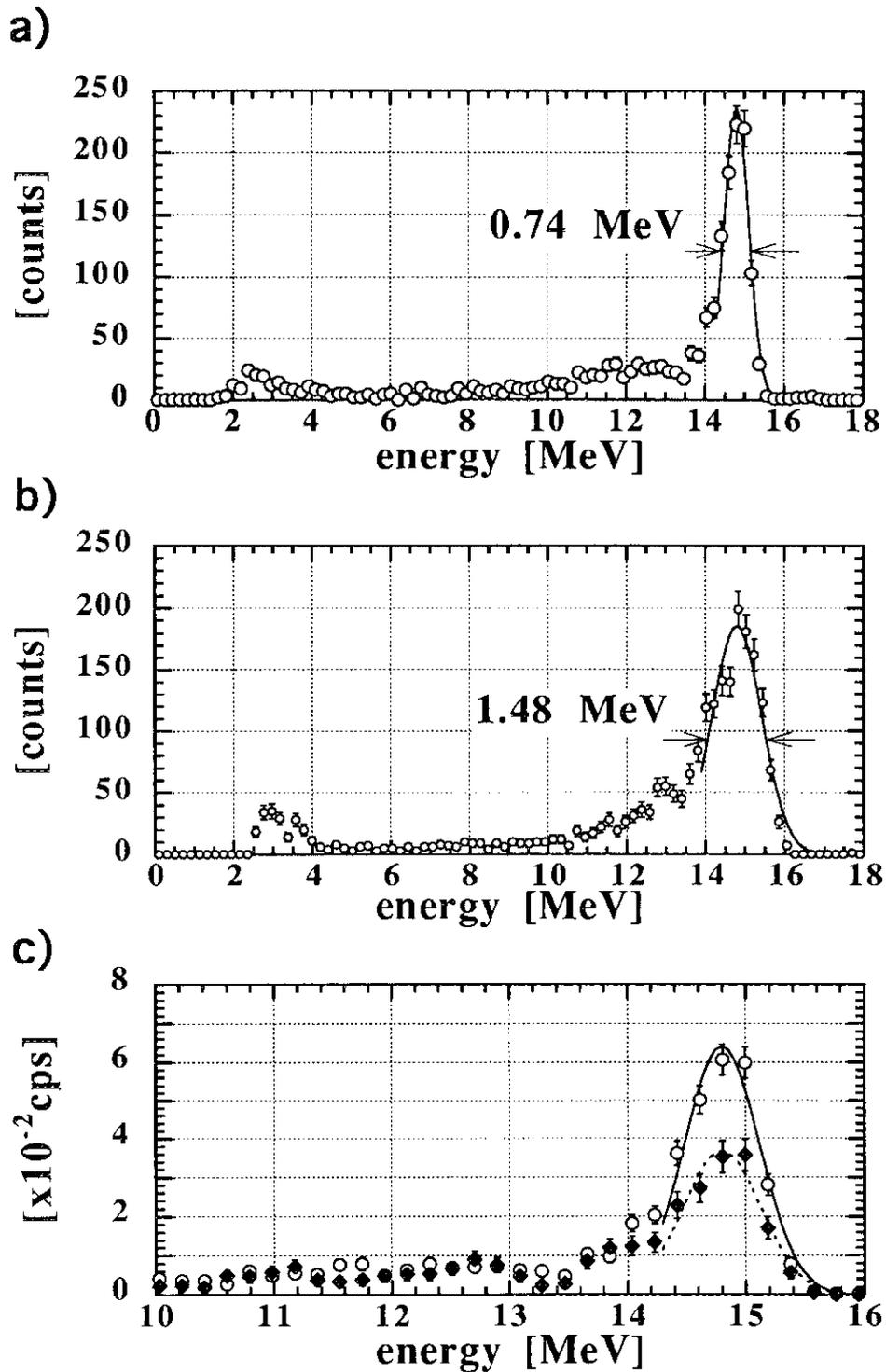
Fig. 2-13 (a) Energy spectra obtained at the calibration experiment for set-A, and (b) that for set-B. Raw data are shown by open circles in these figure. Lines show results of the gaussian fitting with the fitting region of above 14.3-MeV for set-A and 13.9-MeV for set-B. (c) A spectrum for set-A when a polyethylene block is placed in front of the ΔE-detector, shown by closed diamonds, are compared to the spectrum without the block, shown by open circles. The neutron source intensity is almost same in each case and each spectrum is normalized with the measurement time. The solid line shows the fitting of open circles to gaussian curve and the dashed line shows that of closed diamonds.

37

Table 2-6　Obtained energy resolution and detection efficiency for set-A and set-B in calibration experiment.

Type of Sets	Energy Resolution [%]		Detection Efficiency [counts/(n/cm^2)]	
	Experiment	Calculation	Experiment	Calculation
Set-A	3.9%	2.7%	-*	7.6×10^{-6}
Set-B	9.0%	8.5%	6.4×10^{-5}	5.5×10^{-5}

*Experimental detection efficiency for set-A could not be obtained due to the poor statistics of the activation foil measurement.

References

[1] M.Osakabe, *et. al.*, Rev. Sci. Instrum. **65**, 1636 (1994).

[2] A.Takahashi, Private Communication

[3] K.Shibata, *et. al.*, JAERI 1319

[4] M.Osakabe, *et. al.*, Rev. Sci. Instrum. **66**, (1995), to be published in January

[5] C.F.Williamson, *et al.*, CEA-R-3042(1966)

[6] H.H.Anderson, *et. al.*, *Stopping Powers and Ranges vol.3*, Pergamon Press, New York, 1977

Chapter 3

Installation of COTETRA at TFTR

3.1 Outline of TFTR D-T Experiments

The D-T experiment has been performed on TFTR since November 1993 [1-14]. The goals of the experiment are (1)safe operation of tritium handling and processing system and successful machine and diagnostic operation in a high radiation environment of 14-MeV neutron, (2)evaluation of the confinement and the heatings of D-T plasmas, (3)evaluation of the effect of fast α-particles on plasmas, (4)demonstration of 10MW fusion power operation and establishment of its reliable operating regime, and (5) test of the diagnostic for confined α-particles [14]. It is expected that the D-T experiments will provide useful databases in designing ITER and new physics operating regime that could improve tokamak concepts.

In the experiment, tritium was introduced to the torus by gas puffing and/or by neutral beam injection (NBI). There are twelve NBI sources on TFTR. Six aimed in the co-direction, and the other six in the counter-direction. Deuterium and/or tritium can be injected in any combination of these sources. Ion cyclotron range of frequency (ICRF) heating is also provided as an auxiliary heating[11-13].

Several types of neutron measurements are performed on TFTR[15-29]. Total amount of neutron yield is measured by the activation foil system[19,22]. Total neutron emission rates are measured by uranium fission chambers[23]. D-T neutron emission rates are measured by silicon diode detectors[27]. Neutron emission profiles are measured by the detectors in ten-channel neutron collimator. The collimator has three sets of multi-detector system, i.e., ten NE451

39

scintillators, ten ZnS scintillators[15,20,28], and five ^{4}He proportional counters(Fig.3-1)[16,25]. Each of the multi-detector systems has different counting rate capability and neutron sensitivity. Among them, only the ZnS scintillator can survive during the high fusion power D-T experiments. All of these neutron detectors are calibrated *in situ* by positioning a D-T neutron generator at many locations within the vacuum vessel of TFTR[23-25].

3.2 Experimental Arrangement of COTETRA at TFTR

In 1993, both set-A and -B were installed on TFTR under flight tubes of the neutron collimator[29]. The set-A is placed under the flight tube #6, and set-B under the #5 as shown in Fig.3-1. These two channels correspond to the lines of sight at the major radii of 251cm and 265cm, respectively. Both sets are viewing plasmas perpendicularly to the magnetic field line. There are three other neutron detectors on their lines of sight[15,16,20]. However, the spectrum near 14-MeV energy is not expected to be affected, while the virgin fluence is expected to be reduced, as was shown in the calibration experiment at OKTAVIAN (Fig.2-13(c)). In particular, significant degradation in neutron energy would be the result of significant angular scattering which is not possible in the highly collimated environment on TFTR.

Block diagrams of the electronics used on TFTR are shown in Fig.3-2. In the experiments on TFTR, two new functions are added to the data acquisition system. One function provides the information of time for detected events. A continuous train of periodic time scale signals is produced by a clock generator, which is synchronized to the TFTR clock cycle, typically with a 2msec period. This period can be varied from 2msec to 10sec. These time scale signals are independent of COTETRA so that signals generated from COTETRA appear between
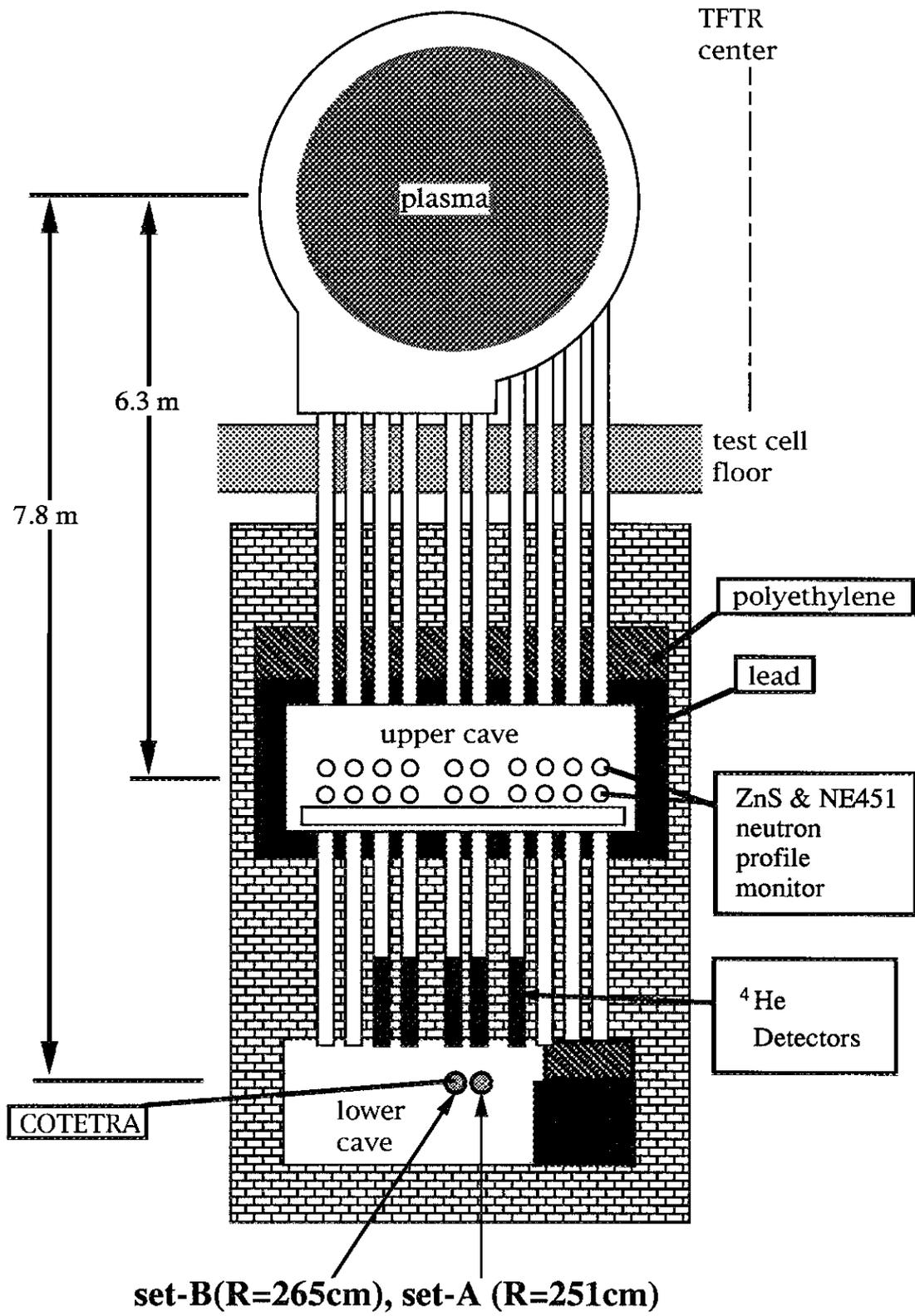
Fig. 3-1 Schematic drawing of multi-channel neutron collimator (MCNC) at Bay-K on TFTR. ZnS and NE451 detectors are installed in the upper cave. ^{4}He propotional counters are installed in the flight tube between upper and lower cave. Set-A of COTETRA is installed in the lower cave under channel #5 and set-B is under channel #6 of the MCNC. These channel correspond to the major radius of 251cm and 265cm, respectively.
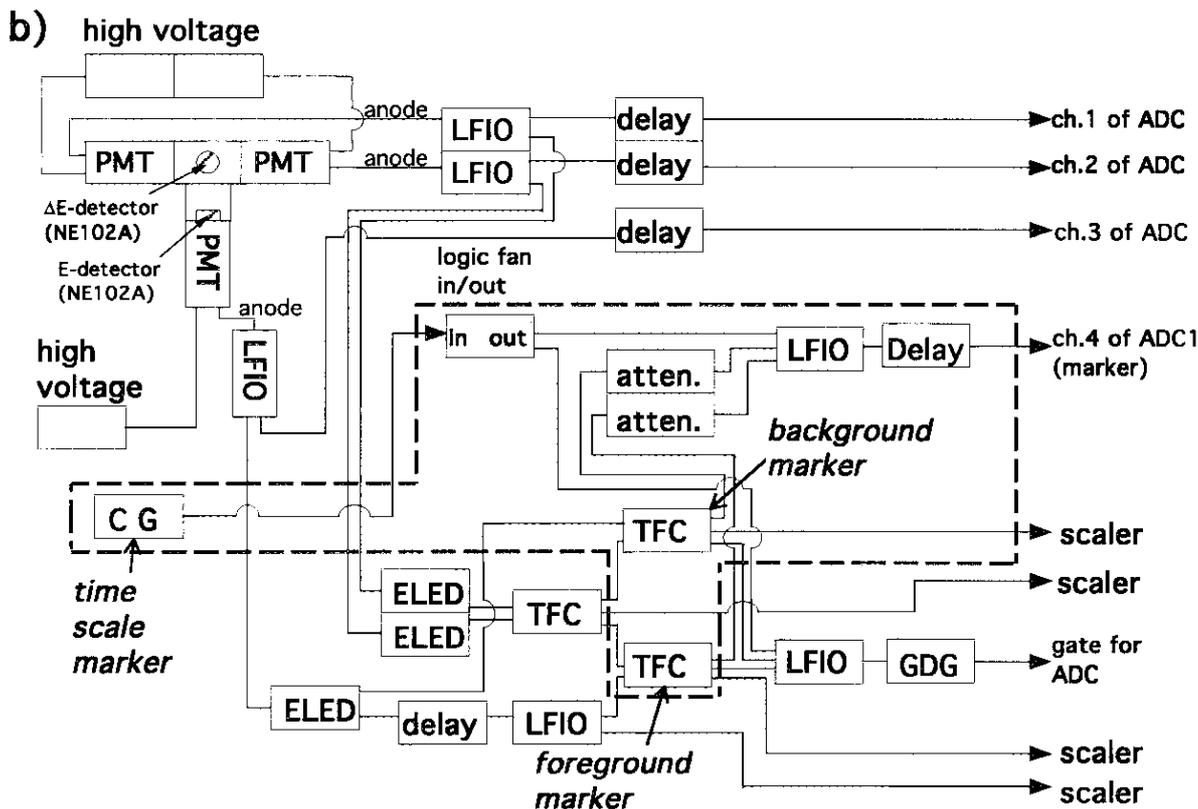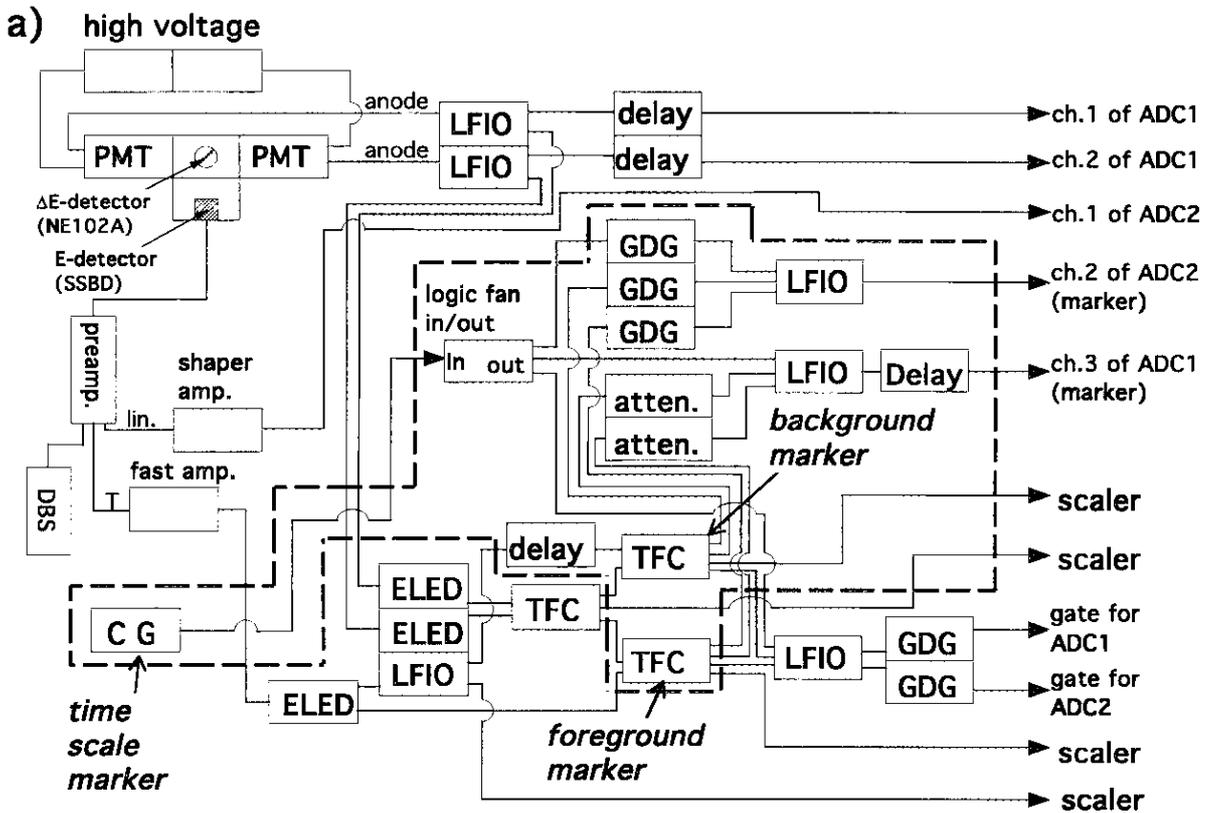
Fig. 3-2 Block diagram for COTETRA (a)set-A and (b)set-B on TFTR. The modules surrounded by the dashed lines are newly applied for TFTR experiments. The labels shown in these figures are; **PMT**: photo multiplier tube, **SSBD**: silicon surface barrier detector, **DBS**: detector bias supply, **CG**: clock generator, **ELED**: extrapolated leading edge discriminator, **LFIO**: linear fan in and out, **TFC**: two fold coincidence, **GDG**: gate and delay generator, **atten.**: attenuator.

them (Fig.3-3). With the help of them, a COTETRA signal can be time-resolved within 2msec.

Another function provides the information of accidental coincidence between ΔE- and E-detector. The accidental coincidence causes serious problem when the neutron flux is extremely high. On the calibration experiment, the effect of accidental coincidence was evaluated by placing a tantalum plate between ΔE- and E-detector. It was not possible to apply this method at TFTR, and the evaluation was made by timing-shift technique. The normal coincidence spectrum was obtained by accumulating the coincidence events of three detectors (two PMT's of the ΔE-detector, and one PMT or SSBD of the E-detector). In this chapter, these events are defined as *foreground events*. On the other hand, the accidental spectrum was obtained from the coincidence events between the ΔE-detector signals and the E-detector signals 10nsec-shifted. These coincidence events are defined as *background events*, here. The evaluation of true coincidence spectrum was made by subtracting the background spectrum from the foreground spectrum. The concept of this technique is shown in Fig.3-4.

Marker signals were provided for those three types of events, i.e., time scale signals, foreground events, and background events. The pulse heights of the markers were set to be different to each other so that those three events were easily identified. They were digitized with the three linear signals from COTETRA (two signals from ΔE-detector and one from E-detector) by a four-channel ADC. These digitized four signals were stored with the vector form of (ΔE_1, ΔE_2, E, marker) in the internal memories of the ADC with 'event-by-event' mode and sent to the VAX computers between the TFTR discharges. As is mentioned, the COTETRA signals, i.e., foreground and background events, generally appeared between time scale signals. Therefore, the linear signals being
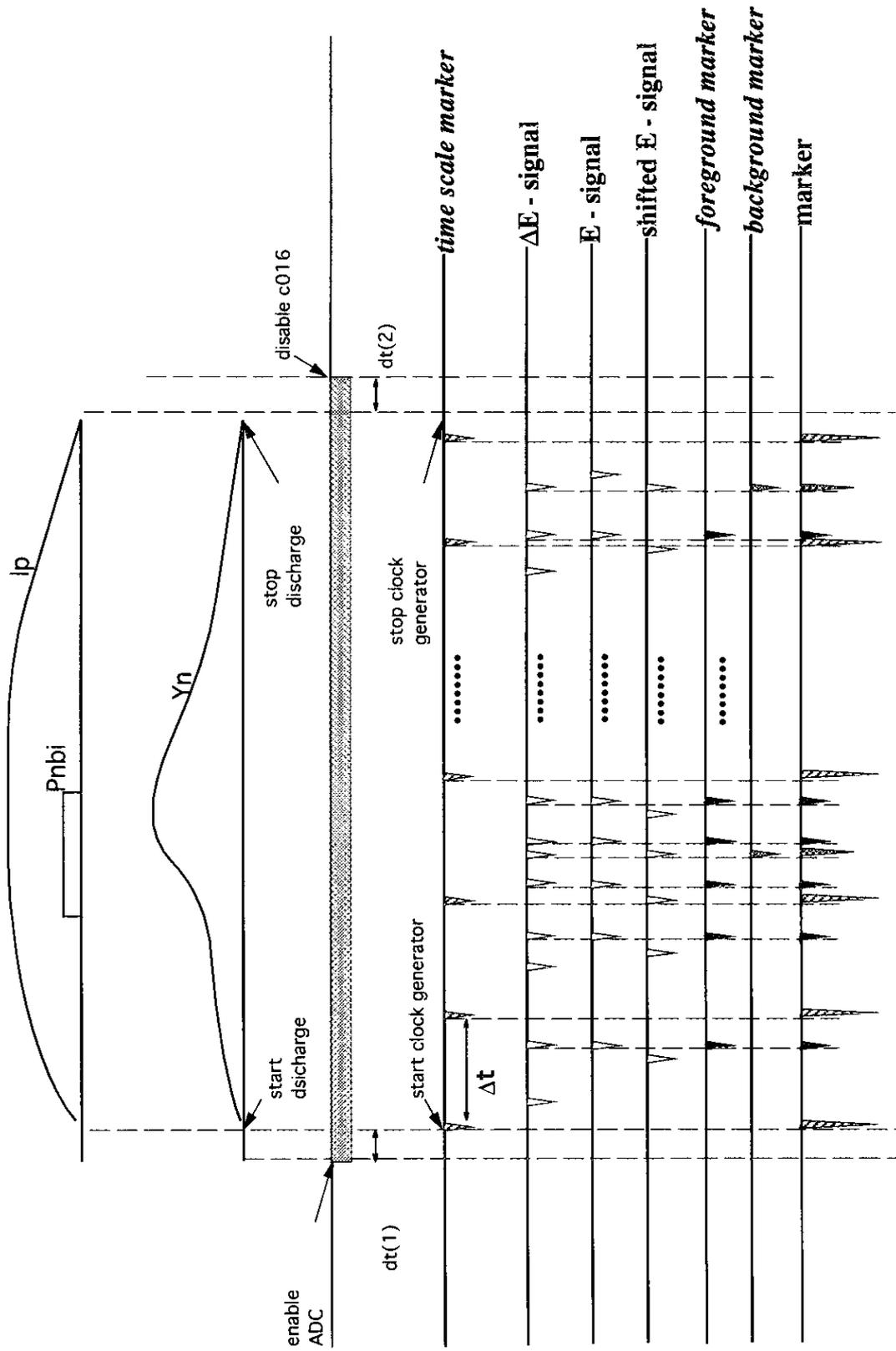
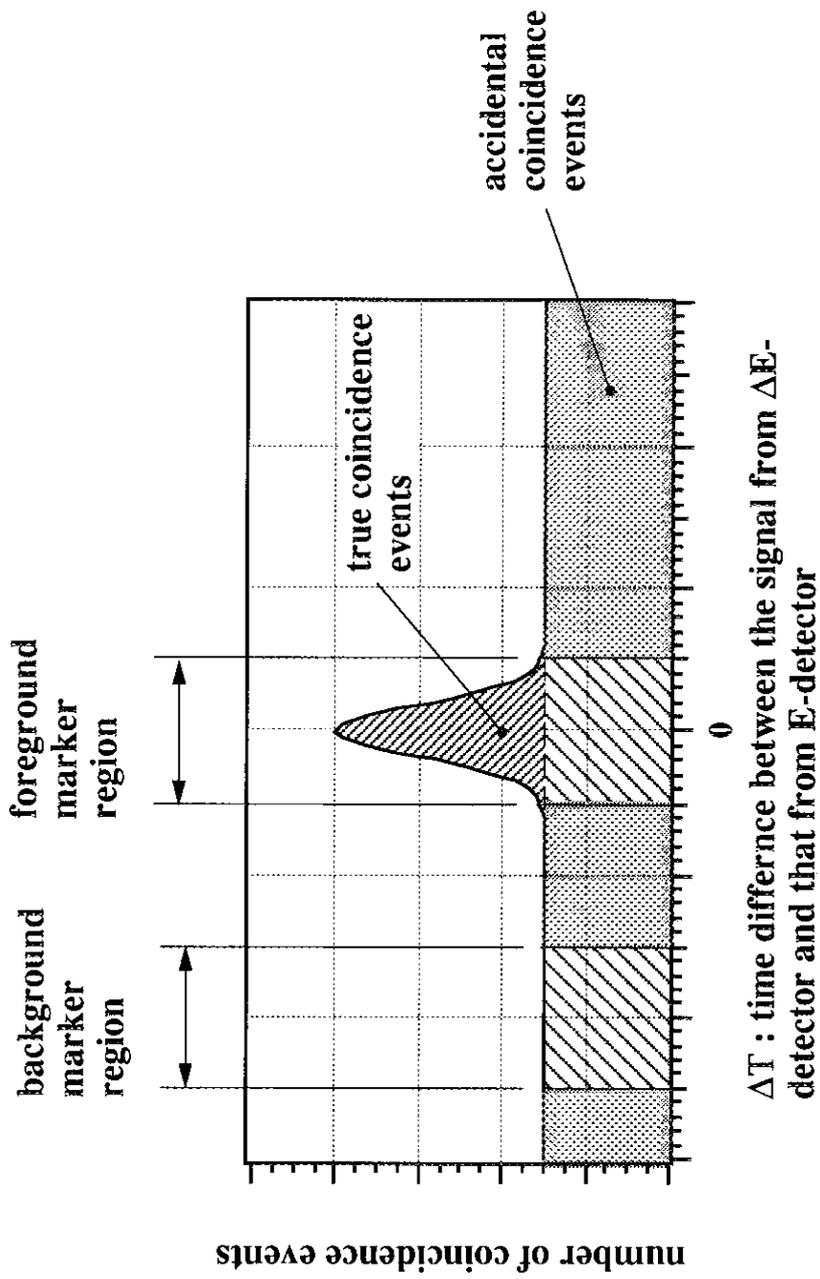Fig.3-3 Schematic relation of mark signals and signals from COTETRA

44

Fig.3-4 Conceptual drawing of the evaluation of true events by foreground and background markers

45

associated with the time scale signals do not have the information of neutron energy but contain the ground level information of the detector signals. Using this information, the ground level fluctuation of COTETRA signals, whose characteristic time is greater than the period of time scale markers, can be evaluated and removed.

3.3 Verification of COTETRA detection system from experimental results

The D-T neutron energy spectra were obtained for three 'NBI and ICRF' heated plasmas (RF-discharges) and for a NBI heated plasma without ICRF heating (NBI-discharge) using set-B. Unfortunately, the activation foil system and the neutron profile monitor of TFTR were not turned on during these discharges. In Fig. 3-5, the time evolution of counting rates of set-B is compared to the D-T neutron emission rates being measured by the Si-diode D-T neutron monitor of TFTR[24,27]. Fig.3-5(a) and (b) show single counting rate of ΔE- and E-detector, respectively. Fig.3-5(c) shows the event rate of true coincidence, which was estimated by subtracting the accidental coincidence rate of ΔE- and E-detector from the coincidence rate of them. The time evolution of counting rates of set-B is in good agreement with that of the Si-diode data. Time scale marker seems to work successfully in obtaining the information of time. Figure 3-6 shows the total counts of set-B vs. D-T neutron emission being measured by Si-diode of TFTR. The total counting efficiency of set-B is estimated to be 6.5×10^{-16} [counts/ neutron emission] by comparing total counts of set-B to the D-T neutron emission. The counting efficiency of set-B for NBI-discharge seems to be a little bit higher than those for RF-discharges. This can be due to the difference of neutron emission profile between these two types of discharges.

a) ΔE-detector
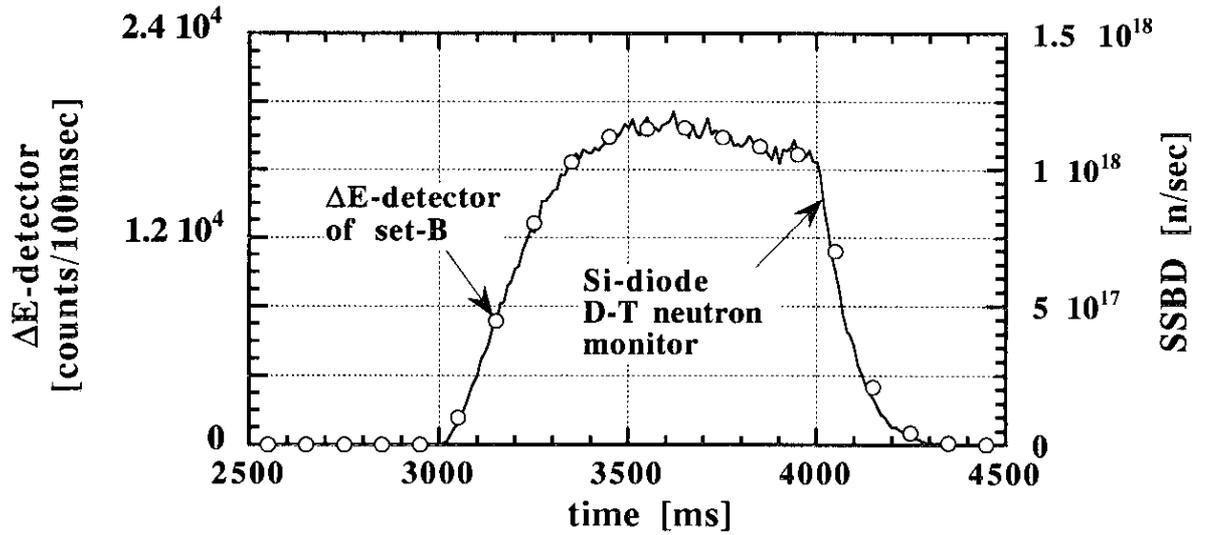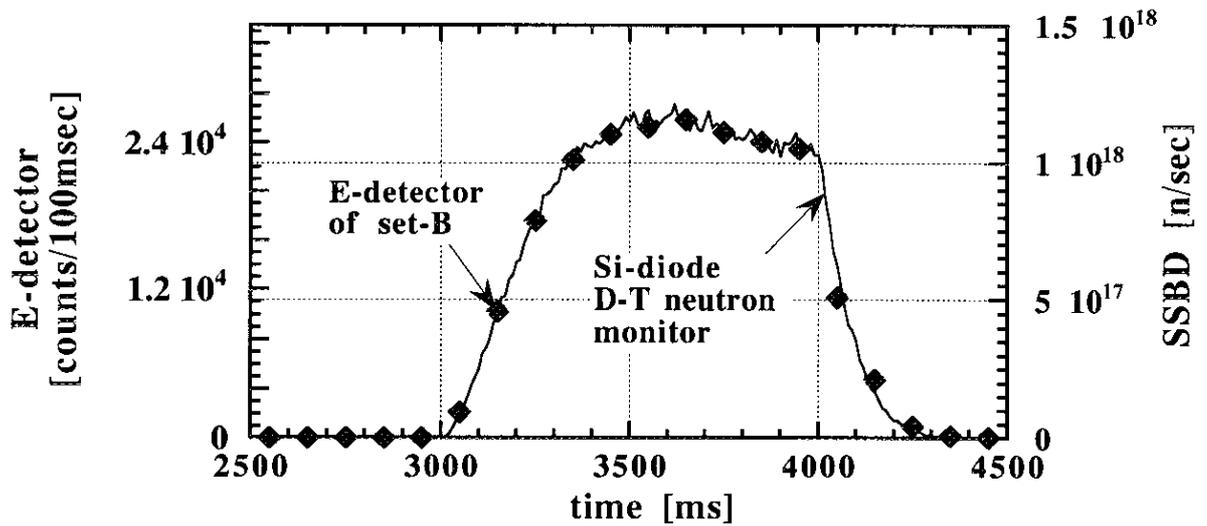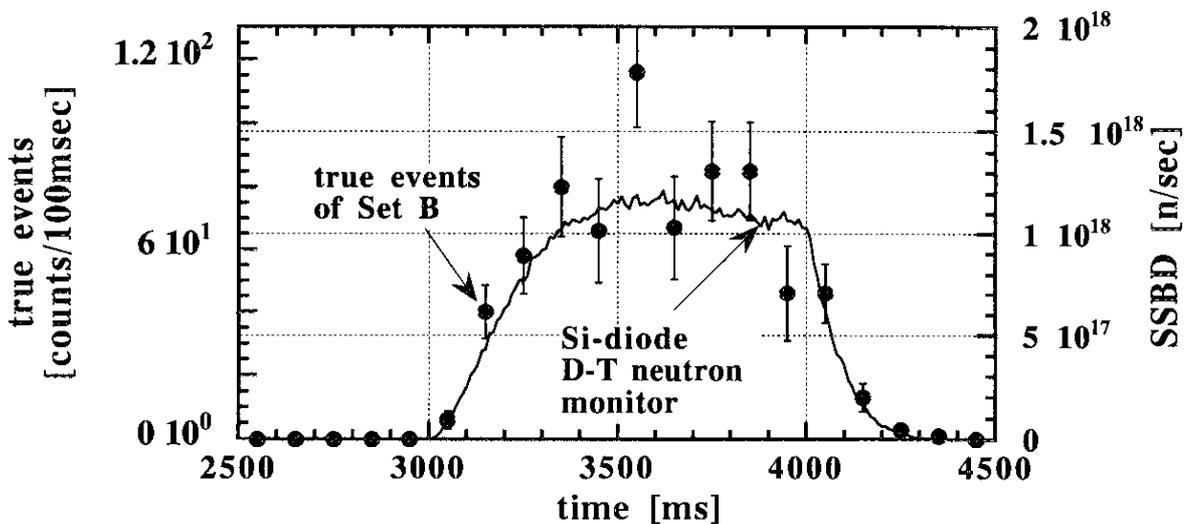

b) E-detector

c) true events

Fig. 3-5 Time evolution of counting rate of (a) ΔE-detector, (b) E-detector, and (c) true events
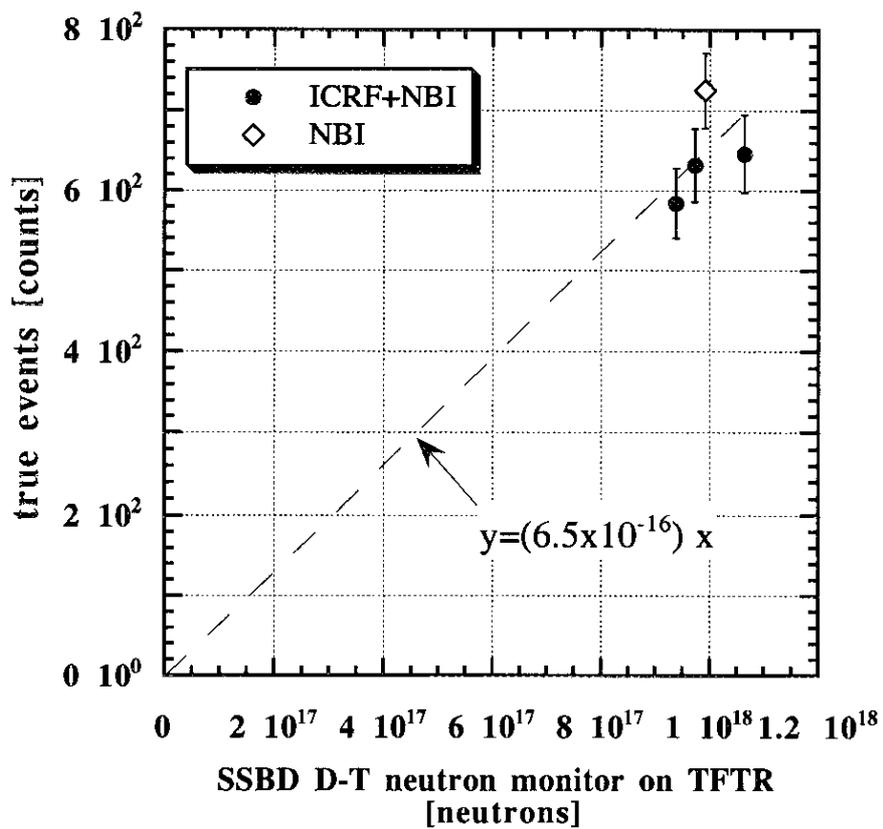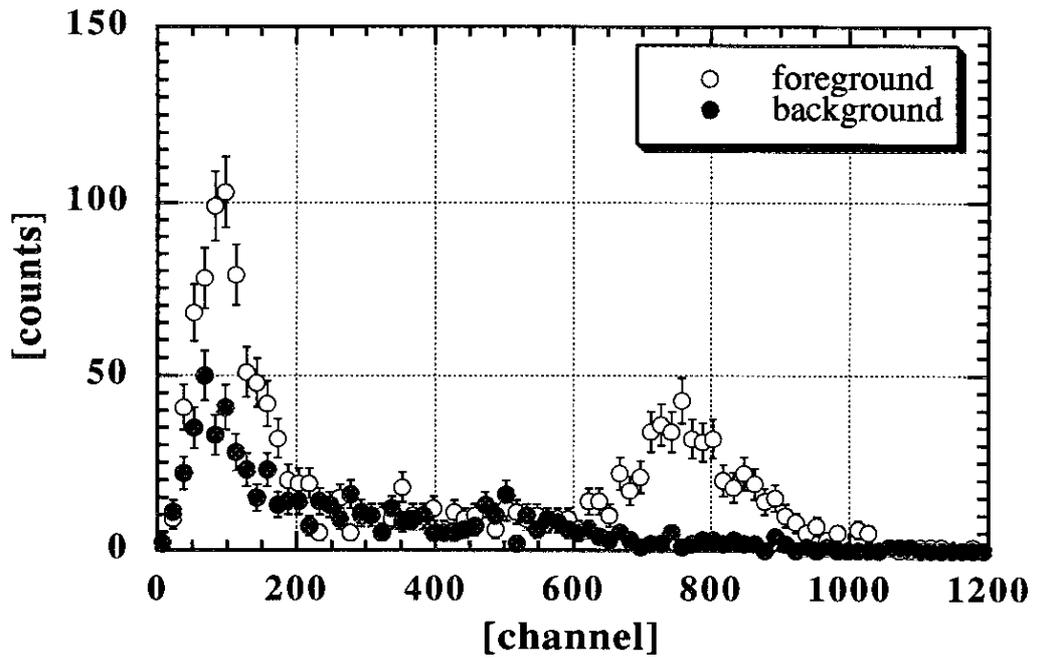
47

Fig.3-6 Total counts of COTETRA set-B vs. D-T neutron yield of TFTR obtained by Si-diode
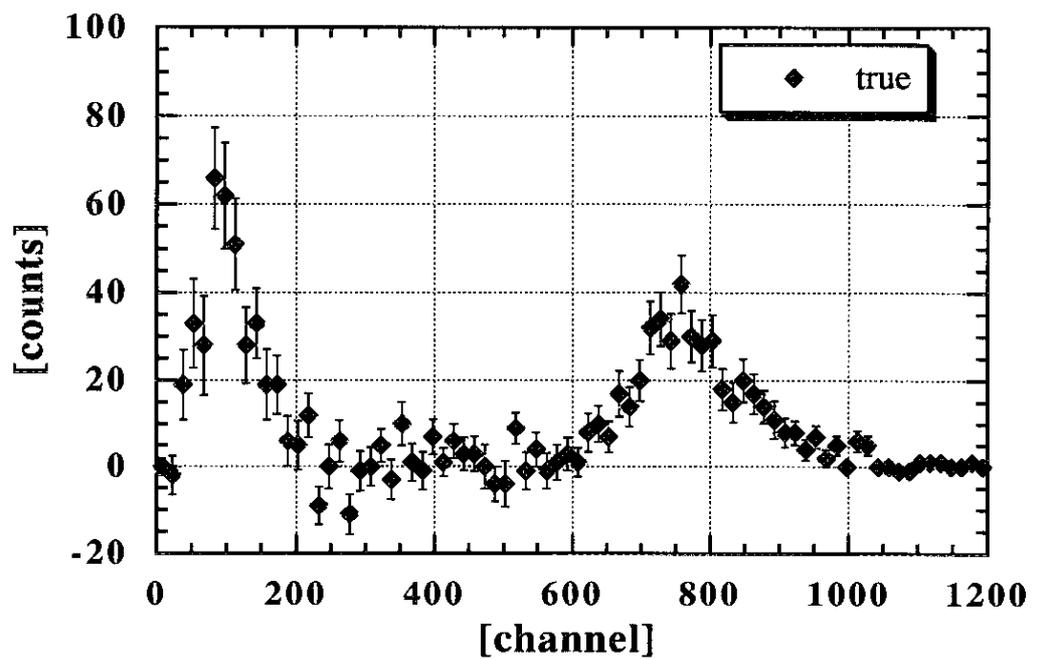
48

a)

b)

Fig. 3-7 Pulse height spectra for (a) foreground and background events, and (b) true events which were obtained by subtraction of background PHS from foreground PHS. These PHS were obtained for an NBI-discharge.

49

The pulse height spectra (PHS) for foreground events and that for background events are shown in Fig. 3-7(a). These are obtained for a NBI-discharge with the count rate of 2000cps. From this figure, the spectrum of the foreground between 5 and 10MeV agrees with that of the background and, therefore, is considered to be due to accidental coincidence events. The evaluation of the accidental coincident events obtained by the sliding timing technique turns to be successful. The low energy counts below 5MeV are considered to be due mainly to background γ-rays.

Because the PMT of E-detector in set-B is located on the flight path of the collimated neutron from TFTR, the neutron may directly induce a signal on PMT. However, the count rate of ΔE- and E-detector of set-B are almost same and this kind of effect seems to be currently negligible.

The broadening of the D-T neutron peak width is discussed in Chapter 5.

References

[1] J.D.Strachan, *et al.*, Physical Review Letters **72**, 3526 (1994)

[2] R.J.Hawryluk, *et al.*, Physical Review Letters **72**, 3530 (1994).

[3] J. Hosea, *et al.*, PPPL-**3013**, (1994)

[4] R.V. Budny, *et al.*, PPPL-**3015**, (1994)

[5] R.J.Hawryluk, *et al.*, IAEA-CN-60/A-1-I-1, 15th International Conference on Plasma Physics and Controlled Nuclear Fusion Research, Seville, Spain, (1994)

[6] M.G.Bell, *et al.*, IAEA-CN-60/A-2-I-1, 15th International Conference on Plasma Physics and Controlled Nuclear Fusion Research, Seville, Spain, (1994)

[7] S.A.Sabbagh, *et al.*, IAEA-CN-60/A-5-I-6, 15th International Conference on Plasma Physics and Controlled Nuclear Fusion Research, Seville, Spain, (1994)

[8] P.C.Efthimion, *et al.*, IAEA-CN-60/A-2-II-6, 15th International Conference on Plasma Physics and Controlled Nuclear Fusion Research, Seville, Spain, (1994)

[9] M.C.Zarnstroff, *et. al.*, IAEA-CN-60/A-2-I-2, 15th International Conference on Plasma Physics and Controlled Nuclear Fusion Research, Seville, Spain, (1994)

[10] E.Fredrickson, *et. al.*, IAEA-CN-60/A-2-II-5, 15th International Conference on Plasma Physics and Controlled Nuclear Fusion Research, Seville, Spain, (1994)

[11] G.Taylor, *et. al.*, IAEA-CN-60/A-3-I-3, 15th International Conference on Plasma Physics and Controlled Nuclear Fusion Research, Seville, Spain, (1994)

[12] R.Majeski, *et. al.*, IAEA-CN-60/A-3-I-4, 15th International Conference on Plasma Physics and Controlled Nuclear Fusion Research, Seville, Spain, (1994)

[13] R.V. Budny, Nuclear Fusion **34**, (1994)

[14] R.J.Hawryluk, *et al.*, Physics of Plasmas **1**,1560 (1994)

[15] A.L.Roquemore, *et al.*, Rev. Sci. Instrum. **61**, 3163 (1990).

[16] J.S.McCauley, *et al.*, Rev. Sci. Instrum. **63**, 4536 (1992).

[17] C.W.Barnes, *et al.*, Rev. Sci. Instrum. **61**, 2383 (1990)

[18] C.W.Barnes, *et al.*, Rev. Sci. Instrum. **61**, 3151 (1990)

[19] C.W.Barnes, *et al.*, Rev. Sci. Instrum. **61**, 3190 (1990)

[20] L.C.Johnson, Rev. Sci. Instrum. **63**, 4517 (1992)

[21] L.P.Ku, *et al.*, Rev. Sci. Instrum. **61**, 3193 (1990)

[22] C.W.Barnes, *et. al.*, Rev. Sci. Instrum. **66**, (1995), to be published in January

[23] D.L.Jassby, *et. al.*, Rev. Sci. Instrum. **66**, (1995), to be published in January

[24] L.C.Johnson, *et. al.*, Rev. Sci. Instrum. **66**, (1995), to be published in January

[25] J.D.Strachan, *et. al.*, Rev. Sci. Instrum. **66**, (1995), to be published in January

[26] G.A.Wurden, *et. al.*, Rev. Sci. Instrum. **66**, (1995), to be published in January

[27] E.Ruskov, *et. al.*, Rev. Sci. Instrum. **66**, (1995), to be published in January

[28] A.L.Roquemore, *et. al.*, Rev. Sci. Instrum. **66**, (1995), to be published in January

[29] M.Osakabe, *et. al.*, Rev. Sci. Instrum. **66**, (1995), to be published in January

Chapter 4

Calculation of D-T Neutron Spectra from D-T Fusion Plasmas

4.1 Calculation Model

To evaluate the neutron energy spectra obtained by D-T discharges, a Monte Carlo code (NESFP: neutron energy spectra at fusion plasma experiments) was developed. The code calculates neutron energy spectra and fusion reactivity from plasmas of any deuterium and tritium ions velocity distributions at a certain line of sight geometry, so that it can use any result of Fokker-Planck solution. In the calculation discussed here, the spatial distribution of deuterium and tritium ions are assumed to be uniform. Almost any function, even if it is not given in an analytic form, can be used as velocity distributions of deuterium and tritium. The D-T fusion cross section was referred from reference [1] (Fig.4-1) and angular production probability of D-T neutron is assumed to be isotropic in the center-of-mass system.

The energy spectrum of the neutron $\phi(E_n)$ entering a detector and fusion reactivity $\langle \sigma_{dt} v_r \rangle$ can be expressed in the following formula:

$$\phi(E_n) = \int dv_t \int dv_d \, f_t(v_t) f_d(v_d) \sigma_{dt}(v_r) v_r P(\Omega; v_t, v_d)(d\Omega/dE_n)\Big|_{\Omega=k} \quad (4\text{-}1),$$

and $\langle \sigma_{dt} v_r \rangle = \int dv_t \int dv_d \, f_t(v_t) f_d(v_d) \sigma_{dt}(v_r) v_r \qquad (4\text{-}2),$

where $f_d(v_d)$: velocity distribution of deuterium ions,

$f_t(v_t)$: velocity distribution of tritium ions,

v_t, v_d : velocity of tritium and deuterium ions in laboratory system,

v_r : relative velocity of deuterium ion with respect to tritium ion ($=v_d-v_t$),
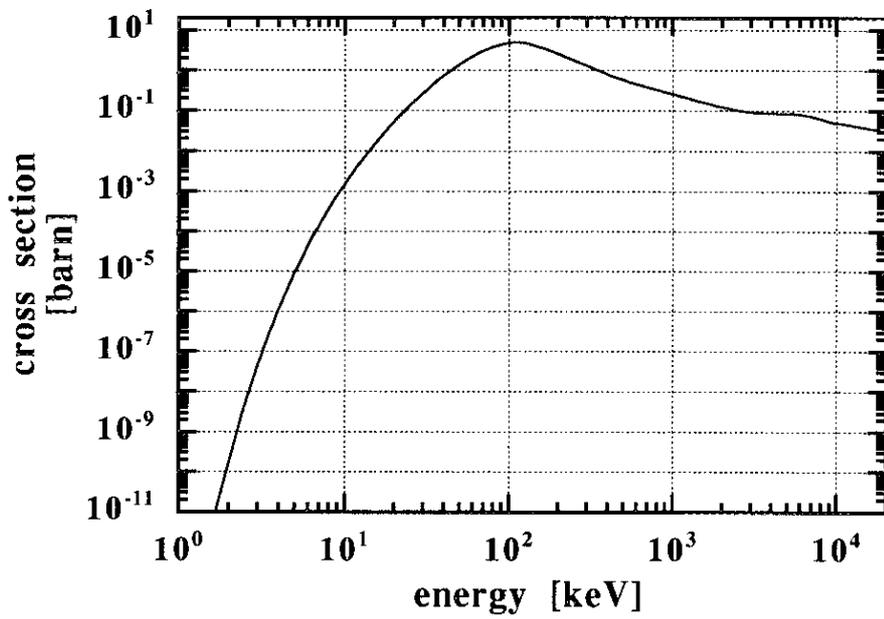
53

Fig. 4-1 D-T fusion cross section used in the NESFP
code[1].

v_n, Ω, E_n: velocity, direction and energy of
              fusion neutron in laboratory system
              (Appendix C),

σ_{dt}: cross section of D-T fusion reaction, and

k   : direction of the line-of-sight of the
             neutron detector in laboratory system.

The $P(\Omega; v_t, v_d)$ is the probability in which the neutron will be emitted in $d\Omega$ along Ω by the reaction between tritium ion of v_t and deuterium of v_d, and is expressed:

$$P(\Omega;v_t,v_d) = P(\Omega \cdot V) = (1/2\pi)P(\mu) \tag{4-3},$$

where **V** : velocity of center-of-mass system
                $(=(m_d v_d + m_t v_t)/(m_d + m_t))$,

        μ : cosine of the angle between **V** and Ω
                $(=V \cdot \Omega/\Omega)$, and

        $P(\mu)$: Angular production probability of
              neutron (Appendix C).

The flow chart of the code is shown in Fig.4-2. In the calculation, the velocities v_d and v_t were generated at random according to their distribution function. The direction **k** was fixed and given as an initial condition. The energy E_n, the fusion reactivity $\sigma_{dt}v_r$, and the angular production probability $P(\mu)$ were calculated for each pair of (v_d, v_t). The $\sigma_{dt}v_r$ was averaged over the whole history of the Monte Carlo calculation, and the neutron spectrum was constructed by accumulating the product $P(\mu)\sigma_{dt}v_r$ for a certain energy E_n.

4.2 Verification of the Code

To verify NESFP code, the neutron spectra and the fusion reactivity were calculated for Maxwellian distributed deuterium and tritium ions. A lot of calculational results are reported for the fusion

start

initialize

calculation of v_d deuteron velocity v_d: v_{dx}, v_{dy}, v_{dz}

calculation of v_t tritium velcity v_t: v_{tx}, v_{ty}, v_{tz}

calculation of κ, V, v_r

calculation of μ

calculation of $P(\Omega \cdot V)$, $\sigma(v_r)$

calculation of E_n

construction of neutron energy spectrum $NSPEC[i]=NSEPC[i]+P(\Omega \cdot V)*\sigma(v_r)v_r$

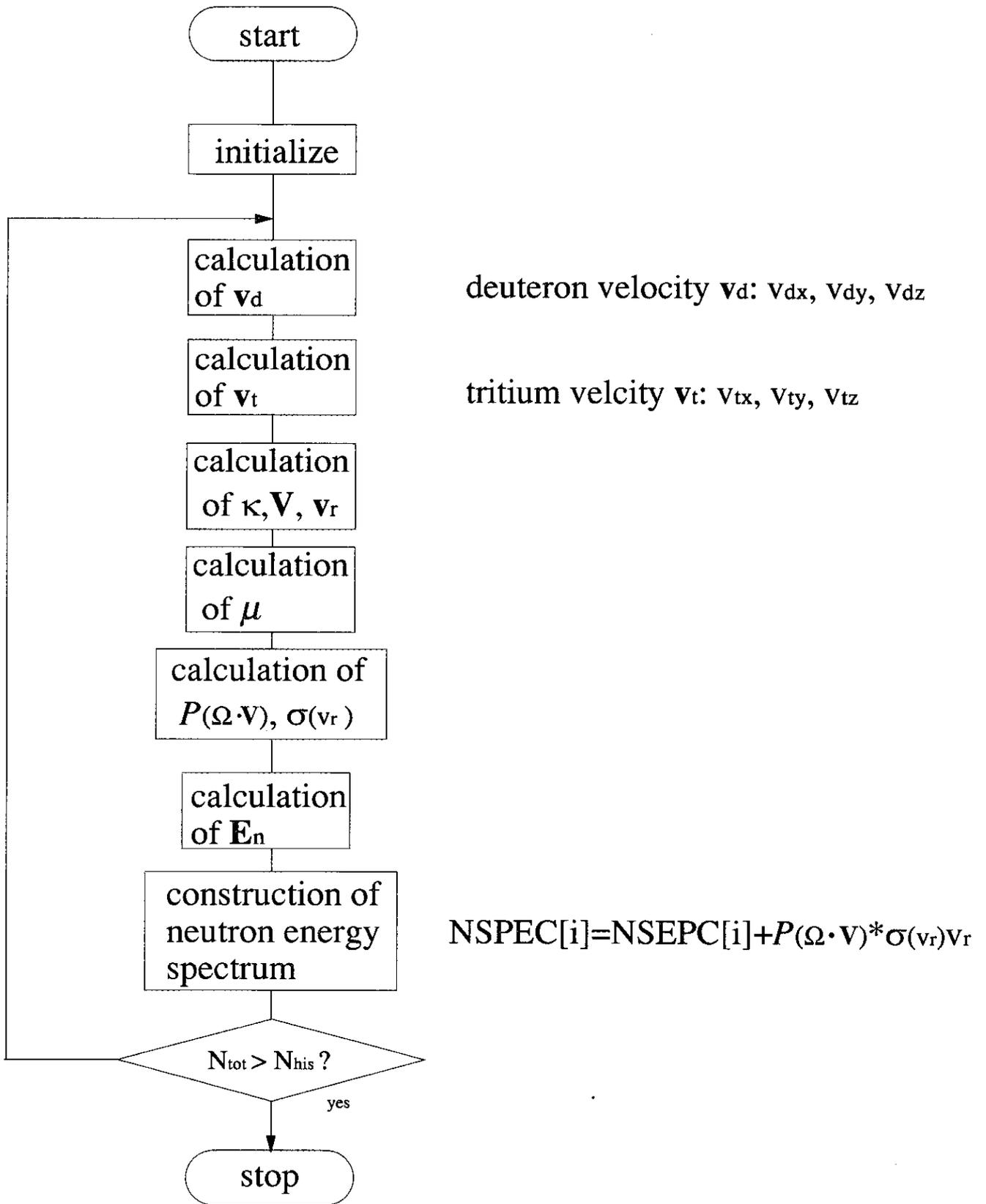$N_{tot} > N_{his}$?

yes

stop

Fig.4-2 Flow chart for NESFP code

reactivity and the neutron energy spectra of this case [1-4]. Here, the calculated fusion reactivity and neutron spectra by NESFP are compared with that in reference [1] and [2].

Figure 4-3(a) shows the calculated fusion reactivity. The open circles express the result of NESFP, and the solid line does the result shown in reference [1]. The neutron spectrum for a Maxwellian distributed D-T plasma is given in reference [2] by an analytical form of:

$$\phi(E_n) = \left(4\pi m_n T_i \langle E_n \rangle / (m_n + m_\alpha)\right)^{-1/2} \exp\left(-(E_n - \langle E_n \rangle)^2 \Big/ \frac{4m_n T_i \langle E_n \rangle}{m_n + m_\alpha}\right) \quad (4\text{-}4),$$

where $\langle E_n \rangle$ is an average neutron energy and T_i is an ion temperature in [keV]. The FWHM of the spectrum can be expressed as $\Delta E_n^{D\text{-}T} = 177\sqrt{T_i}$. In Fig.4-3(b), the FWHM of D-T neutron spectra obtained by NESFP is compared to that in reference [2]. Again, open circles express results of NESFP, and the solid line denotes that in reference [2]. As can be seen in these figures, these calculated values are in good agreement.

4.3 Other Example of the Calculational Results

The fusion reactivity and neutron energy spectra for deuterium and tritium ions of various velocity distributions were calculated. The result of calculation for two cases are shown here. One is the case in which the mono-energetic tritium ion beam is injected parallel to the magnetic field line (z-axis) into the thermal deuterium ions drifting parallel to the line, i.e., $f_t(v_t) = \delta(|v_t - v_{beam}|)$, and $f_d(v_d) = (m_d/2\pi T_d)^{3/2} \exp(-m_d(v_d - u_d)^2/2T_d)$. In the calculations, the deuterium temperature was set to 30keV and tritium beam energy was 100keV, because they were typical values of these parameters at TFTR. Another is the case in which the velocity distribution of deuterium ions is an isotropic Maxwellian of a temperature 30keV, and that of tritium ions is anisotropic Maxwellian, i.e., the tritium ion has different temperature in the direction
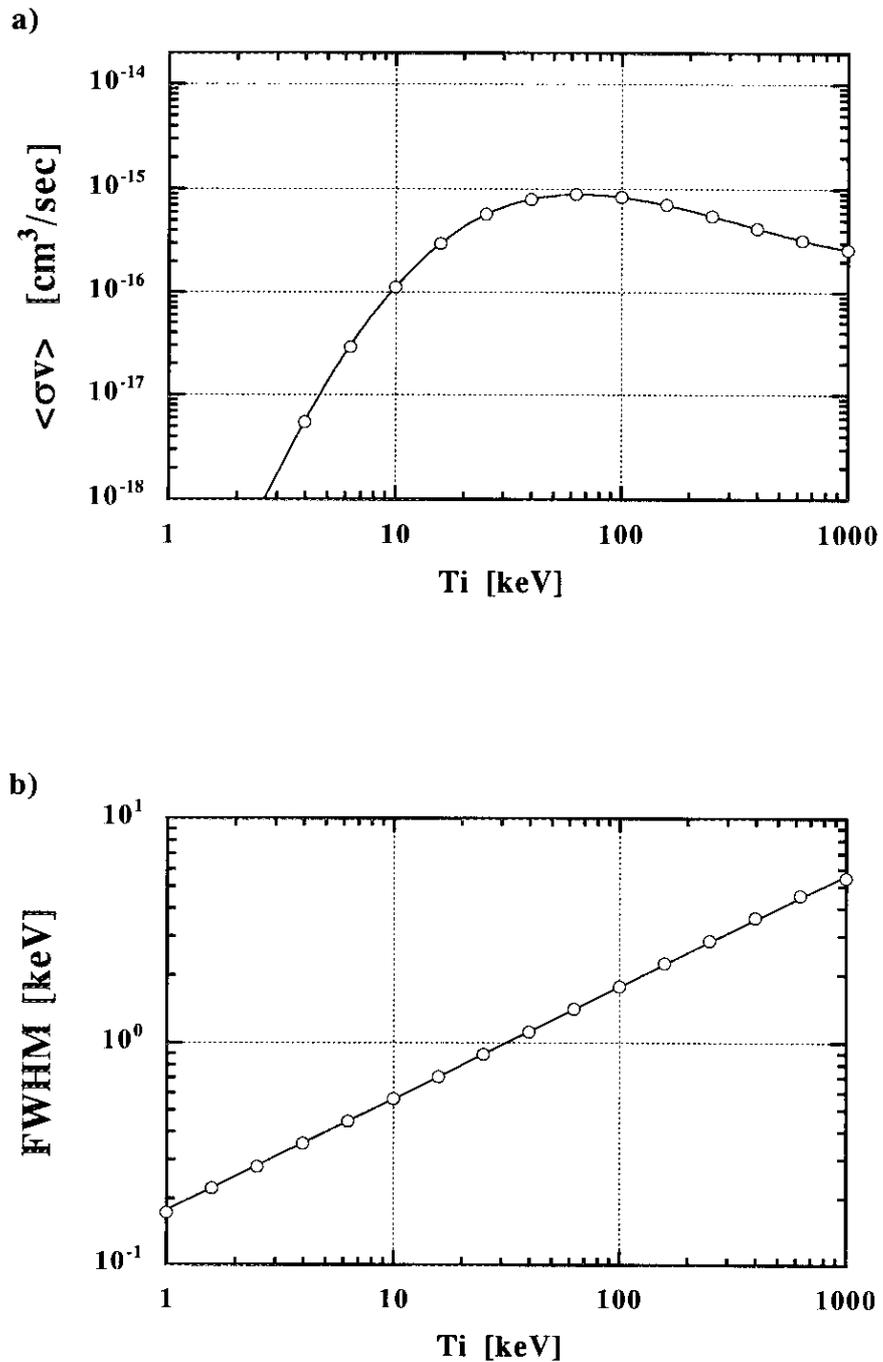
a)

b)

Fig.4-3 (a) Fusion reactivity, and (b) FWHM of the D-T
neutron peak are calculated for D-T Maxwellian plasmas.
The open circles show the result of NESFP, and the solid
line denotes that in references.

perpendicular to magnetic field lines and in the parallel direction. The parallel temperature was assumed to be 30keV, and the perpendicular temperature was varied in the calculation. In both cases, the line-of-sight of the neutron detector was set perpendicular to magnetic field lines.

a) Mono-energetic T ions and drifting thermal D ions

In Fig.4-4(a), the calculated fusion reactivity and the FWHM of the D-T neutron spectra are shown for the case of mono-energetic tritium ions and drifting thermal deuterium ions. This could be a zero-th order approximation for the case where tritium neutral beam was injected to the rotating deuterium plasma. The fusion reactivities are shown by the line with closed circles, and the FWHM are by that with open circles in the figure. The signs of x-axis express the direction of the deuterium drift velocity. The sign is set to minus(-) when the plasma is drifting in the counter direction to the tritium ion beam, and set to plus in co-direction. The fusion reactivity was maximized at $u/v_{th} \simeq -0.5$. This is due to the presence of giant resonance in the D-T fusion cross section at 100keV (Fig.4-1). When $u/v_{th} > -0.5$, the fusion reactivity decreases as the u/v_{th} increases. This could be the results of a decrease in relative velocity v_r between deuterium and tritium ions with the increase of u/v_{th}. On the other hand, the FWHM of D-T neutron spectra increases as the u/v_{th} increase. This is due to the isotropy of the relative velocity distribution. As u/v_{th} decreases, the relative velocity increases. Thus, the deuterium ions could be considered as a cold plasma. In this case, the relative velocity was determined only by the tritium velocity and deuterium drift velocity. Therefore, the neutron energy was fixed and the energy broadening of the spectrum could not happen. In Fig. 4-4(b), the energy spectra of D-T neutron are shown for $u/v_{th}=-0.5$(closed circles), 0(open circles), and 0.5(closed diamonds). The spectra were well fitted by Gaussian curve (Poison's R>0.999).
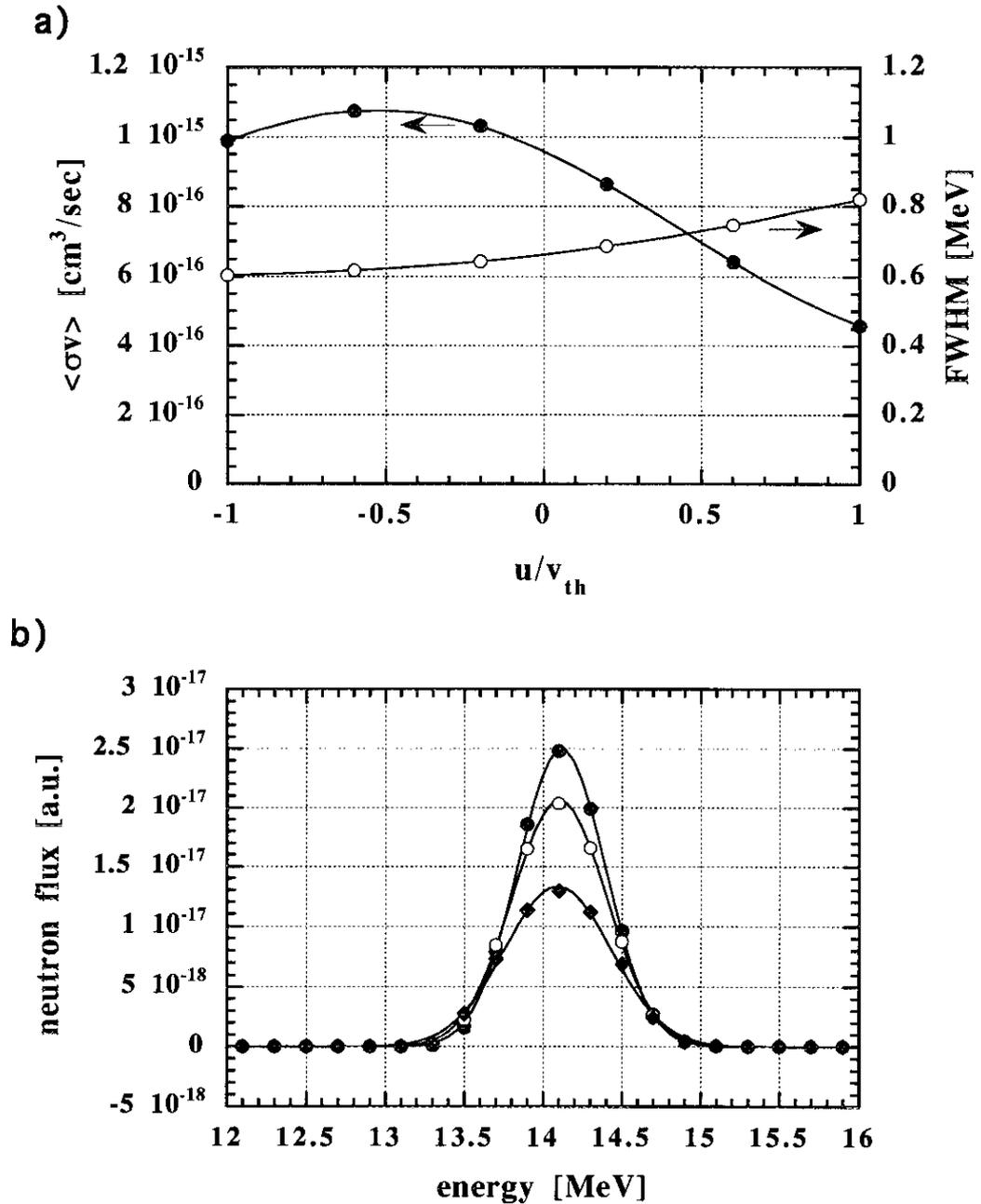
59

a)

b)

Fig.4-4 Result of the NESFP calculation for the case in which the mono-energetic tritium ions are injected parallel to magnetic field lines into the thermal deuterium ion plasma drifting parallel to the lines. The deuterium temperature were assuemed to be 30keV. The sign of x-axis shows the drift direction of deuterium ions with respect to the tritium beam direction. It was set to minus when deuterium ions are moving in the counter-direction to tritium ions, and to plus in the co-direction. (a) The line with closed circles shows the calculated $\langle \sigma_{dt} v_r \rangle$, and that with open circles does the FWHM of D-T neutron peak. (b) The example of the calculated D-T neutron spectra for u/v_{th}=-0.5(closed circles), 0(open circles), and 0.5(closed diamonds).

b) Thermal deuterium and anisotropic tritium ions

Fig.4-5(a) shows the calculated fusion reactivity and the FWHM of the D-T neutron spectra, when an isotropic Maxwellian distribution of temperature 30keV was assumed as a deuterium distribution function and an anisotropic Maxwellian distribution was as a tritium distribution, i.e.,

$$f_t(v_t) = \left(m_t/2\pi T_t^{para.}\right)^{1/2}\left(m_t/2\pi T_t^{parp.}\right)\exp\left(-(m_t/2)\{(v_{tx}^2 + v_{ty}^2)/T_t^{parp.} + v_{tz}^2/T_t^{para.}\}\right).$$

In the calculation, tritium parallel temperature was assumed to be 30keV and perpendicular temperature was varied. This model could calculate energy spectra of neutron produced by the reaction between thermal deuterium ions and ICRF heated tritium ions. In Fig.4-5(b), calculated D-T neutron spectra are shown where $T_t^{parp.}$=40keV(open circles), $T_t^{parp.}$=160keV(closed circles), and $T_t^{parp.}$=400keV(closed diamonds). The solid lines are Gaussian fitted curve of these spectra. They were well expressed by Gaussian curves, and Poison's R's of the fitting were greater than 0.998.

As shown in Fig.4-5(a), the fusion reactivity has its maximum at $T_t^{parp.}\simeq$160keV, this again was due to the giant resonance in D-T reaction cross section. On the other hand, the FWHM of D-T neutron spectra monotonously increases with an increase of $T_t^{parp.}$. This feature suggests that the necessity of neutron spectrum measurement for ICRF heated D-T plasma experiments. Due to the presence of the giant resonance in D-T fusion cross section, we might misread the efficiency of ICRF heating when only neutron counting measurements are performed at D-T ICRF heating experiments. It is recommended that the efficiency of ICRF heatings should be monitored both by a neutron counting measurement and a energy measurement, and that both results are cross-checked to each other.
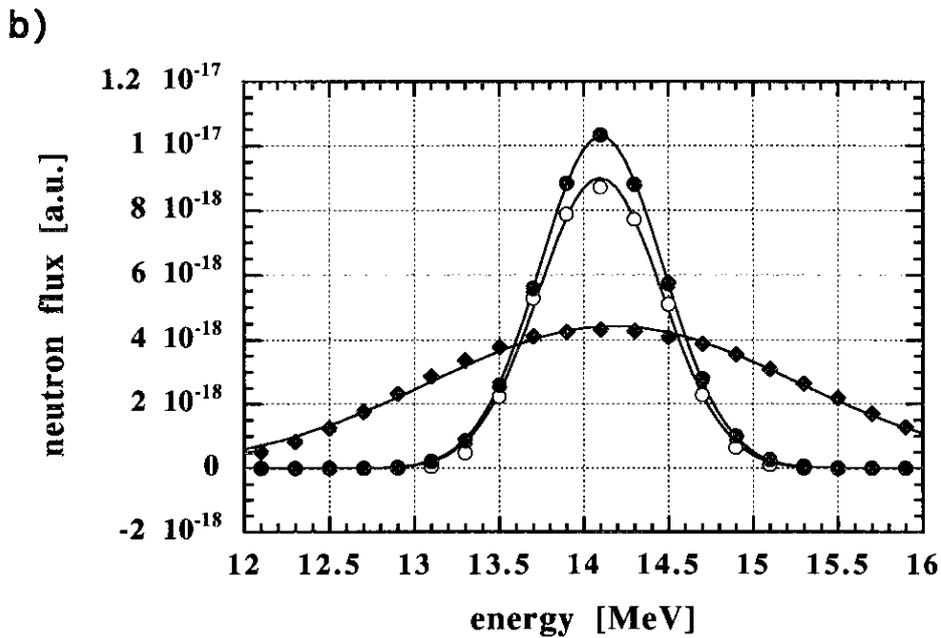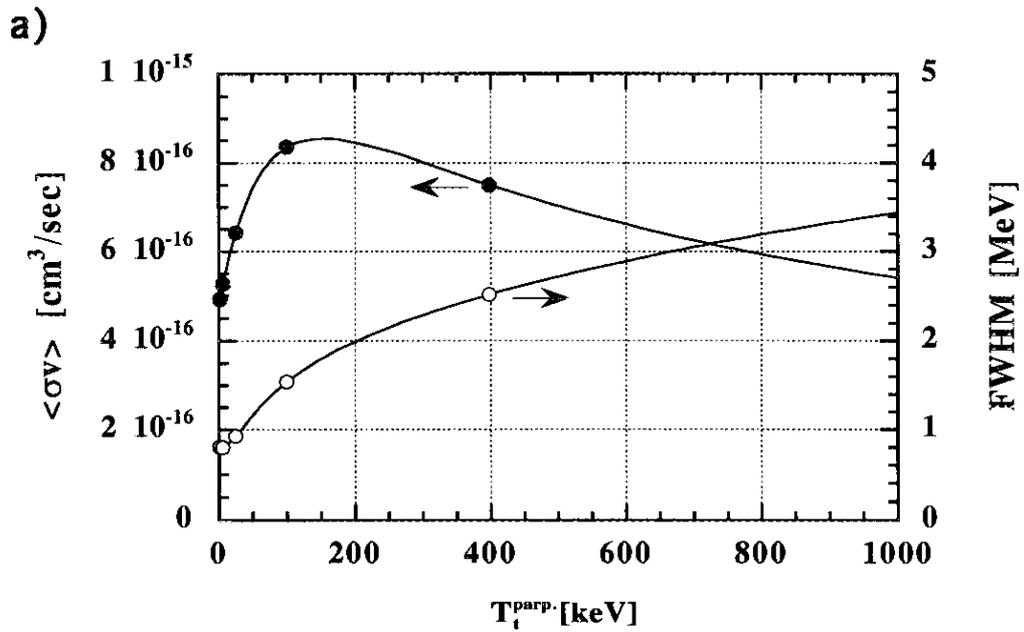
a)

b)

Fig.4-5 Result of the NESFP calculation for the case in which the velocity distribution of deuterium ions is an isotropic Maxwellian of a temperature 30keV, and that of tritium ions is anisotorpic Maxwellian, i.e., the tritium ion was assumed to have different temperture in the direction parpendicular to magnetic field line and in the parallel direction. The parallel temperature was assumed to be 30keV, and the parpendicular temerature was varied in the calculation. (a) The line with closed circles shows calculated $\langle \sigma_d v_r \rangle$, and that with open circles does the FWHM of D-T neutron peak. (b) The example of the calculated D-T neutron spectra for $T_t^{parp.}$=40keV(open circles), 160keV(closed circles), and 400keV(closed diamonds).

62

References

[1] R. Feldbacher, INDC(AUS)-12/G Vers.1 (1987)

[2] H.Brysk, Plasma Phys.**15**, 611 (1973)

[3] J.Scheffel, Nul. Instr. and Meth. **224**, 519 (1984)

[4] H.Liskien, Nucl. Sci. Eng. **71**, 57 (1979)

[5] W.W.Heidbrink, Rev.Sci. Instrum. **56**, 1098 (1985)

Chapter 5

Energy measurement of D-T neutron from ICRF heated D-T plasmas

5.1 Outline of the Experiment

The ion cyclotron range of frequency (ICRF) heating was applied to D-T plasmas on TFTR. The purpose of the experiments is to study the RF physics of ICRF-heated D-T plasmas and to enhance the performance of D-T discharges. The ICRF heating is considered as one of the primary techniques for ITER[1-3]. But, no experimental database has been available to provide the benchmark for the RF simulation code for D-T plasmas. The ICRF heated D-T experiments on TFTR are expected to provide valuable results in extrapolating T-heatings on ITER.

Two RF frequencies, 43MHz and 64MHz, can be used on TFTR[2,3]. In the experiments discussed here, RF power of 43MHz frequency was launched with four antennas at the mid plane on the low field side of the plasma. The experiments are focused on (1) the increase in the central electron temperature of a D-T supershot plasma by coupling ICRH and, consequently, enhance the core α-particle slowing down time, (2) the investigation of the effect of the increased α-particle slowing down time on the central α pressure, (3) the study of RF-physics of the second harmonic tritium resonance with and without the presence of ^{3}He minority in D-T supershot plasmas[2].

5.2 Result of Experiment and Comparison with Calculation

a) D-T neutron spectra obtained for a NBI-discharge

In Fig.5-1, the energy spectrum of D-T neutron for a NBI discharge is shown. Applying a gaussian fitting to the spectrum (solid
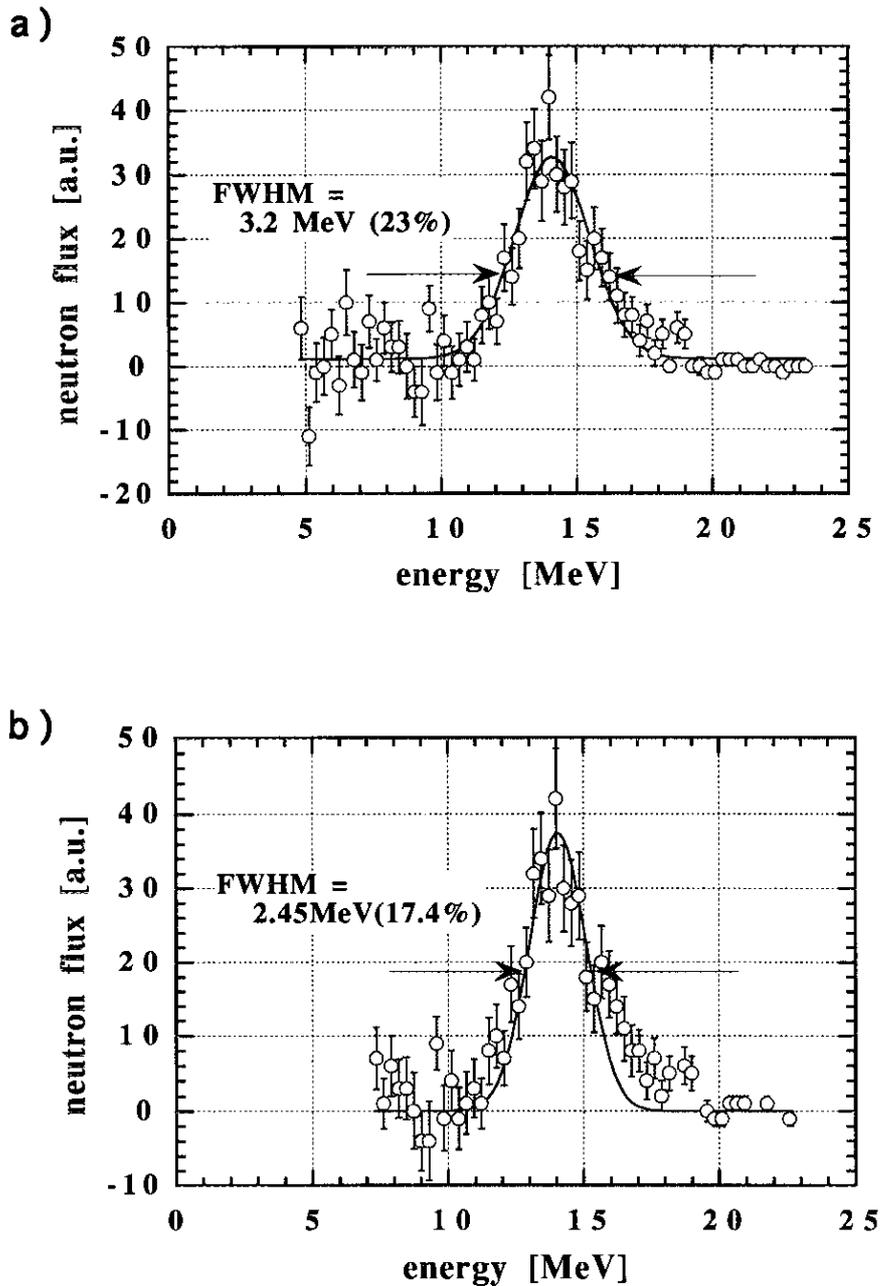
Fig.5-1 Energy spectrum obtained for a NBI heated D-T plasma. (a) open circles show the obtained spectra during the discharge, and the solid line shows the gaussian fitted curve of them. (b) open circles are the same spectrum as shown in (a), but the data point whose error is equal to zero were eliminated. Solid line is obtained by a fitting of gaussian curve whose FWHM are fixed to 17.4%.

line in Fig.5-1(a)), the FWHM of the peak was estimated to be 3.2MeV(23±2%). The ion temperature was measured by charge exchange recombination spectroscopy measurement, and the central ion temperature was 26keV at t=3.4 sec.

Using the NESFP code, the energy spectra of D-T neutron in three cases were calculated (Fig.5-2(a),(b),and(c)). The peak positions of the spectra did not change appreciably and were about 14.1MeV. In the first case the spectra of neutron resulted from the reaction between thermal component of deuterium and tritium were calculated(Fig.5-2(a)). In this case, Maxwellian velocity distribution function of temperature 26keV was assumed for each ion species of deuterium and tritium. The full width at half maximum (FWHM) of the peak was 0.92MeV(6.2%). The second case was for the reaction between thermal component of deuterium and beam component of tritium (Fig.5-2(b)). The same distribution function was applied for deuterium ions as was used in the first case. The angle averaged solution of Fokker-Planck equation for beam ions was used in this case as a velocity distribution function for tritium ions [3], i.e.,

$$f(v) \quad \propto \quad 1/(v^3 + v_c^3), \qquad (v_{th} < v < v_{beam}) \quad (5\text{-}1)$$

where v_c: critical velocity defined as,

$$\frac{1}{2}mv_c^2 = W_{crit} = 14.8T_e\left[\left(A^{3/2}/n_e\right)\sum_i n_i Z_i^2/A_i\right],$$

T_e: electron temperature, A, A_i: atomic weights of injected ions and the plasma ions, n_e, n_i: number density of electrons and ions, and Z_i: charge numbers of the ions

v_{th}: thermal velocity of ions

$(\frac{1}{2}mv_{th}^2 = T_i$, T_i: temperature of ions in keV), and

v_{beam}: initial velocity of injected beam ions
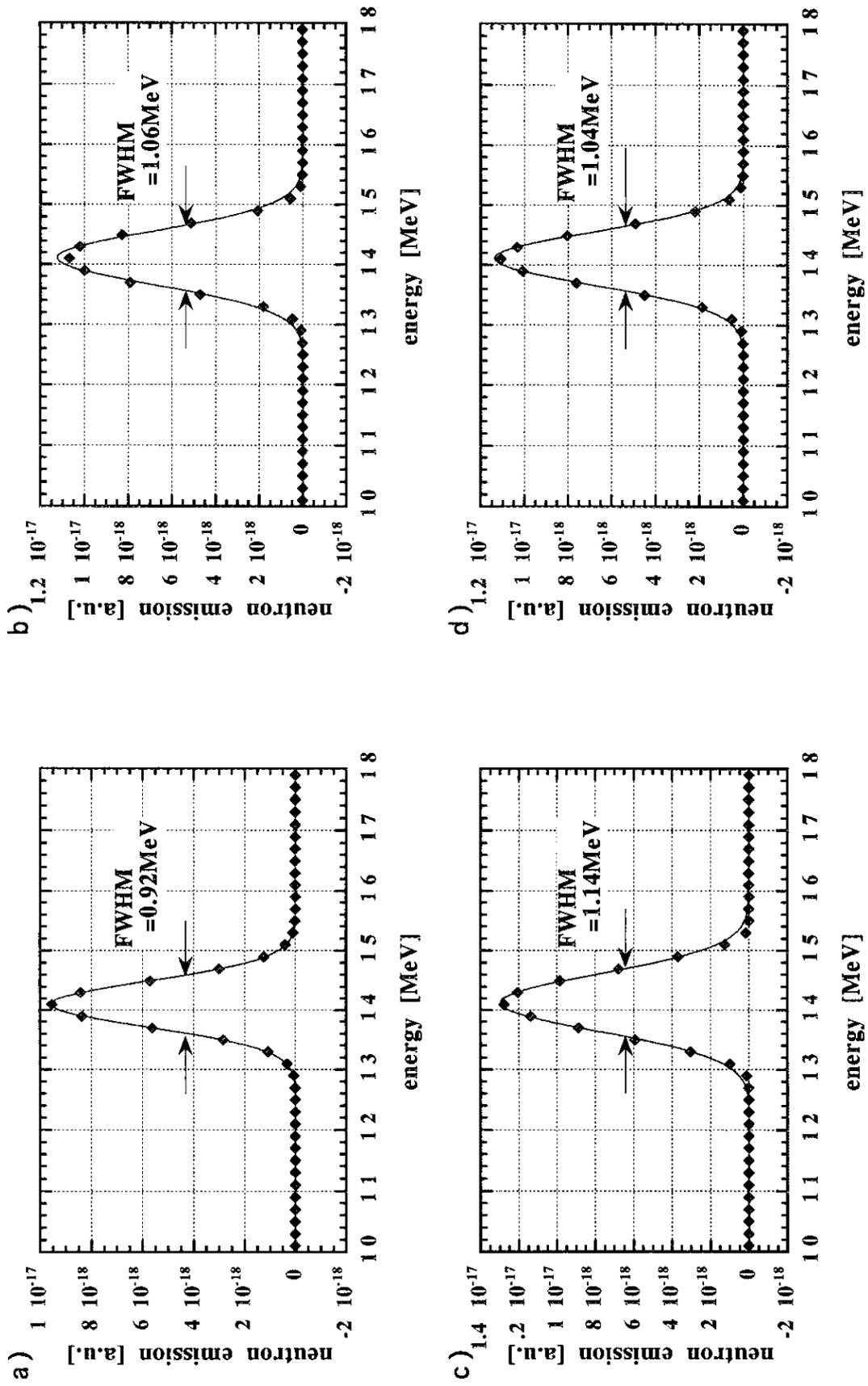
$(\frac{1}{2}mv_{beam}^2 = E_{beam})$.

Fig.5-2 Calculated D-T neutron spectra by NESFP code. (a)spectra resulted from the reaction between thermal component of deuterium and tritium (thermal component), (b)that between thermal deuterium component and beam tritium component (beam-thermal component). (c)that between beam component of deuterium and tritium (beam-beam component), (d) composite spectra of (a),(b) and (c). The spectra was summed assuming the 50% of D-T neutrons are beam-thermal component, 25% are thermal component, and 25% are beam-beam component

67

In the third case, the both tritium ions and deuterium ions were assumed to be beam components. The eq.(5-1) was used as a velocity distribution function for each of tritium and deuterium ions. The FWHM of the peak are 1.06MeV(7.5%) for beam-thermal component, and 1.14MeV(8.1%) for beam-beam component. In Fig.5-2(d), the composite spectrum of these three spectra is shown. The half of the D-T neutron being emitted was assumed to be beam-thermal component, and halves of the rest to be thermal and beam-beam components. The FWHM of this spectrum is 1.04MeV(7.4%). Taking into account the energy resolution (9.5%) of set-B obtained by calibration experiments and the energy broadening of the peak due to the ground level fluctuation (12.6%) which is monitored by the time scale markers, the FWHM of the expected spectrum becomes 17.4% which is narrower than that obtained for the NBI-discharge.

Assuming the FWHM of the spectrum for the discharge as 17.4%, a Gaussian fitting was applied with the FWHM of the peak being fixed to 17.4% (Fig.5-1(b)). The χ^2 of the fitting was 90 and the degree of freedom (v) was 47. For the significance level of 5%, the region of rejection is $\chi^2 > 64$ for the χ^2-distribution of $v=47$. Therefore, this fitting is apparently wrong. The energy resolution of set-B measurement system seems to be deteriorated to $22\pm2\%$ ($= \sqrt{23^2 - 7.4^2}$) due to various influences, i.e., the multiple pulses in single gate width, the fluctuation of ground level of the detector signals whose characteristic time is shorter than the period of time scale marker, the degradation of multiplication of PMT's due to high counting rate measurements, and etc. Among them, the effect of the multiple pulses is most probable as the spectrum over 15MeV is significantly distorted in Fig.5-1(b), which could be the result of the influence.

68

b) D-T neutron spectra obtained for RF-discharges

In Fig.5-3, the energy spectra of neutron for the plasmas being heated by NBI and ICRF are shown. Figure 5-3(a) and (b) were for plasmas with ^{3}He minority. They were almost identical plasmas, but, in (a), some of NBI sources were failed at the end of the discharge. Figure 5-3(c) was for a plasma without ^{3}He minority. The FWHM of these peaks are (a) 4.0 ± 0.3MeV ($28\pm2\%$), (b) 3.7 ± 0.2MeV ($26\pm1\%$), and (c) 3.5 ± 0.3MeV ($25\pm2\%$). These are summarized in Table.5-1. There is a trend that RF-discharges have greater width than a NBI-discharge, although the accuracy of the measurement is not good. Subtracting the energy resolution of the whole detection system of set B ($22\pm2\%$) which is estimated in the previous section, the width of the spectra becomes (a) $17\pm4\%$, (b)$14\pm4\%$, and (c)$12\pm6\%$. Assuming the origin of the neutrons are the reaction between thermal component (isotropic Maxwellian) of tritium ions and deuterium ions, the ion temperature can be evaluated from the energy width. The estimated ion temperatures are shown in Table 5-2. By Charge Exchange Recombination Spectroscopy measurements, Ion temperature of ICRF heated D-T plasmas was evaluated as 36keV at t=3.4s, which is much smaller than temperatures obtained for the case of isotropic Maxwellian. As the second harmonic resonance regions for tritium ions were located in the center of plasmas during these RF-discharges[5], the velocity distribution of tritium ions could be different in the direction parallel to magnetic field lines and in the perpendicular direction. In Fig.5-4, the calculated FWHM are shown for the case where deuterium ion has a velocity distribution of an isotropic Maxwellian and tritium ion has that of an anisotropic Maxwellian. In the calculation, the deuterium ion temperature and parallel component of tritium ion temperature were set to 36keV, and the perpendicular component of the tritium ion temperature was varied.
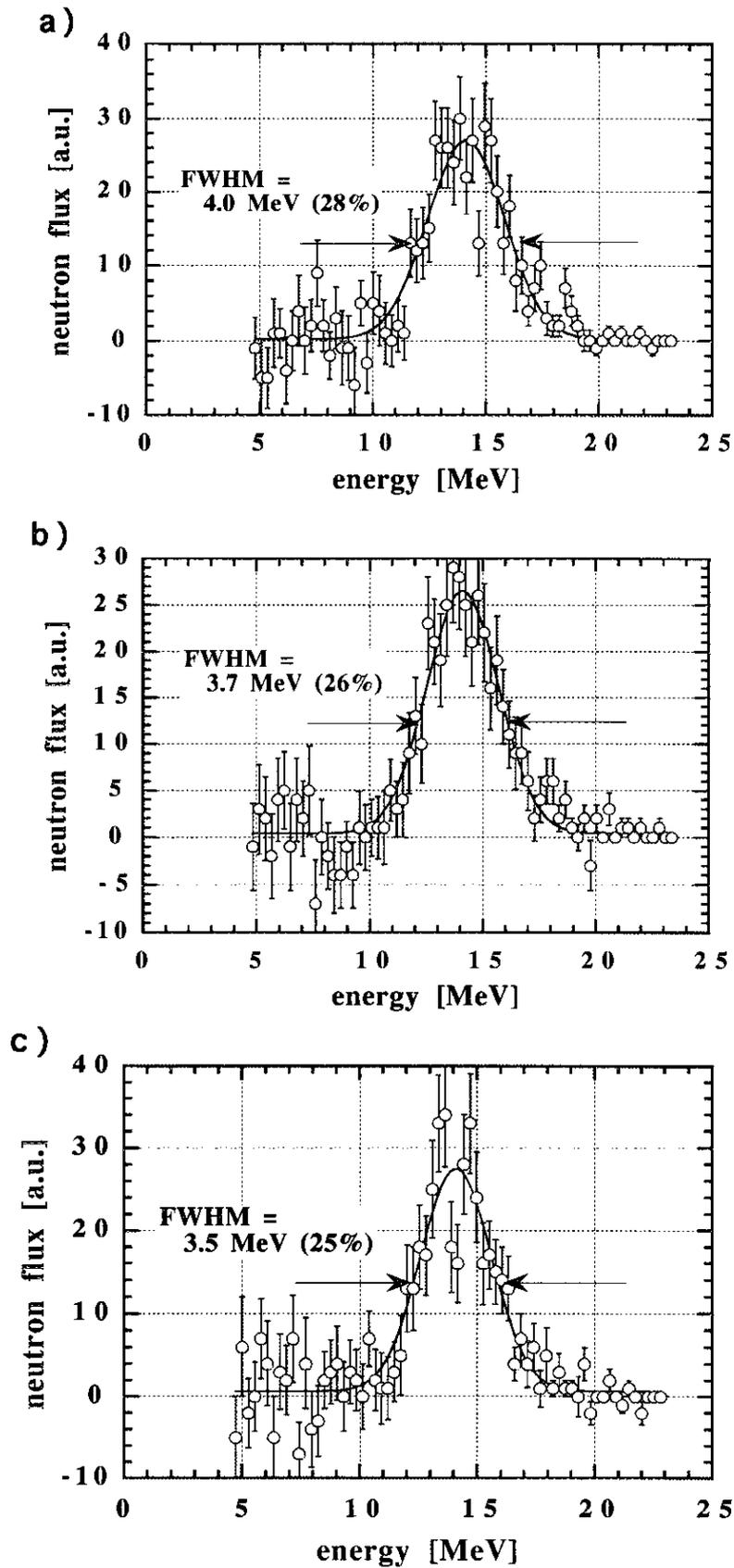
69

Fig.5-3 Energy spectra of neutron obtained for NBI and ICRF heated plasma. (a) and (b) are that obatined for discharges with ^{3}He minority. (c) is that obtained for a discharge without ^{3}He
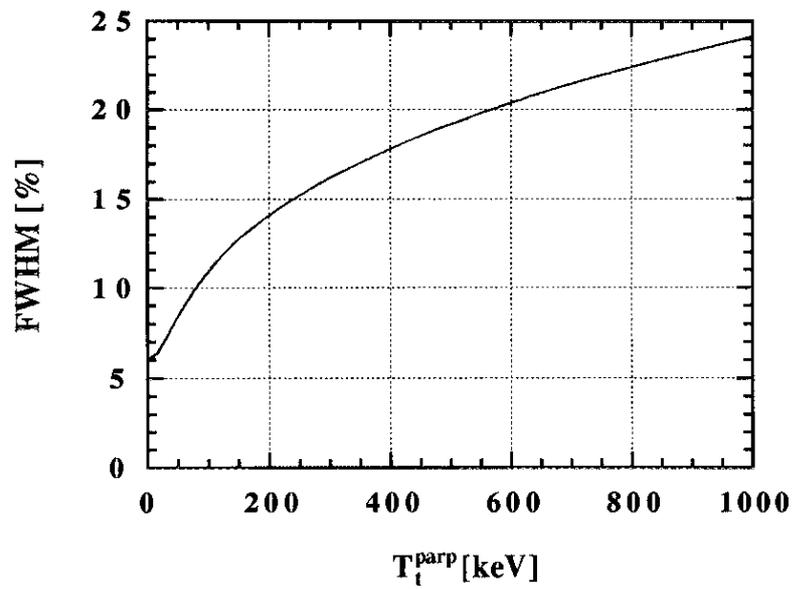
70

Fig. 5-4 The calculated FWHM of D-T neutron peak. The deuterium velocity distribution function was assumed as an isotropic Maxwellian of temperature 36keV, and the tritium distribution function was as an anisotropic Maxwellian having different temperature in the direction parallel to magnetic field lines and in the perpendicular direction. Tritium parallel temperature was assumed to be 36keV, and the perpendicular temperature was varied in the calculation

71

Using this calculation result, the perpendicular temperatures were evaluated to be (a) 350^{+310}_{-190}keV, (b) 200^{+210}_{-120}keV, and (c) 125^{+285}_{-125}keV. Because of the weak dependence of the FWHM on the perpendicular temperature, errors in FWHM were projected to large errors in the perpendicular temperature. It is necessary to measure the FWHM of D-T neutron peak with small uncertainty to investigate the effect of ICRF heatings.

Table 5-1   The energy width of the obtained spectra for a NBI-discharge and for RF-discharges.

Type of discharge	Original FWHM [%]	Estimated FWHM [%]
NBI-discharge	23 ± 2	7.4
RF-discharge (a)	28 ± 2	17 ± 4
RF-discharge (b)	26 ± 1	14 ± 4
RF-discharge (c)	25 ± 2	12 ± 6

Table 5-2   The estimated ion temperatures for RF-discharges.   In the case of isotropic Maxwellian, ion temperatures were estimated by assuming that D and T ions' distributions were isotropic Maxwellians and that both ions had same temperatures.   In the case of anisotropic Maxwellian, the velocity distribution of deuterium was an isotropic Maxwellian of temperature 36keV and that of tritium was an anisotropic Maxwellian having different temperatures in the direction parallel to magnetic field lines and in the perpendicular direction.   Tritium parallel temperature was assumed to be 36keV, and the perpendicular temperatures were evaluated.

Type of discharge	Ion Temperature [keV] (isotropic Maxwellian)	Perpendicular Tritium Temperature [keV] (anisotropy Maxwellian)
RF-discharge (a)	190^{+90}_{-80}	350^{+310}_{-190}
RF-discharge (b)	130^{+100}_{-80}	200^{+210}_{-120}
RF-discharge (c)	95^{+115}_{-70}	125^{+285}_{-125}

References

[1] R.J.Hawryluk, *et al.,* Physics of Plasmas **1**,1560 (1994)

[2] G.Taylor, *et. al.,* IAEA-CN-60/A-3-I-3, 15th International Conference on Plasma Physics and Controlled Nuclear Fusion Research, Seville, Spain, (1994)

[3] R.Majeski, *et. al.,* IAEA-CN-60/A-3-I-4, 15th International Conference on Plasma Physics and Controlled Nuclear Fusion Research, Seville, Spain, (1994)

[4] D.L.Jassby, Nuclear Fusion **17**, 309 (1977)

Chapter 6

Conclusion

Based on the proton recoil counter telescope technique, a new type of neutron energy spectrometer, named COTETRA(counter telescope with thick radiator), was developed and applied to the magnetically confined D-T plasma experiments on TFTR (Tokamak Fusion Test Reactor). The first D-T neutron energy spectra were obtained during the experiments.

The prototype of COTETRA was constructed and its performance was tested using an intense D-T neutron generator. The results of the experiments were compared to those of Monte Carlo calculation code, which simulates its detection process. The results of the calculation agree with those of the calibration experiments within its margin of error.

Two types of COTETRA (set-A and -B) were developed for the application to TFTR D-T experiments. Set-A was characterized by higher energy resolution, while set-B was by higher counting rate capability and detection efficiency. Energy resolution of 4% was obtained for 14.8-MeV neutron with set-A. It was confirmed that set-B could work at a count rate of up to 10^4cps, which corresponds to a neutron flux rate of $\sim10^9$ (n/cm^2)/s. The detection efficiency of set-B was $\sim6\times10^{-5}$ counts/(n/cm^2).

Both of them were installed at the multichannel neutron collimator of TFTR. The data acquisition system was newly developed at TFTR. The neutron energy spectra were successfully obtained for a NBI heated discharge and 'NBI and ICRF' heated discharges. The full width at half maximum (FWHM) of the peak for the 'NBI and ICRF' heated discharges are wider than that for a NBI heated discharge.

The Monte Carlo code NESFP was developed to calculate the energy spectra of neutrons emerged from D-T fusion plasmas. The calculated energy spectra suggested that the broadening of neutron spectra for 'NBI and ICRF' heated discharges was due to the existence of the high energy tritium ion tail of 100~400keV. It was also suggested by the calculation that the measurement of neutron energy spectrum is necessary in evaluating the existence of high energy ions besides the total neutron yield, which might decrease at higher ion temperature for D-T plasmas.

Space resolved measurements of D-T neutron energy spectra will be necessary for the D-T ICRF heated plasma experiments on the next large tokamak, such as ITER, to evaluate the mechanism of ICRF heating in the plasma. The COTETRA will be a suitable diagnostic for this purpose because of its good energy resolution and compactness.

Appendix A

Effect of Lucite lens on the energy resolution of ΔE-detector

In designing the ΔE-detector of the prototype, the light collection efficiency of the light guide was one of the great interests. There are two ways of maximizing the efficiency. One is increase in the extracting probability of scintillation light from the scintillator (P^{ext}). The other is decrease in the attenuation loss of the light in the light guide. It can be easily thought that the shape of the scintillator surface could affect P^{ext}. Attaching a Lucite lens on the scintillator was planed to increase the P^{ext}. Lucite was chosen because it has similar refractive index to the plastic scintillator (NE102A) for the scintillation light.

Figure A-1 shows the calculated P^{ext}. The cylindrical scintillator of thickness 2mm and of radius 21mm was assumed in the calculation. The solid line shows the change of P^{ext} with the change of the curvature radius of Lucite lens (R^{cuv}). The dashed line express the P^{ext} without a Lucite lens. As was expected, the P^{ext} with lens is greater than that without lens for any R^{cuv}. Taking the distortion of the neutron spectrum by the Lucite lens into accounts, R^{cuv} was set to 35mm. It was expected that the ΔE-detector with a Lucite lens would have a slightly better energy resolution than that without a lens, since P^{ext}_{lens} was estimated to be greater than $P^{ext}_{no-lens}$.

To assure the tendency shown by the calculation, two types of ΔE-detectors are constructed (LG1 and LG2), which is shown in Fig.A-2, and the energy resolutions of them are measured using the internal conversion electron (ICE) from ^{137}Cs (Table 1). On the contrary to the calculation, the energy resolution of LG2 was worse than that of LG1. This was considered due to the difference in the attenuation loss of
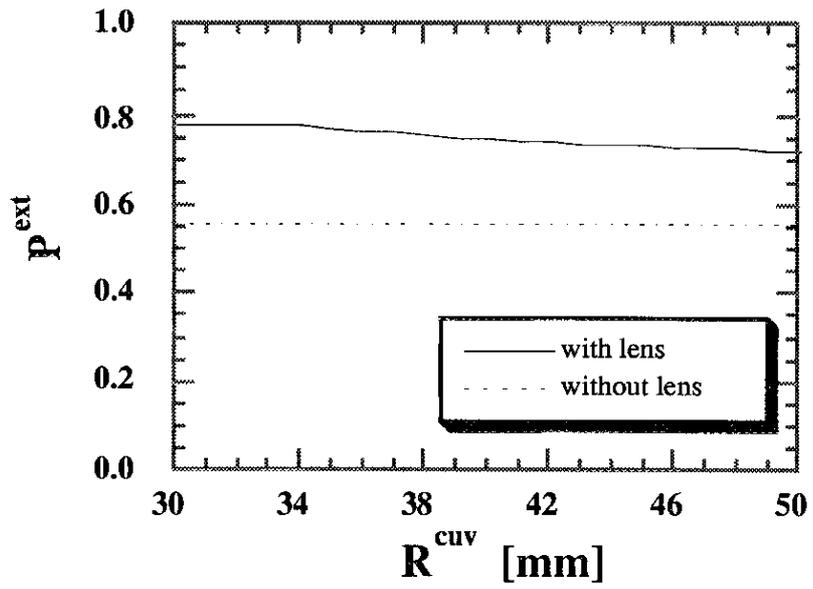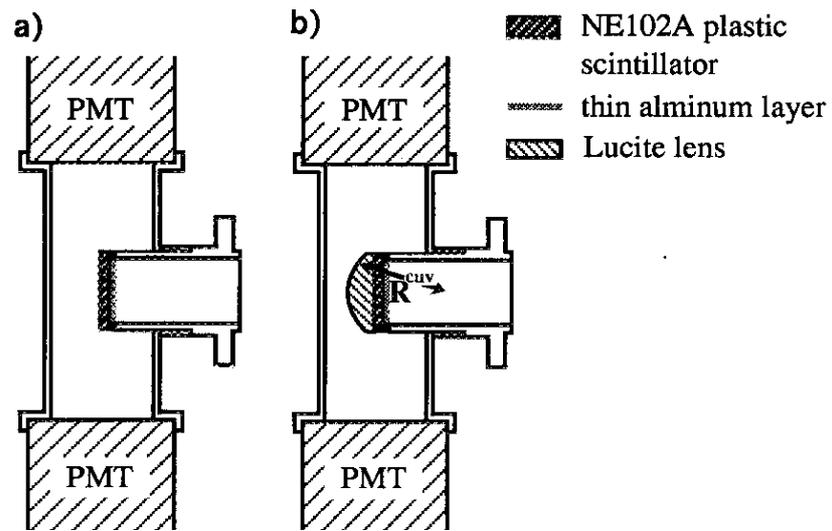
76

Fig. A-1 Calculated P^{ext} vs R^{cuv}

Fig. A-2 ΔE-detector with inner polished aluminum
light guide (a)without a Lucite lens and (b)with a
Lucite lens.

scintillation lights in the light guide, which was not considered in the calculation.

Table 1   Measured energy resolution of ΔE-detector for 1.01 MeV electron (ICE from ^{137}Cs)

Type of light guide	Energy Resolution
Inner Polished Al Light Guide without lens (LG1)	24%
Inner Polished Al Light Guide with lens (LG2)	30%

Although it was suggested by the calculation that the light extracting efficiency would increase by attaching a Lucite lens on a plastic scintillator, an improvement on the energy resolution could not be observed experimentally on COTETRA ΔE-detectors. As Lucite contains a lot of hydrogen atoms, neutrons may recoil protons in the lens. Those proton will increase the count rate of ΔE-detector and decrease the 'true events to accidental coincidence events' ratio of COTETRA, which would cause a severe problem at the high neutron flux environment. Therefore, lens were not applied for the COTETRA set-A and -B.

Appendix B

Energy dependence of the resolution of
ΔE-detector

The pulse height resolution of scintillation detector is expressed in the empirical approximation[1],

$$\Delta L/L = [\alpha^2 + (\beta/L^{1/2})^2 + (\gamma/L)^2]^{1/2}$$

where the parameters consider the geometrical influences (α), the statistical fluctuation of the light production and amplification (β) and the noise of the photomultiplier and electrical circuits (γ).

In the present case, the noise component (γ) is extremely reduced owing to the coincidence technique between two photomultiplier, and it could be neglected in the energy range higher than 1 MeV, as being experimentally tested by using various γ-ray sources.

The geometrical influence on ΔL mainly comes from the difference of the average length of light path (Δx) from a scintillation point to the photomultiplier tube. The influence of a small difference Δx on L can be expressed in the form of $\Delta L \cong (\partial L / \partial x)\Delta x$. Since the geometrical influence on ΔL can be considered to be proportional to L, this equation becomes $\Delta L \cong \alpha' L \Delta x$. Then, L will be written in the form $L \cong A \exp(\alpha' x)$.

Here, we consider the geometrical influence on ΔL in the case where a scintillator is placed at the center of two photomultipliers (PMT_{left} and PMT_{right}) which are faced each other and the signal (L) is the sum of the output of these two PMT's (L_{left} and L_{right}), i.e., $L \cong L_{left} + L_{right}$. When the scintillation point is deviated by x [cm] to the photo cathode of PMT_{left} from the center of the scintillator d [cm], L_{left} and L_{right} can be expressed by $L_{left} = L_0 \exp(\alpha'(d-x))$ and $L_{right} = L_0 \exp(\alpha'(d+x))$. Then, the signal of the detector is;

$$L = L_0 [\exp\{\alpha'(d+x)\} + \exp\{\alpha'(d-x)\}],$$

80

and the energy broadening due to the geometrical influence becomes;

$$\Delta L/L = \{(\partial L/\partial x)\Delta x\}/L = \{(L_{right} - L_{left})/(L_{right} + L_{left})\}\alpha'\Delta x.$$

With L_{left} and L_{right}, $\alpha'x$ is expressed in the form of $\alpha'x = \{\ln(L_{right}/L_{left})\}/2$ and $\alpha'\Delta x$ can be calculated as a standard deviation of $\alpha'x$. Then, the geometrical factor of $\Delta L/L$ is determined from the distribution of (L_{left}, L_{right}).

Figure B-1 shows the distribution function of $\{\ln(L_{right}/L_{left})\}/2$ ($=\alpha'x$). Applying a gaussian fitting to the raw data of Fig. B-2, $\alpha'\Delta x$ is calculated and is 8.51×10^{-2}. Using this $\alpha'\Delta x$ and the data of Fig. B-1, the $\Delta L/L$ distribution is obtained and is shown in Fig. B-2. The FWHM of this distribution is 1.45×10^{-2}.

Figure B-3 shows the energy broadening (ΔE) of Detector #1 of the prototype due to the geometrical influence and the statistical fluctuation. The geometrical influence (ΔE_{geo}) and the statistical fluctuation (ΔE_{stat}) are considered to be $\Delta E_{geo} = (1.45\times10^{-2})E$ a n d $\Delta E_{stat} = (3.98\times10^{-1})\sqrt{E}$, respectively. The total energy broadening (ΔE_{tot}) is estimated from $\Delta E_{tot} = (\Delta E_{geo}^2 + \Delta E_{stat}^2)^{1/2}$. When the energy of the proton is less than 20 MeV, ΔE_{stat} is dominant and ΔE_{geo} is almost negligible.

References
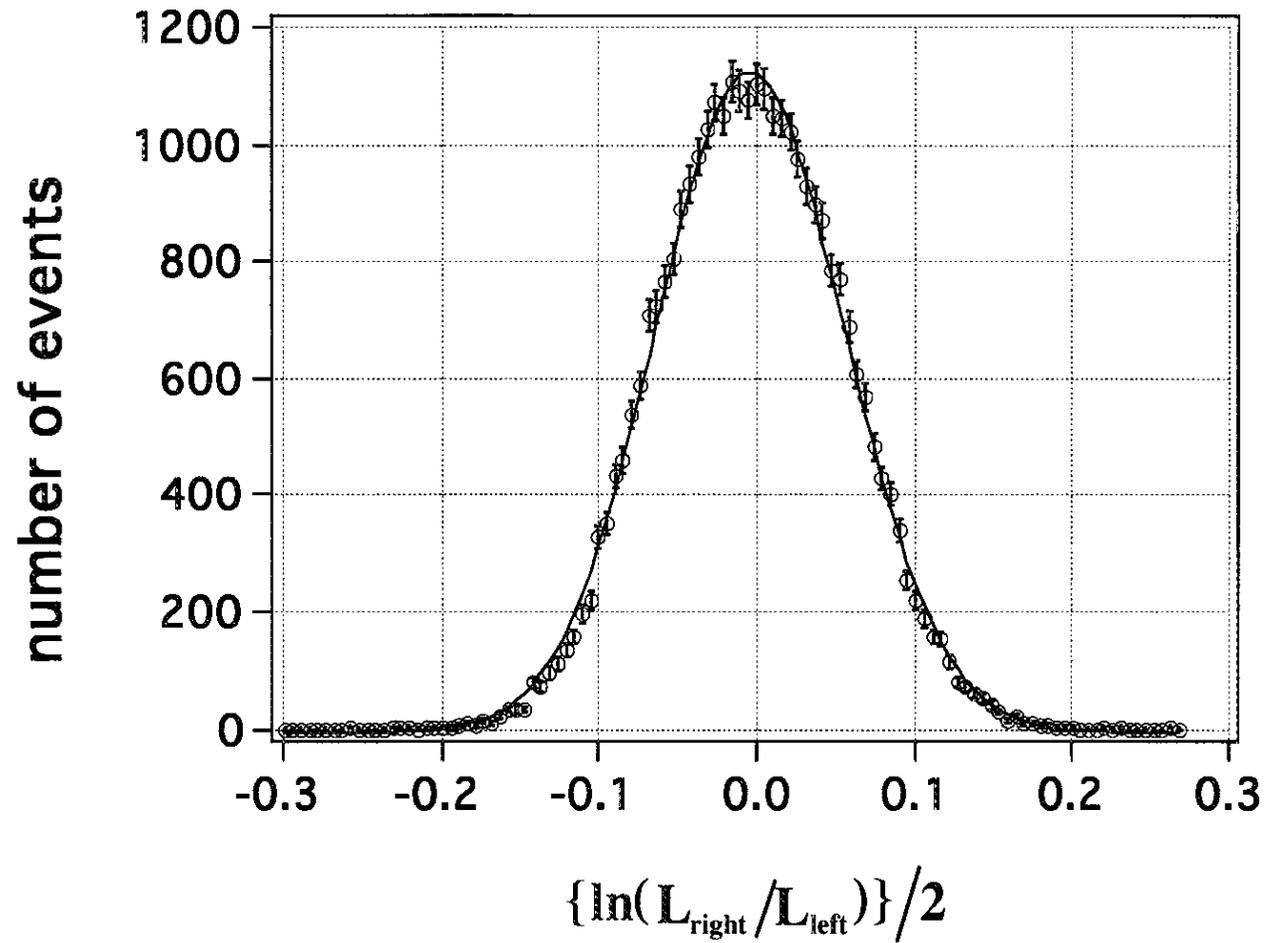[1] Horst Schölermann and Horst Klein, Nucl. Instr. Meth.169, 25 (1980)

Fig. B-1 The distribution function of $\{\ln(L_{right}/L_{left})\}/2$ (=$\alpha'x$). The white circle shows the experimental data, and the solid line shows the gaussian fitted curve.

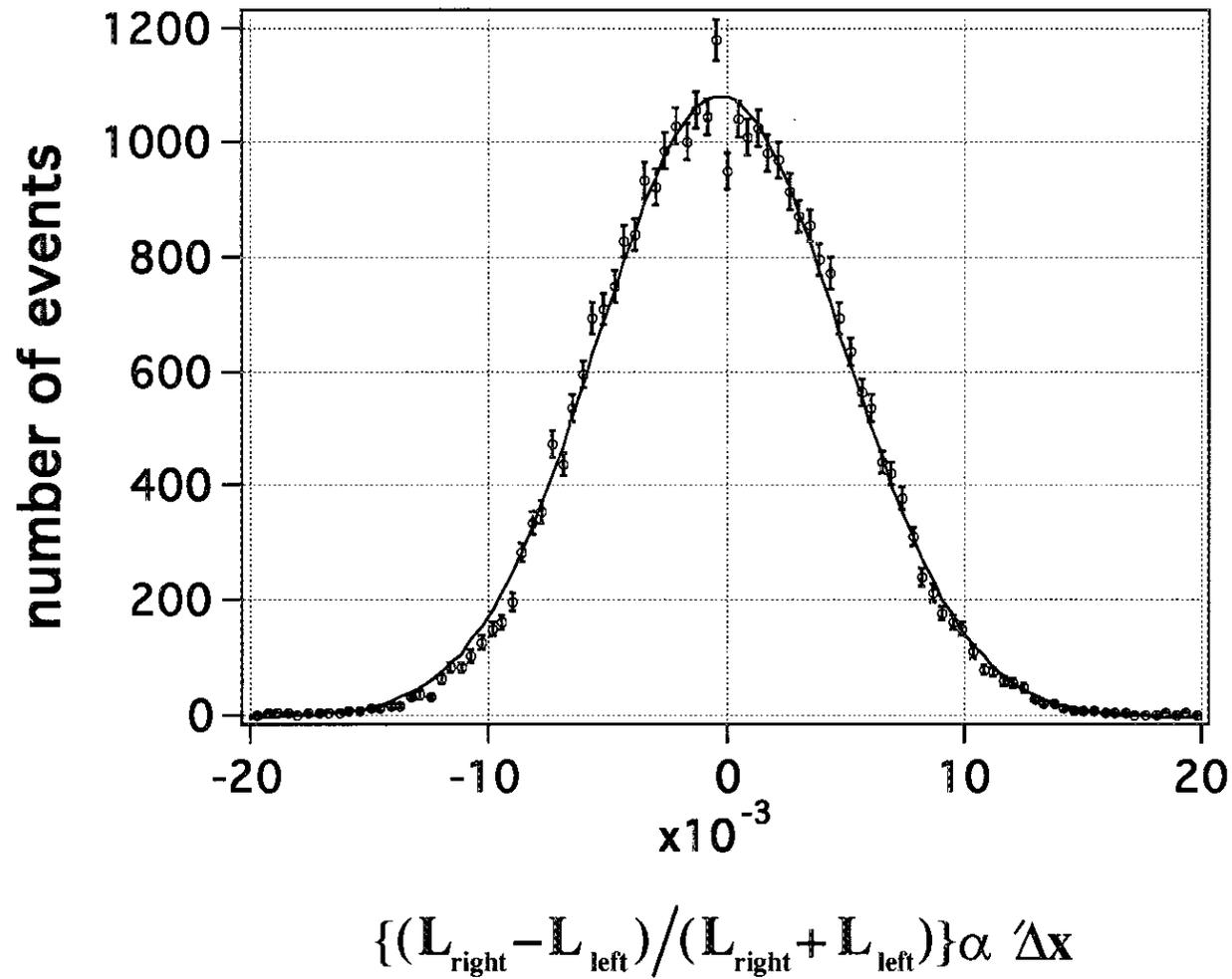$$\{(L_{right}-L_{left})/(L_{right}+L_{left})\}\alpha\ '\!\Delta x$$

Fig. B-2 The distribution function of $\Delta L/L(=\{(L_{right}-L_{left})/(L_{right}+L_{left})\}\alpha'\!\Delta x)$. The white circle shows the experimental data, and the solid line shows the gaussian fitted curve.

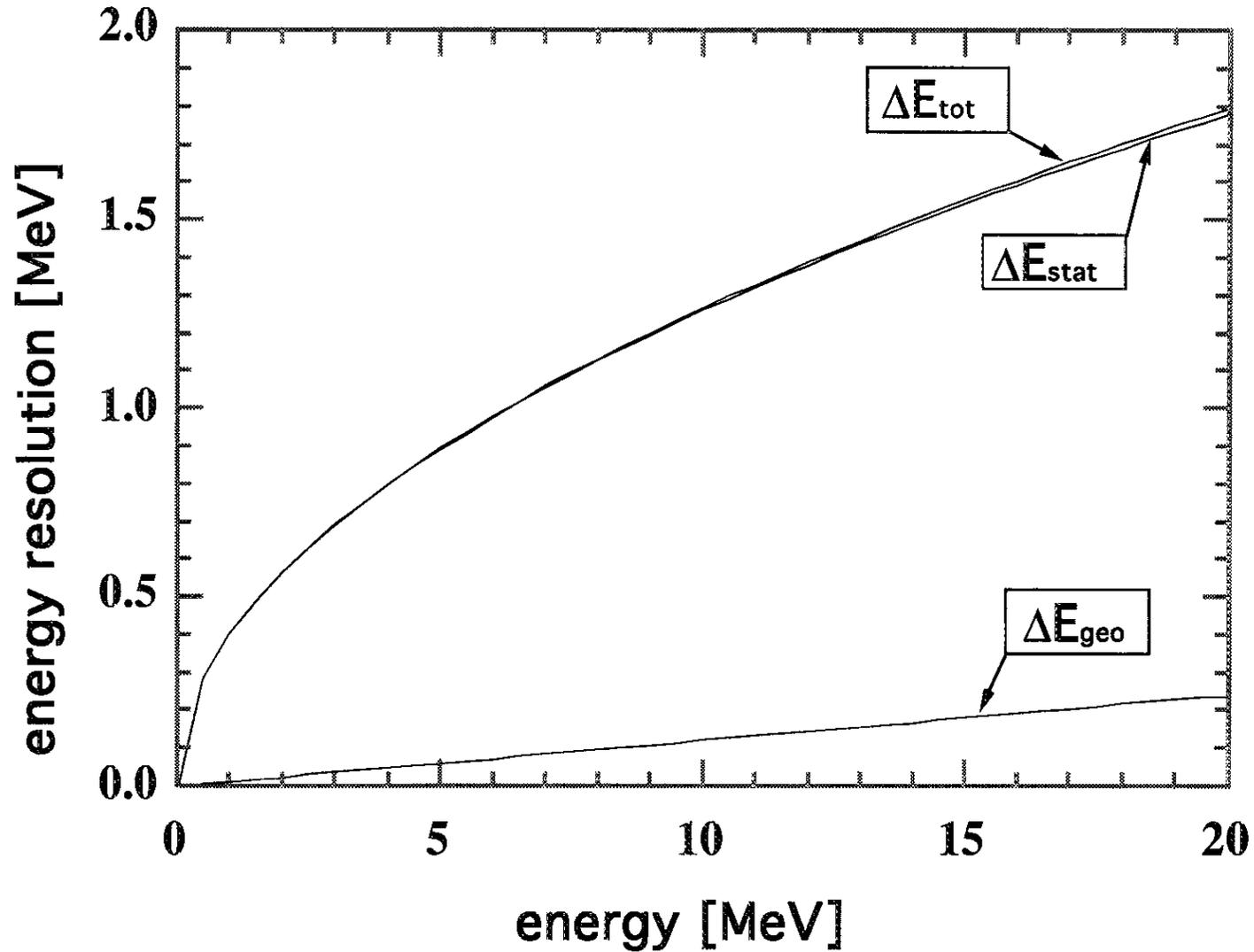Fig. B-3 The calculated energy resolution of ΔE-detector due to the geometrical influence (ΔE_{geo}) and the statistical fluctuation (ΔE_{stat}). The total energy resolution of ΔE-detector is estimated from $\Delta E_{tot}^2 = (\Delta E_{geo}^2 + \Delta E_{stat}^2)^{1/2}$.

Appendix C

Velocity and angular production probability of fusion products in laboratory system

a) Velocity and energy of fusion products in laboratory system

In this section, the velocity and energy of a fusion product in laboratory-system are derived when two kinds of particles "1" and "2" are undergoing a fusion reaction and produce new kinds of particles "3" and "4". Using their masses (m_i; i=1,2,3, and 4) and velocities in the laboratory frame, the center-of-mass velocity V and relative velocities u (before the reaction) and u' (after the reaction) can be expressed as:

$$V = \frac{m_1 v_1 + m_2 v_2}{m_1 + m_2} = \frac{m_3 v_3 + m_4 v_4}{m_3 + m_4},$$

$$u = v_1 - v_2, \text{ and } u' = v_3 - v_4.$$

The velocity of these particles in center-of-mass system are expressed as (Fig.C-1):

$$u_1 = v_1 - V = \frac{m_2}{m_1 + m_2} u,$$

$$u_2 = v_2 - V = -\frac{m_1}{m_1 + m_2} u,$$

$$u_3 = v_3 - V = \frac{m_4}{m_3 + m_4} u',$$

and

$$u_4 = v_4 - V = -\frac{m_3}{m_3 + m_4} u'.$$

From the conservation of energy, we get following relation;

$$\kappa + Q = \kappa'$$

where $\kappa = \frac{1}{2} m u^2$, $\kappa' = \frac{1}{2} m' u'^2$, and Q: Q value of nuclear reaction. The m and m' are reduced masses before and after the reaction, respectively, i.e.;
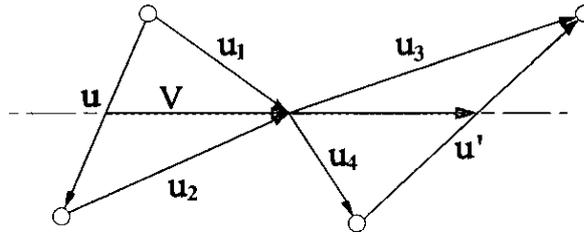
Fig.C-1 Nuclear reaction between particles kind "1" and "2". As a result of the reaction, particles kind "3" and "4" are emitted.
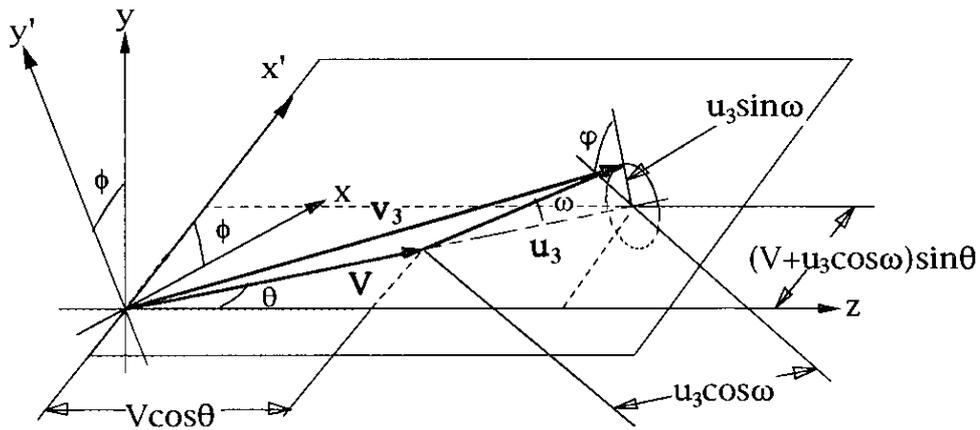

Fig.C-2 Relation of x-and y-axis with respect to the direction of center-of mass under the existence of magnetic field
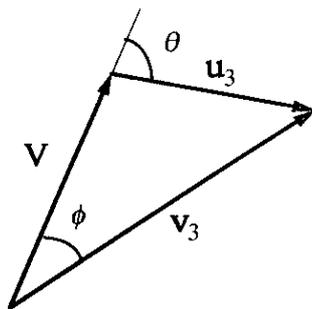

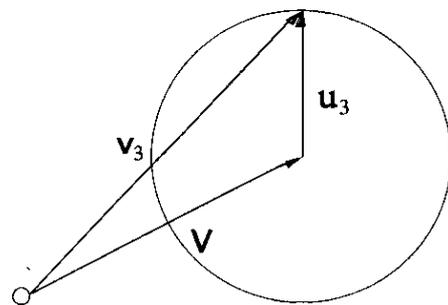Fig.C-3. Relation between vector u_3, v_3 and V.

Fig. C-4 Relation of V and u_3 when $\gamma < 1$

$$m = \frac{m_1 m_2}{m_1 + m_2} \quad \text{and} \quad m' = \frac{m_3 m_4}{m_3 + m_4}.$$

From the energy conservation, the u' is expressed as;

$$u' = \sqrt{\frac{2(\kappa + Q)}{m'}}.$$

Then, u_3 is:

$$u_3 = \sqrt{\frac{2m_4(\kappa + Q)}{m_3(m_3 + m_4)}}.$$

When z-axis of Cartesian coordinate is set to parallel to the magnetic field and both x- and y-axes are chosen arbitrarily as shown in Fig.C-2, it is difficult to express v_3. To simplify the problem, x'- is chosen so that the velocity V is included in x'z-plane, and y' are set to perpendicular to x'- and z-axes (Fig.C-2). In this coordinate, the velocities u_3 and V are expressed as follows;

$$u_3 = \begin{pmatrix} u_3(\cos\omega\sin\theta + \sin\omega\cos\varphi\cos\theta) \\ u_3\sin\omega\sin\varphi \\ u_3(\cos\omega\cos\theta - \sin\omega\cos\varphi\sin\theta) \end{pmatrix}, \text{ and } V = \begin{pmatrix} V\sin\theta \\ 0 \\ V\cos\theta \end{pmatrix}.$$

Then, velocity v_3 is,

$$v_3 = \begin{pmatrix} V\sin\theta + u_3(\cos\omega\sin\theta + \sin\omega\cos\varphi\cos\theta) \\ u_3\sin\omega\sin\varphi \\ V\cos\theta + u_3(\cos\omega\cos\theta - \sin\omega\cos\varphi\sin\theta) \end{pmatrix}.$$

Therefore, in xyz-coordinate, v_3 is

$$v_3 = \begin{pmatrix} V\sin\theta\cos\phi + u_3(\cos\omega\sin\theta\cos\phi + \sin\omega\cos\varphi\cos\theta\cos\phi - \sin\omega\sin\varphi\sin\phi) \\ V\sin\theta\sin\phi + u_3(\cos\omega\sin\theta\sin\phi + \sin\omega\cos\varphi\cos\theta\sin\phi + \sin\omega\sin\varphi\cos\phi) \\ V\cos\theta + u_3(\cos\omega\cos\theta - \sin\omega\cos\varphi\sin\theta) \end{pmatrix}.$$

(c-1)

The energy of particle kind "3" is:

$$\frac{1}{2}m_3 v_3 = \frac{1}{2}m_3 u_3^2 + \frac{1}{2}m_3 V^2 + m_3 u_3 V \cos\omega \qquad (c\text{-}2)$$

b) *Angular production probability of fusion products in laboratory system*

In center-of-mass system, the angular production probability of Fusion products of D-T reaction and D-^{3}He reaction can be considered as isotropic. The angular production probability of these reaction in laboratory system is discussed here.

The relation among the velocity of a fusion product particle(particle kind "3"), the velocity of the center-of-mass system and the production angle is shown in Fig.C-3. In the figure, u_3 is the velocity of the particle in center-of-mass system, v_3 is that in laboratory. system, and V is the center-of-mass velocity. The θ and ϕ are the production angle in center-of-mass system and in laboratory system, respectively. Since the production of the particle kind "3" is considered as isotropic in center-of-mass system, the probability with which the particle enters into a small solid angle $d\Omega$ along Ω, will be ; $P(\Omega)d\Omega = \frac{1}{4\pi}d\Omega = \frac{1}{4\pi}d\xi d\varphi$, where φ is an azimuthal angle around V and ξ is cosine of ϕ. By integrating the probability over φ, the production probability in ξ is obtained as;

$$P(\xi) = \begin{cases} 1/2 --- (-1 \le \xi \le 1) \\ 0 --- (other) \end{cases}.$$

In the Lab system, this probability becomes;

$$P(\mu) = P(\xi)\frac{d\xi}{d\mu}.$$

Using the velocity of the particle kind "3" and the center-of-mass velocity, the velocity of the particle in laboratory system can be expressed as;

$$v_3 = u_3 + V.$$

Then, we get;

$$v_3 = V\sqrt{1 + 2\gamma\xi + \gamma^2} \quad \text{and} \quad v_3\mu = V(1 + \gamma\xi),$$

where $\gamma = u_3/V$. Therefore, μ and ξ are

$$\mu = \frac{1 + \gamma\xi}{\sqrt{1 + 2\gamma\xi + \gamma^2}}.\text{and} \qquad \text{(C-3)}$$

$$\xi = \left[-(1 - \mu^2) \pm \mu\sqrt{\mu^2 + \gamma^2 - 1}\right]/\gamma \qquad \text{(C-4)}$$

$$\frac{d\mu}{d\xi} = \frac{\gamma^2(\gamma + \xi)}{(1 + 2\gamma\xi + \gamma^2)^{3/2}} \qquad \text{(C-5)}$$

The sign in eq.(C-4) is determined in the following manner.

i) $\gamma < 1$ (in the case of $v_3 < V$)

In this case, $\mu = 1$ for both $\xi = \pm 1$ and there is a minimum μ for certain ξ. The minimum μ is obtained when $V^2 = v_3^2 + u_3^2$ and;

$$\mu = \sqrt{1 - \gamma^2} \quad \text{when} \quad \xi = -\gamma.$$

When $\sqrt{1 - \gamma^2} \leq \mu \leq 1$, μ could have both signs of eq.(c) and in other case there exists no real ξ. Therefore, we obtain

$$P(\mu) = \begin{cases} \left.\frac{1}{2}\frac{d\xi}{d\mu}\right|_+ , or \left.\frac{1}{2}\frac{d\xi}{d\mu}\right|_- \quad ---\left(\sqrt{1 - \gamma^2} \leq \mu \leq 1\right) \\ 0 --- (other) \end{cases}$$

where the sign of $\frac{d\xi}{d\mu}$ correspond that in eq.(d).

ii) $\gamma > 1$ (in the case of $v_3 > V$)

In this case, we have $\mu = 1$ when $\xi = 1$ and $\mu = -1$ when $\xi = -1$. Therefore, the sign in eq.(d) should be plus(+). $P(\mu)$ becomes;

$$P(\mu) = \begin{cases} \frac{1}{2}\frac{d\xi}{d\mu} ---- (-1 \leq \mu \leq 1) \\ 0 --- (other) \end{cases}$$

89